

1

2 A SEARCH FOR LONG-LIVED, CHARGED, SUPERSYMMETRIC PARTICLES
3 USING IONIZATION WITH THE ATLAS DETECTOR

4

BRADLEY AXEN

5

6 September 2016 – Version 0.37

⁸ Bradley Axen: *A Search for Long-Lived, Charged, Supersymmetric Particles using*
⁹ *Ionization with the ATLAS Detector*, Subtitle, © September 2016

10

Usually a quotation.

11

Dedicated to.

₁₂ ABSTRACT

₁₃ How to write a good abstract:

₁₄ <https://plg.uwaterloo.ca/~migod/research/beck00PSLA.html>

₁₅ PUBLICATIONS

₁₆ Some ideas and figures have appeared previously in the following publications:

₁₇

₁₈ Put your publications from the thesis here. The packages `multibib` or `bibtopic`
₁₉ etc. can be used to handle multiple different bibliographies in your document.

²¹ ACKNOWLEDGEMENTS

²² Put your acknowledgements here.

²³

²⁴ And potentially a second round.

²⁵

26 CONTENTS

27	I	INTRODUCTION	1
28	1	INTRODUCTION	3
29	II	THEORETICAL CONTEXT	5
30	2	STANDARD MODEL	7
31	2.1	Particles	7
32	2.2	Interactions	8
33	2.3	Limitations	8
34	3	SUPERSYMMETRY	9
35	3.1	Motivation	9
36	3.2	Structure	9
37	3.3	Phenomenology	9
38	4	LONG-LIVED PARTICLES	11
39	4.1	Mechanisms	11
40	4.1.1	Examples in Supersymmetry	11
41	4.2	Phenomenology	11
42	4.2.1	Disimilarities to Prompt Decays	11
43	4.2.2	Characteristic Signatures	11
44	III	EXPERIMENTAL STRUCTURE AND RECONSTRUCTION	13
45	5	THE LARGE HADRON COLLIDER	15
46	5.1	Injection Chain	15
47	5.2	Design and Parameters	15
48	5.3	Luminosity	15
49	6	THE ATLAS DETECTOR	17
50	6.1	Coordinate System	17
51	6.2	Magnetic Field	17
52	6.3	Inner Detector	17
53	6.3.1	Pixel Detector	17
54	6.3.2	Semiconductor Tracker	17
55	6.3.3	Transition Radiation Tracker	17
56	6.4	Calorimetry	17
57	6.4.1	Electromagnetic Calorimeters	17
58	6.4.2	Hadronic Calorimeters	17
59	6.4.3	Forward Calorimeters	17
60	6.5	Muon Spectrometer	17
61	6.6	Trigger	17
62	6.6.1	Trigger Scheme	17
63	6.6.2	Missing Transverse Energy Triggers	17
64	7	EVENT RECONSTRUCTION	19
65	7.1	Tracks and Vertices	19

66	7.1.1	Track Reconstruction	19
67	7.1.2	Vertex Reconstruction	19
68	7.2	Jets	19
69	7.2.1	Topological Clustering	19
70	7.2.2	Jet Energy Scale	19
71	7.2.3	Jet Energy Scale Uncertainties	19
72	7.2.4	Jet Energy Resolution	19
73	7.3	Electrons	19
74	7.3.1	Electron Identification	19
75	7.4	Muons	19
76	7.4.1	Muon Identification	19
77	7.5	Missing Transverse Energy	19
78	IV	CALORIMETER RESPONSE	21
79	8	RESPONSE MEASUREMENT WITH SINGLE HADRONS	23
80	8.1	Dataset and Simulation	24
81	8.1.1	Data Samples	24
82	8.1.2	Simulated Samples	24
83	8.1.3	Event Selection	24
84	8.2	Inclusive Hadron Response	25
85	8.2.1	E/p Distribution	25
86	8.2.2	Zero Fraction	26
87	8.2.3	Neutral Background Subtraction	27
88	8.2.4	Corrected Response	29
89	8.2.5	Additional Studies	31
90	8.3	Identified Particle Response	34
91	8.3.1	Decay Reconstruction	34
92	8.3.2	Identified Response	35
93	8.3.3	Additional Species in Simulation	37
94	8.4	Summary	38
95	9	JET ENERGY RESPONSE AND UNCERTAINTY	41
96	9.1	Motivation	41
97	9.2	Uncertainty Estimate	41
98	9.3	Summary	44
99	V	SEARCH FOR LONG-LIVED PARTICLES	47
100	10	LONG-LIVED PARTICLES IN ATLAS	49
101	10.1	Event Topology	49
102	10.1.1	Detector Interactions	50
103	10.1.2	Lifetime Dependence	51
104	10.2	Simulation	54
105	11	EVENT SELECTION	57
106	11.1	Trigger	58
107	11.2	Kinematics and Isolation	59
108	11.3	Particle Species Rejection	63
109	11.4	Ionization	66
110	11.4.1	Mass Estimation	67

111	11.5 Efficiency	68
112	12 BACKGROUND ESTIMATION	71
113	12.1 Background Sources	71
114	12.2 Prediction Method	72
115	12.3 Validation	73
116	12.3.1 Closure in Simulation	73
117	12.3.2 Validation Region in Data	74
118	13 SYSTEMATIC UNCERTAINTIES AND RESULTS	77
119	13.1 Systematic Uncertainties	77
120	13.1.1 Background Estimate	77
121	13.1.2 Signal Yield	78
122	13.2 Final Yields	84
123	13.3 Cross Sectional Limits	85
124	13.4 Mass Limits	89
125	13.5 Context for Long-Lived Searches	89
126	VI CONCLUSIONS	93
127	14 SUMMARY AND OUTLOOK	95
128	14.1 Summary	95
129	14.2 Outlook	95
130	VII APPENDIX	97
131	A INELASTIC CROSS SECTION	99
132	B EXPANDED R-HADRON YIELDS AND LIMITS	101
133	BIBLIOGRAPHY	107

134 LIST OF FIGURES

135	Figure 1	The particle content of the Standard Model (SM).	8
136	Figure 2	An illustration (a) of the E/p variable used throughout this paper. The red energy deposits come from the charged particle targeted for measurement, while the blue energy deposits are from nearby neutral particles and must be subtracted. The same diagram (b) for the neutral-background selection, described in Section 8.2.3.	26
137			
138			
139			
140			
141			
142	Figure 3	The E/p distribution and ratio of simulation to data for isolated tracks with (a) $ \eta < 0.6$ and $1.2 < p/\text{GeV} < 1.8$ and (b) $ \eta < 0.6$ and $2.2 < p/\text{GeV} < 2.8$	26
143			
144			
145	Figure 4	The fraction of tracks as a function (a, b) of momentum, (c, d) of interaction lengths with $E \leq 0$ for tracks with positive (on the left) and negative (on the right) charge.	28
146			
147			
148			
149	Figure 5	$\langle E/p \rangle_{\text{BG}}$ as a function of the track momentum for tracks with (a) $ \eta < 0.6$, (b) $0.6 < \eta < 1.1$, and as a function of the track pseudorapidity for tracks with (c) $1.2 < p/\text{GeV} < 1.8$, (d) $1.8 < p/\text{GeV} < 2.2$	29
150			
151			
152			
153	Figure 6	$\langle E/p \rangle_{\text{COR}}$ as a function of track momentum, for tracks with (a) $ \eta < 0.6$, (b) $0.6 < \eta < 1.1$, (c) $1.8 < \eta < 1.9$, and (d) $1.9 < \eta < 2.3$	30
154			
155			
156	Figure 7	$\langle E/p \rangle_{\text{COR}}$ calculated using LCW-calibrated topological clusters as a function of track momentum for tracks with (a) zero or more associated topological clusters or (b) one or more associated topological clusters.	31
157			
158			
159			
160	Figure 8	Comparison of the $\langle E/p \rangle_{\text{COR}}$ for tracks with (a) less than and (b) greater than 20 hits in the TRT.	32
161			
162	Figure 9	Comparison of the $\langle E/p \rangle_{\text{COR}}$ for (a) positive and (b) negative tracks as a function of track momentum for tracks with $ \eta < 0.6$	32
163			
164			
165	Figure 10	Comparison of the E/p distributions for (a) positive and (b) negative tracks with $0.8 < p/\text{GeV} < 1.2$ and $ \eta < 0.6$, in simulation with the FTFP_BERT and QGSP_BERT physics lists.	33
166			
167			
168			
169	Figure 11	Comparison of the response of the hadronic calorimeter as a function of track momentum (a) at the EM-scale and (b) after the LCW calibration.	33
170			
171			
172	Figure 12	Comparison of the response of the EM calorimeter as a function of track momentum (a) at the EM-scale and (b) with the LCW calibration.	34
173			
174			

175	Figure 13	The reconstructed mass peaks of (a) K_S^0 , (b) Λ , and (c) $\bar{\Lambda}$ candidates.	35
176			
177	Figure 14	The E/p distribution for isolated (a) π^+ , (b) π^- , (c) proton, and (d) anti-proton tracks.	36
178			
179	Figure 15	The fraction of tracks with $E \leq 0$ for identified (a) π^+ and π^- , and (b) proton and anti-proton tracks	36
180			
181	Figure 16	The difference in $\langle E/p \rangle$ between (a) π^+ and π^- (b) p and π^+ , and (c) \bar{p} and π^-	37
182			
183	Figure 17	$\langle E/p \rangle_{\text{COR}}$ as a function of track momentum for (a) π^+ tracks and (b) π^- tracks.	38
184			
185	Figure 18	The ratio of the calorimeter response to single parti- cles of various species to the calorimeter response to π^+ with the physics list FTFP_BERT.	38
186			
187	Figure 19	The spectra of true particles inside anti- k_t , $R = 0.4$ jets with (a) $90 < p_T/\text{GeV} < 100$, (b) $400 < p_T/\text{GeV} <$ 500 , and (c) $1800 < p_T/\text{GeV} < 2300$	42
188			
190	Figure 20	The jet energy scale (<a>JES) uncertainty contributions, as well as the total <a>JES uncertainty, as a function of jet p_T for (a) $ \eta < 0.6$ and (b) $0.6 < \eta < 1.1$	44
191			
193	Figure 21	The <a>JES correlations as a function of jet p_T and $ \eta $ for jets in the central region of the detector.	45
194			
195	Figure 22	A schematic diagram of an R-Hadron event with a life- time around 0.01 ns. The diagram includes one charged R-Hadron (solid blue), one neutral R-Hadron (dashed blue), Lightest Supersymmetric Particles (<a>LSPs) (dashed green) and charged hadrons (solid orange). The pixel detector, calorimeters, and muon system are illustrated but not to scale.	51
196			
197	Figure 23	A schematic diagram of an R-Hadron event with a life- time around 4 ns. The diagram includes one charged R-Hadron (solid blue), one neutral R-Hadron (dashed blue), <a>LSPs (dashed green) and a charged hadron (solid orange). The pixel detector, calorimeters, and muon system are illustrated but not to scale.	52
198			
199	Figure 24	A schematic diagram of an R-Hadron event with a life- time around 5 ns. The diagram includes one charged R-Hadron (solid blue), one neutral R-Hadron (dashed blue), <a>LSPs (dashed green) and charged hadrons (solid orange). The pixel detector, calorimeters, and muon system are illustrated but not to scale.	53
200			
201	Figure 25	A schematic diagram of an R-Hadron event with a life- time around 20 ns. The diagram includes one charged R-Hadron (solid blue), one neutral R-Hadron (dashed blue), <a>LSPs (dashed green) and charged hadrons (solid orange). The pixel detector, calorimeters, and muon system are illustrated but not to scale.	53
202			

221	Figure 26	A schematic diagram of an R-Hadron event with a life-time around 20 ns. The diagram includes one charged R-Hadron (solid blue) and one neutral R-Hadron (dashed blue). The pixel detector, calorimeters, and muon system are illustrated but not to scale.	54
222			
223			
224			
225			
226	Figure 27	The distribution of (a) E_T^{miss} and (b) Calorimeter E_T^{miss} for simulated signal events before the trigger requirement.	58
227			
228			
229	Figure 28	The distribution of E_T^{miss} for data and simulated signal events, after the trigger requirement.	60
230			
231	Figure 29	The trigger efficiency for the HLT_xe70 trigger requirement as a function of (a) E_T^{miss} and (b) Calorimeter E_T^{miss} for simulated signal events.	61
232			
233			
234	Figure 30	The dependence of dE/dx on N_{split} in data after basic track hit requirements have been applied.	62
235			
236	Figure 31	The distribution of dE/dx with various selections applied in data and simulated signal events.	62
237			
238	Figure 32	The distribution of track momentum for data and simulated signal events, after previous selection requirements have been applied.	63
239			
240			
241	Figure 33	The distribution of M_T for data and simulated signal events, after previous selection requirements have been applied.	64
242			
243			
244	Figure 34	The distribution of summed tracked momentum within a cone of $\Delta R < 0.25$ around the candidate track for data and simulated signal events, after previous selection requirements have been applied.	65
245			
246			
247			
248	Figure 35	The normalized, two-dimensional distribution of E/p and f_{EM} for simulated (a) $Z \rightarrow ee$, (b) $Z \rightarrow \tau\tau$, (c) 1200 GeV Stable R-Hadron events, and (d) 1200 GeV, 10 ns R-Hadron events.	66
249			
250			
251			
252	Figure 36	Two-dimensional distribution of dE/dx versus charge signed momentum (qp) for minimum-bias tracks. The fitted distributions of the most probable values for pions, kaons and protons are superimposed.	67
253			
254			
255			
256	Figure 37	The distribution of mass estimated using dE/dx for simulated stable R-Hadrons with masses between 1000 and 1600 GeV.	68
257			
258			
259	Figure 38	The acceptance \times efficiency as a function of R-Hadron (a) mass and (b) lifetime. (a) shows all of the combinations of mass and lifetime considered in this search, and (b) highlights the lifetime dependence for 1000 GeV and 1600 GeV R-Hadrons.	70
260			
261			
262			
263			

264	Figure 39	The distribution of (a) dE/dx and (b) momentum for tracks in data and simulated signal after requiring the event level selection and the track selection on p_T , hits, and N_{split} . Each sub-figure shows the normalized distributions for tracks classified as hadrons, electrons, and muons in data and R-Hadrons in the simulated signal.	72
265			
266			
267			
268			
269			
270			
271	Figure 40	The distribution of $M_{dE/dx}$ (a) before and (b) after the ionization requirement for tracks in simulated W boson decays and for the randomly generated background estimate.	74
272			
273			
274			
275	Figure 41	The distribution of $M_{dE/dx}$ (a) before and (b) after the ionization requirement for tracks in the validation region and for the randomly generated background estimate.	75
276			
277			
278			
279	Figure 42	The trigger efficiency for the HLT_xe70 trigger requirement as a function of Calorimeter E_T^{miss} for simulated data events with a W boson selection. Simulated signal events and simulated W boson events are also included.	80
280			
281			
282			
283			
284	Figure 43	The efficiency of the muon veto for R-hadrons of two different masses, as a function of $\frac{1}{\beta}$ for simulated R-Hadron tracks.	82
285			
286			
287	Figure 44	The average reconstructed MDT β distribution for $Z \rightarrow \mu\mu$ events in which one of the muons is reconstructed as a slow muon, for both data and simulation. A gaussian fit is superimposed.	83
288			
289			
290			
291	Figure 45	The observed mass distribution of events in data and the generated background distribution in (a) the stable and (b) the metastable signal region. A few example simulated signal distributions are superimposed.	84
292			
293			
294			
295	Figure 46	The observed and expected cross section limits as a function of mass for the stable simulated signal. The predicted cross section values for the corresponding signals are included.	87
296			
297			
298			
299	Figure 47	The observed and expected cross section limits as a function of mass for each generated lifetime. The predicted cross section values for the corresponding signals are included.	88
300			
301			
302			
303	Figure 48	The excluded range of masses as a function of gluino lifetime. The expected lower limit (LL), with its experimental $\pm 1\sigma$ band, is given with respect to the nominal theoretical cross-section. The observed 95% LL obtained at $\sqrt{s} = 8$ TeV [55] is also shown for comparison.	90
304			
305			
306			
307			

308	Figure 49	The constraints on the gluino mass as a function of lifetime for a split-supersymmetry model with the gluino R-Hadrons decaying into a gluon or light quarks and a neutralino with mass of 100 GeV. The solid lines indicate the observed limits, while the dashed lines indicate the expected limits. The area below the curves is excluded. The dots represent results for which the particle is assumed to be prompt or stable.	91
309			
310			
311			
312			
313			
314			
315			

316 LIST OF TABLES

317	Table 1	The dominant sources of corrections and systematic uncertainties in the JES estimation technique, includ- ing typical values for the correcting shift (Δ) and the associated uncertainty (σ).	43
320			
321	Table 2	The expected number of events at each level of the se- lection for metastable 1600 GeV, 10 ns R-Hadrons, along with the number of events observed in data, for 3.2 fb^{-1} . The simulated yields are shown with statis- tical uncertainties only. The total efficiency \times accep- tance is also shown for the signal.	69
322			
323			
324			
325			
326			
327	Table 3	A summary of the sources of systematic uncertainty for the data-driven background in the signal region. If the uncertainty depends on the mass, the maximum values are reported.	77
328			
329			
330			
331	Table 4	A summary of the sources of systematic uncertainty for the simulated signal yield. The uncertainty depends on the mass and lifetime, and the maximum negative and positive values are reported in the table.	79
332			
333			
334			
335	Table 5	Example of the contributing systematic variations to the total systematic for the E_T^{miss} Scale, as measured in a 1200 GeV, Stable R-Hadron signal sample.	81
336			
337			
338	Table 6	The estimated number of background events and the number of observed events in data for the specified se- lection regions prior to the requirement on mass. The background estimates show statistical and systematic uncertainties.	84
339			
340			
341			
342			
343	Table 7	The left and right extremum of the mass window for each generated mass point with a 10 ns lifetime.	85
344			
345	Table 8	The left and right extremum of the mass window used for each generated stable mass point.	85
346			
347	Table 9	The expected number of signal events, the expected number of background events, and the observed num- ber of events in data with their respective statistical er- rors within the respective mass window for each gen- erated stable mass point.	86
348			
349			
350			
351			
352	Table 10	The expected number of signal events, the expected number of background events, and the observed num- ber of events in data with their respective statistical er- rors within the respective mass window for each gen- erated mass point with a lifetime of 10 ns.	86
353			
354			
355			
356			

357	Table 11	The observed and expected 95% CL lower limit on mass for gluino R-Hadrons for each considered lifetime.	89
358			
359	Table 12	The left and right extremum of the mass window for each generated mass point with a 50 ns lifetime.	101
360			
361	Table 13	The left and right extremum of the mass window for each generated mass point with a 30 ns lifetime.	101
362			
363	Table 14	The left and right extremum of the mass window for each generated mass point with a 10 ns lifetime.	102
364			
365	Table 15	The left and right extremum of the mass window used for each generated mass point with a lifetime of 3 ns.	102
366			
367	Table 16	The left and right extremum of the mass window used for each mass point with a lifetime of 1 ns.	102
368			
369	Table 17	The left and right extremum of the mass window for each generated mass point with a lifetime of 0.4 ns.	103
370			
371	Table 18	The left and right extremum of the mass window used for each generated stable mass point.	103
372			
373	Table 19	The expected number of signal events, the expected number of background events, and the observed number of events in data with their respective statistical errors within the respective mass window for each generated mass point with a lifetime of 50 ns.	103
374			
375			
376			
377			
378	Table 20	The expected number of signal events, the expected number of background events, and the observed number of events in data with their respective statistical errors within the respective mass window for each generated mass point with a lifetime of 30 ns.	104
379			
380			
381			
382			
383	Table 21	The expected number of signal events, the expected number of background events, and the observed number of events in data with their respective statistical errors within the respective mass window for each generated mass point with a lifetime of 10 ns.	104
384			
385			
386			
387			
388	Table 22	The expected number of signal events, the expected number of background events, and the observed number of events in data with their respective statistical errors within the respective mass window for each generated mass point with a lifetime of 3 ns.	105
389			
390			
391			
392			
393	Table 23	The expected number of signal events, the expected number of background events, and the observed number of events in data with their respective statistical errors within the respective mass window for each generated mass point with a lifetime of 1 ns.	105
394			
395			
396			
397			
398	Table 24	The expected number of signal events, the expected number of background events, and the observed number of events in data with their respective statistical errors within the respective mass window for each generated mass point with a lifetime of p4 ns.	106
399			
400			
401			
402			

403	Table 25	The expected number of signal events, the expected number of background events, and the observed num- ber of events in data with their respective statistical er- rors within the respective mass window for each gen- erated stable mass point	106
404			
405			
406			
407			

409 ACRONYMS

- 410 SM Standard Model
411 SUSY Supersymmetry
412 LSP Lightest Supersymmetric Particle
413 LHC Large Hadron Collider
414 ATLAS A Toroidal LHC ApparatuS
415 ToT time over threshold
416 LCW local cluster weighted
417 MIP minimally ionizing particle
418 EPJC European Physical Journal C
419 JES jet energy scale
420 LLP Long-Lived Particle
421 CR Control Region
422 NLO next-to-leading order
423 NLL next-to-leading logarithmic
424 PDF parton distribution function
425 ISR initial state radiation
426 RMS root mean square
427 IBL Insertible B-Layer
428 CP Combined Performance
429 MDT Monitored Drift Tube

430

PART I

431

INTRODUCTION

432

You can put some informational part preamble text here.

1

433

434 INTRODUCTION

435

PART II

436

THEORETICAL CONTEXT

437

You can put some informational part preamble text here.

2

438

439 STANDARD MODEL

440 The SM of particle physics seeks to explain the symmetries and interactions of
441 all currently discovered fundamental particles. It has been tested by several genera-
442 tions of experiments and has been remarkably successful, no significant de-
443 viations have been found. The SM provides predictions in particle physics for
444 interactions up to the Planck scale (10^{15} - 10^{19} GeV).

445 The theory itself is a quantum field theory grown from an underlying $SU(3) \times$
446 $SU(2) \times U(1)$ that requires the particle content and quantum numbers consist-
447 ent with experimental observations (see Section 2.1). Each postulated symme-
448 try is accompanied by an interaction between particles through gauge invari-
449 ance. These interactions are referred to as the Strong, Weak, and Electromag-
450 netic forces, which are discussed in Section 2.2.

451 Although this model has been very predictive, the theory is incomplete; for
452 example, it is not able to describe gravity or astronomically observed dark matter.
453 These limitations are discussed in more detail in Section 2.3.

454 21 PARTICLES

455 The most familiar matter in the universe is made up of protons, neutrons, and
456 electrons. Protons and neutrons are composite particles, however, and are made
457 up in turn by particles called quarks. Quarks carry both electric charge and color
458 charge, and are bound in color-neutral combinations called baryons. The elec-
459 tron is an example of a lepton, and carries only electric charge. Another type
460 of particle, the neutrino, does not form atomic structures in the same way that
461 quarks and leptons do because it carries no color or electric charge. Collectively,
462 these types of particles are known as fermions, the group of particles with half-
463 integer spin.

464 There are three generations of fermions, although familiar matter is formed
465 predominantly by the first generation. The generations are identical except for
466 their masses, which increase in each generation by convention. In addition, each
467 of these particles is accompanied by an antiparticle, with opposite-sign quantum
468 numbers but the same mass.

469 The fermions comprise what is typically considered matter, but there are
470 additional particles that are mediators of interactions between those fermions.
471 These mediators are known as the gauge bosons, gauge in that their existence
472 is required by gauge invariance (discussed further in Section 2.2) and bosons in
473 that they have integer spin. The boson which mediates the electromagnetic force
474 is the photon, the first boson to be discovered; it has no electric charge, no mass,
475 and a spin of 1. There are three spin-1 mediators of the weak force, the two
476 W bosons and the Z boson. The W bosons have electric charge of ± 1 and a
477 mass of 80.385 ± 0.015 GeV, while the Z boson is neutral and has a mass of

478 91.1876 \pm 0.0021 GeV. The strong force is mediated by eight particles called
 479 gluons, which are massless and electrically neutral but do carry color charge.

480 The final particle present in the SM is the Higgs boson, which was recently
 481 observed for the first time by experiments at CERN in 2012. It is electrically
 482 neutral, has a mass of 125.7 \pm 0.4 GeV, and is the only spin-0 particle yet to be
 483 observed. The Higgs boson is the gauge boson associated with the mechanism
 484 that gives a mass to the W and Z bosons.

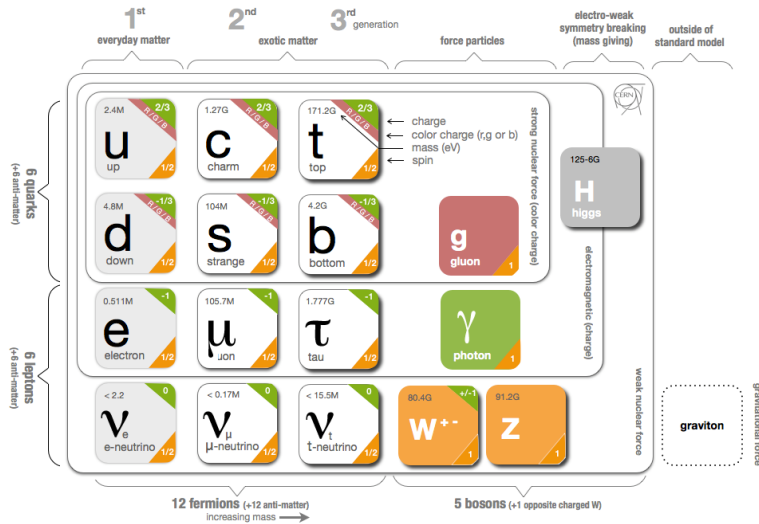


Figure 1: The particle content of the SM.

485 Together these particles form the entire content of the SM, and are summa-
 486 rized in Figure 1. These are the particles that constitute the observable universe
 487 and all the so-far-observed interactions within it.

488 2.2 INTERACTIONS

489 The interactions predicted and described by the SM are fundamentally tied to the
 490 particles within it, both in that they describe the way those particles can influence
 491 each other and also in that the existence of the interactions requires the existence
 492 of some particles (the gauge bosons).

493 2.3 LIMITATIONS

3

494

495 SUPERSYMMETRY

496 3.1 MOTIVATION

497 3.2 STRUCTURE

498 3.3 PHENOMENOLOGY

4

499

500 LONG-LIVED PARTICLES

501 4.1 MECHANISMS

502 4.1.1 EXAMPLES IN SUPERSYMMETRY

503 4.2 PHENOMENOLOGY

504 4.2.1 DISIMILARITIES TO PROMPT DECAYS

505 4.2.2 CHARACTERISTIC SIGNATURES

506

PART III

507

EXPERIMENTAL STRUCTURE AND RECONSTRUCTION

508

You can put some informational part preamble text here.

5

509

510 THE LARGE HADRON COLLIDER

511 5.1 INJECTION CHAIN

512 5.2 DESIGN AND PARAMETERS

513 5.3 LUMINOSITY

6

s14

s15 THE ATLAS DETECTOR

s16 6.1 COORDINATE SYSTEM

s17 6.2 MAGNETIC FIELD

s18 6.3 INNER DETECTOR

s19 6.3.1 PIXEL DETECTOR

s20 6.3.2 SEMICONDUCTOR TRACKER

s21 6.3.3 TRANSITION RADIATION TRACKER

s22 6.4 CALORIMETRY

s23 6.4.1 ELECTROMAGNETIC CALORIMETERS

s24 6.4.2 HADRONIC CALORIMETERS

s25 6.4.3 FORWARD CALORIMETERS

s26 6.5 MUON SPECTROMETER

s27 6.6 TRIGGER

s28 6.6.1 TRIGGER SCHEME

s29 6.6.2 MISSING TRANSVERSE ENERGY TRIGGERS

7

530

531 EVENT RECONSTRUCTION

532 The ATLAS experiment combines measurements in the subdetectors to form a
533 cohesive picture of each physics event.

534 7.1 TRACKS AND VERTICES

535 7.1.1 TRACK RECONSTRUCTION

536 7.1.1.1 NEURAL NETWORK

537 7.1.1.2 PIXEL DE/DX

538 7.1.2 VERTEX RECONSTRUCTION

539 7.2 JETS

540 7.2.1 TOPOLOGICAL CLUSTERING

541 7.2.2 JET ENERGY SCALE

542 7.2.3 JET ENERGY SCALE UNCERTAINTIES

543 7.2.4 JET ENERGY RESOLUTION

544 7.3 ELECTRONS

545 7.3.1 ELECTRON IDENTIFICATION

546 7.4 MUONS

547 7.4.1 MUON IDENTIFICATION

548 7.5 MISSING TRANSVERSE ENERGY

549

PART IV

550

CALORIMETER RESPONSE

551

You can put some informational part preamble text here.

8

552

553 RESPONSE MEASUREMENT WITH SINGLE HADRONS

554 As discussed in Section 7.2, colored particles produced in collisions hadronize
555 into jets of multiple hadrons. One approach to understanding jet energy mea-
556 surements in the ATLAS calorimeters is to evaluate the calorimeter response to
557 those individual hadrons; measurements of individual hadrons can be used to
558 build up an understanding of the jets that they form. The redundancy of the
559 momentum provided by the tracking system and the energy provided by the
560 calorimeter provides an opportunity to study calorimeter response using real
561 collisions, as described further in Section 8.2.

562 Calorimeter response includes a number of physical effects that can be ex-
563 tracted to provide insight into many aspects of jet modeling. First, many charged
564 hadrons interact with the material of the detector prior to reaching the calorime-
565 ters and thus do not deposit any energy. Comparing this effect in data and simu-
566 lation is a powerful tool in validating the interactions of particles with the mate-
567 rial of the detector and the model of the detector geometry in simulation, see Sec-
568 tion 8.2.2. The particles which do reach the calorimeter deposit their energy into
569 several adjacent cells, which are then clustered together. The energy of the clus-
570 ter is then the total energy deposited by that particle. Comparing the response of
571 hadrons in data to that of simulated hadrons provides a direct evaluation of the
572 showering of hadronic particles and the energy deposited by particles in matter
573 (Section 8.2.4).

574 The above studies all use an inclusive selection of charged particles, which are
575 comprised predominantly of pions, kaons, and (anti)protons. It is also possible to
576 measure the response to various identified particle types separately to evaluate
577 the simulated interactions of each particle, particularly at low energies where
578 differences between species are very relevant. Pions and (anti)protons can be
579 identified through decays of long-lived particles, in particular Λ , $\bar{\Lambda}$, and K_S^0 , and
580 then used to measure response as described above. This is discussed in detail in
581 Section 8.3.

582 The results in this chapter use data collected at 7 and 8 TeV collected in 2010
583 and 2012, respectively. Both are included as the calorimeter was repaired and
584 recalibrated between those two data-taking periods. Both sets of data are com-
585 pared to an updated simulation that includes new physics models provided by
586 Geant4 [1] and improvements in the detector description [2, 3]. The present
587 results are published in European Physical Journal C (EPJC) [4] and can be com-
588 pared to a similar measurement performed in 2009 and 2010 [5], which used the
589 previous version of the simulation framework [6].

590 8.1 DATASET AND SIMULATION

591 8.1.1 DATA SAMPLES

592 The two datasets used in this chapter are taken from dedicated low-pileup runs
 593 where the fraction of events with multiple interactions was negligible. These
 594 datasets are used rather than those containing full-pileup events to facilitate mea-
 595 surement of isolated hadrons. The 2012 dataset at $\sqrt{s} = 8$ TeV contains 8 mil-
 596 lion events and corresponds to an integrated luminosity of 0.1 nb^{-1} . The 2010
 597 dataset at $\sqrt{s} = 7$ TeV contains 3 million events and corresponds to an inte-
 598 grated luminosity of 3.2 nb^{-1} . The latter dataset was also used for the 2010 re-
 599 sults [5], but it has since been reanalyzed with an updated reconstruction includ-
 600 ing the final, best understanding of the detector description for the material and
 601 alignment from Run 1.

602 8.1.2 SIMULATED SAMPLES

603 The two datasets above are compared to simulated single-, double-, and non-
 604 diffractive events generated with Pythia8 [7] using the A2 configuration of
 605 hadronization [8] and the MSTW 2008 parton-distribution function set [9, 10].
 606 The admixture of the single-, double-, and non-diffractive events uses the default
 607 relative contributions from Pythia8. The conditions and energies for the two
 608 simulations are chosen so that they match those of the corresponding dataset.

609 To evaluate the interaction of hadrons with detector material, the simulation
 610 uses two different collections of hadronic physics models, called physics lists, in
 611 Geant4 9.4 [11]. The first, QGSP_BERT, combines the Bertini intra-nuclear
 612 cascade [12–14] below 9.9 GeV, a parametrized proton inelastic model from 9.5
 613 to 25 GeV [15], and a quark-gluon string model above 12 GeV [16–20]. The
 614 second, FTFP_BERT, combines the Bertini intra-nuclear cascade [12–14] below
 615 5 GeV and the Fritiof model [21–24] above 4 GeV. In either list, Geant4 en-
 616 forces a smooth transition between models where multiple models overlap.

617 8.1.3 EVENT SELECTION

618 The event selection for this study is minimal, as the only requirement is selecting
 619 good-quality events with an isolated track. Such events are triggered by requir-
 620 ing at least two hits in the minimum-bias trigger scintillators. After trigger, each
 621 event is required to have exactly one reconstructed vertex, and that vertex is re-
 622 quired to have four or more associated tracks.

623 The particles which are selected for the response measurements are first iden-
 624 tified as tracks in the inner detector. The tracks are required to have at least 500
 625 MeV of transverse momentum. To ensure a reliable momentum measurement,
 626 these tracks are required to have at least one hit in the pixel detector, six hits in
 627 the SCT, and small longitudinal and transverse impact parameters with respect
 628 to the primary vertex [5]. For the majority of the measurements in this chapter,
 629 the track is additionally required to have 20 hits in the TRT, which significantly

630 reduces the contribution from tracks which undergo nuclear interactions. This
 631 requirement and its effect is discussed in more detail in Section 8.2.5. In addition,
 632 tracks are rejected if there is any other reconstructed track which extrapolates
 633 to the calorimeter within a cone of $\Delta R = \sqrt{(\Delta\phi)^2 + (\Delta\eta)^2} < 0.4$. This require-
 634 ment guarantees that the contamination of energy from nearby charged particles
 635 is negligible [5].

636 8.2 INCLUSIVE HADRON RESPONSE

637 The calorimeter response is more precisely defined as the ratio of the measured
 638 calorimeter energy to the true energy carried by the particle, although this true
 639 energy is unknown. For charged particles, however, the inner detector provides
 640 a very precise measurement of momentum (with uncertainty less than 1%) that
 641 can be used as a proxy for true energy. The ratio of the energy deposited by
 642 the charged particle in the calorimeter, E , to its momentum measured in the
 643 inner detector p , forms the calorimeter response measure called E/p . Though
 644 the distribution of E/p contains a number of physical features, this study focuses
 645 on the trends in two aggregated quantities: $\langle E/p \rangle$, the average of E/p for the
 646 selected tracks, and the zero fraction, the fraction of tracks with no associated
 647 energy in the calorimeter for those tracks.

648 The calorimeter energy assigned to a track is defined using clusters. The clus-
 649 ters are formed using a 4–2–0 algorithm [25] that begins with seeds requiring
 650 at least 4 times the average calorimeter cell noise. The neighboring cells with
 651 at least twice that noise threshold are then added to the cluster, and all bound-
 652 ing cells are then added with no requirement. This algorithm minimizes noise
 653 contributions through its seeding process, and including the bounding cells im-
 654 proves the energy resolution [26]. The clusters are associated to a given track
 655 if they fall within a cone of $\Delta R = 0.2$ of the extrapolated position of the track,
 656 which includes about 90% of the energy on average [5]. This construction is il-
 657 lustrated in Figure 2.

658 8.2.1 E/P DISTRIBUTION

659 The E/p distributions measured in both data and simulation are shown in Fig-
 660 ure 3 for two example bins of track momentum and for tracks in the central
 661 region of the detector. These distributions show several important features of
 662 the E/p observable. The large content in the bin at $E = 0$ comes from tracks that
 663 have no associated cluster, which occurs due to interactions with detector mate-
 664 rial prior to reaching the calorimeter or the energy deposit being insufficiently
 665 large to generate a seed, and are discussed in Section 8.2.2. The small negative
 666 tail also comes from tracks that do not deposit any energy in the calorimeter but
 667 are randomly associated to a cluster with an energy below the noise threshold.
 668 The long positive tail above 1.0 comes from the contribution of neutral parti-
 669 cles. Nearby neutral particles deposit (sometimes large) additional energy in the
 670 calorimeter but do not produce tracks in the inner detector, so they cannot be
 671 rejected by the track isolation requirement. Additionally the peak and mean of

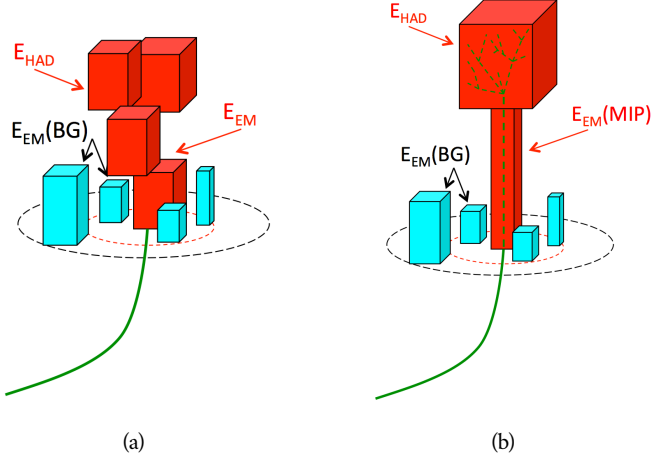


Figure 2: An illustration (a) of the E/p variable used throughout this paper. The red energy deposits come from the charged particle targeted for measurement, while the blue energy deposits are from nearby neutral particles and must be subtracted. The same diagram (b) for the neutral-background selection, described in Section 8.2.3.

the distribution falls below 1.0 because of the loss of energy not found within the cone as well as the non-compensation of the calorimeter.

The data and simulation share the same features, but the high and low tails are significantly different. The simulated events tend to overestimate the contribution of neutral particles to the long tail, an effect which can be isolated and removed as discussed in Section 8.2.3. Additionally, the simulated clusters have less noise on average, although this is a small effect on the overall response.

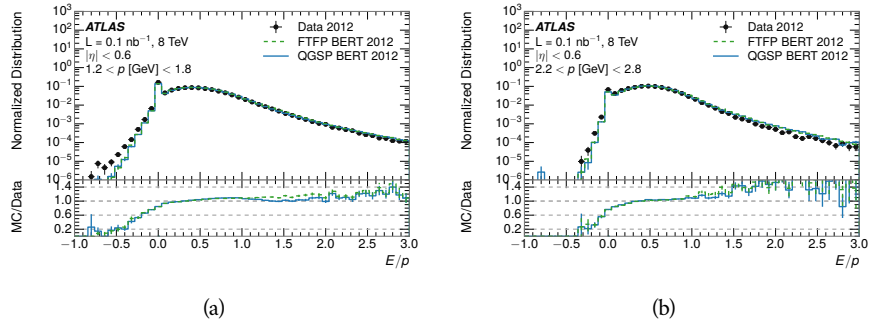


Figure 3: The E/p distribution and ratio of simulation to data for isolated tracks with (a) $|\eta| < 0.6$ and $1.2 < p/\text{GeV} < 1.8$ and (b) $|\eta| < 0.6$ and $2.2 < p/\text{GeV} < 2.8$.

8.2.2 ZERO FRACTION

The fraction of particles with no associated clusters, or similarly those with $E \leq 0$, reflects the modeling of both the detector geometry and hadronic interactions. The zero fraction is expected to rise as the amount of material a particle traverses

increases, while it is expected to decrease as the particle energy increases. This dependence can be seen in Figure 4, where the zero fraction in data and simulation is shown as a function of momentum and the amount of material measured in interaction lengths. The trends are similar between 2010 and 2012 and for positively and negatively charged particles. The zero fraction decreases with energy as expected. The absolute discrepancy in zero fraction decreases with momentum from 5% to less than 1%, but this becomes more pronounced in the ratio as the zero fraction shrinks quickly with increasing momentum. There is a small constant difference between the data and simulation in both interaction models that becomes more pronounced. The amount of material in the detector increases with η , which is used to obtain results for interaction lengths ranging between 0.1 and 0.65 λ . As the data and simulation have significant disagreement in the zero fraction over a number of interaction lengths, the difference must be primarily from the modeling of hadronic interactions with detector material and not just the detector geometry. Although two different hadronic interaction models are shown in the figure, they have very similar discrepancies to data because both use the same description (the BERT model) at low momentum.

8.2.3 NEUTRAL BACKGROUND SUBTRACTION

The isolation requirement on hadrons is only effective in removing an energy contribution from nearby charged particles. Nearby neutral particles, predominantly photons from π^0 decays, also add their energy to the calorimeter clusters, but mostly in the electromagnetic calorimeter. It is possible to measure this contribution, on average, using late-showering hadrons that minimally ionize in the electromagnetic calorimeter. Such particles are selected by requiring that they deposit less than 1.1 GeV in the EM calorimeter within a cone of $\Delta R < 0.1$ around the track. To ensure that these particles are well measured, they are additionally required to deposit between 40% and 90% of their energy in the hadronic calorimeter within the same cone.

These particles provide a clean sample to measure the nearby neutral background because they do not deposit energy in the area immediately surrounding them in the EM calorimeter, as shown in Figure 2. So, the energy deposits in the region $0.1 < \Delta R < 0.2$ can be attributed to neutral particles alone. To estimate the contribution to the whole cone considered for the response measurement, that energy is scaled by a geometric factor of 4/3. This quantity, $\langle E/p \rangle_{BG}$, measured in aggregate over a number of particles, gives the contribution to $\langle E/p \rangle$ from neutral particles in the EM calorimeter. Similar techniques were used in the individual layers of the hadronic calorimeters to show that the background from neutrals is negligible in those layers [5].

The distribution of this background estimate is shown in Figure 5 for data and simulation with the two different physics lists. The contribution from neutral particles falls from 0.1 at low momentum to around 0.03 for particles above 7 GeV. Although the simulation captures the overall trend, it significantly overestimates the neutral contribution for tracks with momentum between 2 and 8 GeV. This effect was also seen in the tails of the E/p distributions in Figure 3.

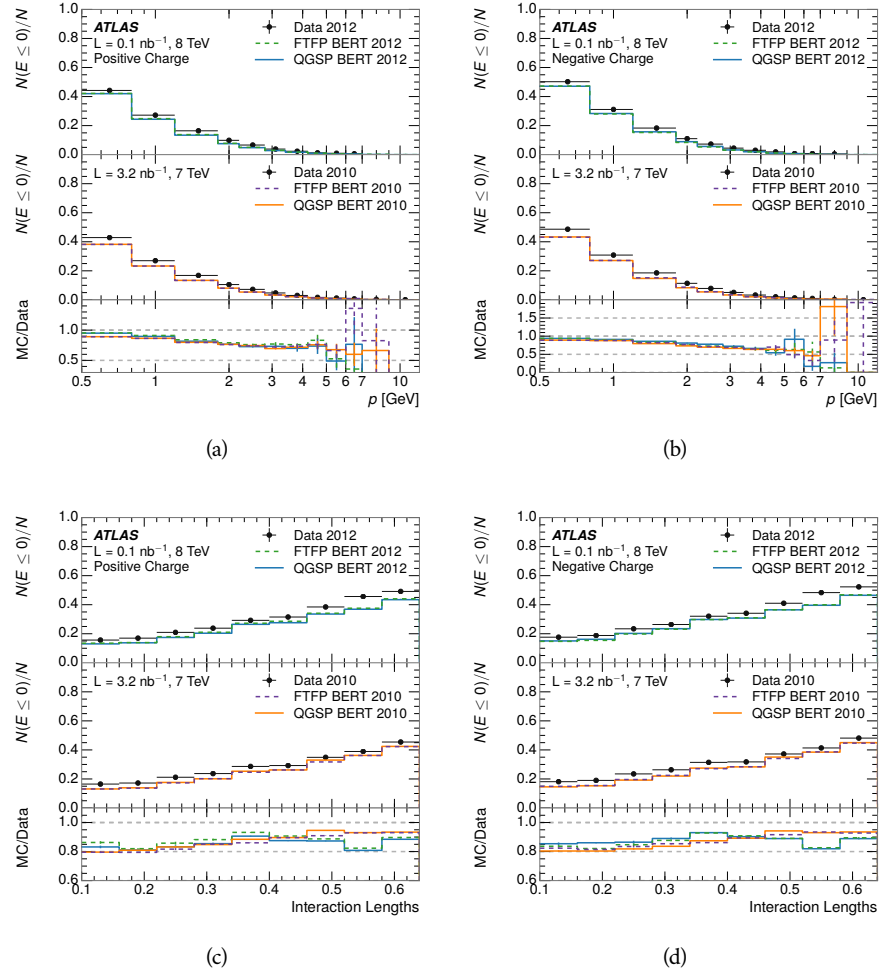


Figure 4: The fraction of tracks as a function (a, b) of momentum, (c, d) of interaction lengths with $E \leq 0$ for tracks with positive (on the left) and negative (on the right) charge.

This difference is likely due to modeling of coherent neutral particle radiation in Pythia8 that overestimates the production of π^0 near the production of the charged particles. The discrepancy does not depend on η and thus is unlikely to be a mismodeling of the detector. This difference can be subtracted to form a corrected average E/p , as in Section 8.2.4.

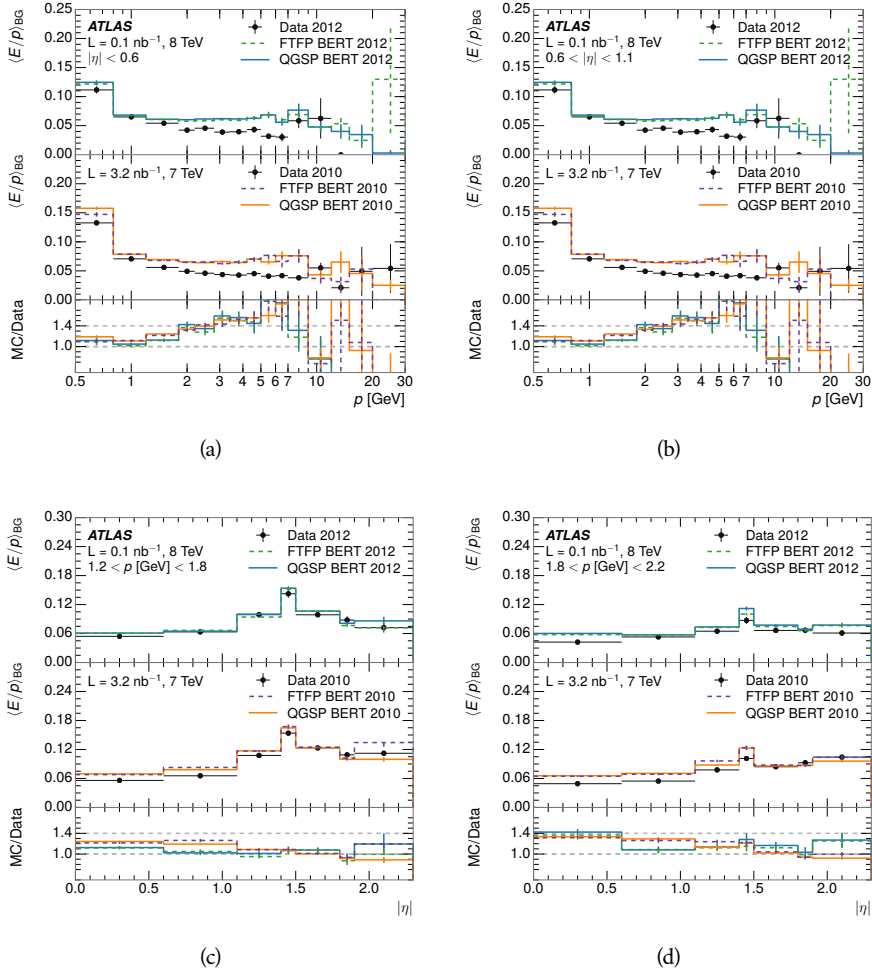


Figure 5: $\langle E/p \rangle_{\text{BG}}$ as a function of the track momentum for tracks with (a) $|\eta| < 0.6$, (b) $0.6 < |\eta| < 1.1$, and as a function of the track pseudorapidity for tracks with (c) $1.2 < p/\text{GeV} < 1.8$, (d) $1.8 < p/\text{GeV} < 2.2$.

8.2.4 CORRECTED RESPONSE

Figure 6 shows $\langle E/p \rangle_{\text{COR}}$ as a function of momentum for several bins of pseudorapidity. This corrected $\langle E/p \rangle_{\text{COR}} \equiv \langle E/p \rangle - \langle E/p \rangle_{\text{BG}}$ measures the average calorimeter response without the contamination of neutral particles. It is the most direct measurement of calorimeter response in that it is the energy measured for fully isolated hadrons. The correction is performed separately in data and simulation, so that the mismodeling of the neutral background in simulation is removed from the comparison of response. The simulation overestimates the

740 response at low momentum by about 5%, an effect that can be mostly attributed
 741 to the underestimation of the zero fraction mentioned previously. For $|\eta| < 0.6$,
 742 the data-simulation agreement has a larger discrepancy by about 5% for 2010
 743 than 2012, although this is not reproduced in at higher pseudorapidity.

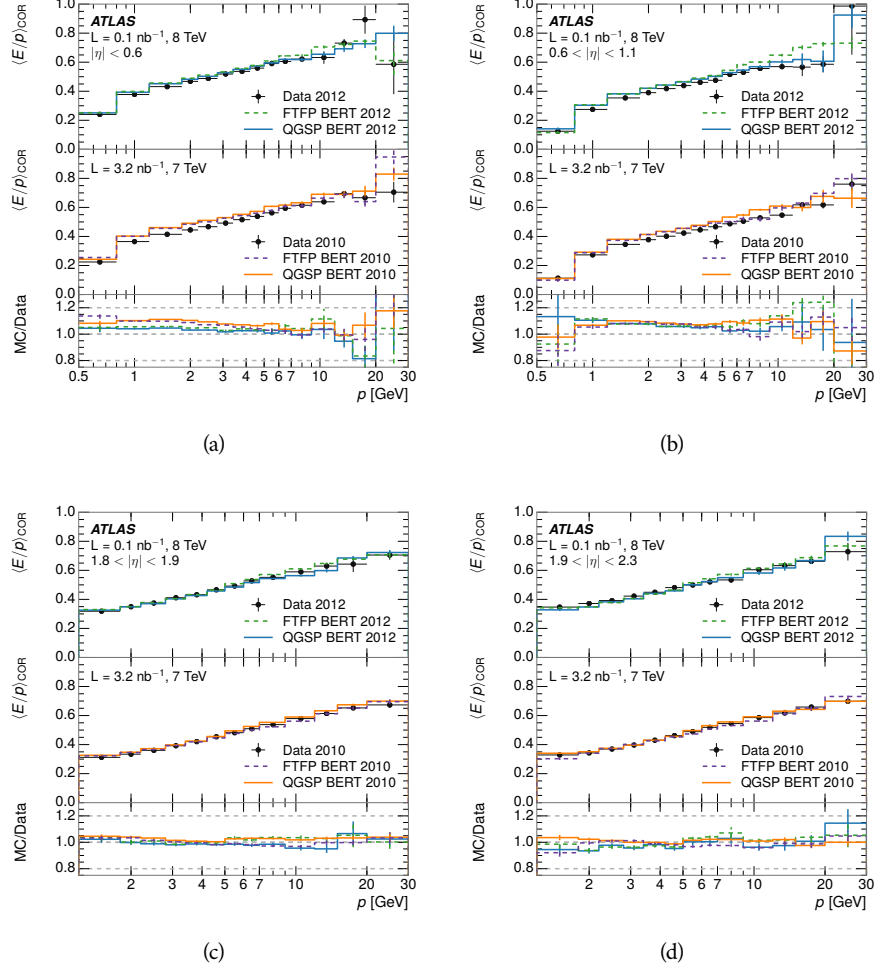


Figure 6: $\langle E/p \rangle_{\text{COR}}$ as a function of track momentum, for tracks with (a) $|\eta| < 0.6$, (b) $0.6 < |\eta| < 1.1$, (c) $1.8 < |\eta| < 1.9$, and (d) $1.9 < |\eta| < 2.3$.

744 The response measurement above used topological clustering at the EM scale,
 745 that is clusters were formed to measure energy but no corrections were applied
 746 to correct for expected effects like energy lost outside of the cluster or in unin-
 747 strumented material. It is also interesting to measure $\langle E/p \rangle_{\text{COR}}$ using local clus-
 748 ter weighted ([LCW](#)) energies, which accounts for those effects by calibrating the
 749 energy based on the properties of the cluster such as energy density and depth in
 750 the calorimeter. Figure 7 shows these distributions for tracks with zero or more
 751 clusters and separately for tracks with one or more clusters. The calibration
 752 moves the mean value of $\langle E/p \rangle_{\text{COR}}$ significantly closer to 1.0 as desired. The
 753 agreement between data and simulation improves noticeably when at least one
 754 cluster is required, as this removes the contribution from the mismodeling of
 755 the zero fraction. The good agreement in that case again demonstrates that the

difference in $\langle E/p \rangle_{\text{COR}}$ between data and simulation is caused predominantly by the difference in zero fraction.

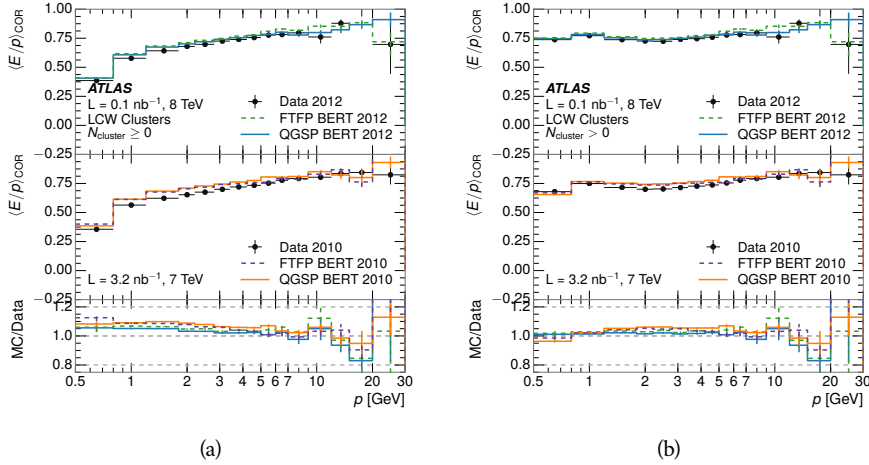


Figure 7: $\langle E/p \rangle_{\text{COR}}$ calculated using LCW-calibrated topological clusters as a function of track momentum for tracks with (a) zero or more associated topological clusters or (b) one or more associated topological clusters.

8.2.5 ADDITIONAL STUDIES

As has been seen in several measurements in previous sections, the simulation does not correctly model the chance of a low momentum hadron to reach the calorimeter. Because of the consistent discrepancy across pseudorapidity and interaction lengths, this can be best explained by incomplete understanding of hadronic interactions with the detector [4]. For example, a hadron that scatters off of a nucleus in the inner detector can be deflected through a significant angle and not reach the expected location in the calorimeter. In addition, these interactions can produce secondary particles that are difficult to model.

The requirement used throughout the previous sections on the number of hits in the TRT reduces these effects by preferentially selecting tracks that do not undergo nuclear interactions. It is interesting to check how well the simulation models tracks with low numbers of TRT hits, which selects tracks that are more likely to have undergone a hadronic interaction. Figure 8 compares the distributions with $N_{\text{TRT}} < 20$ to $N_{\text{TRT}} > 20$ for real and simulated particles. As expected, the tracks with fewer hits are poorly modeled in the simulation as $\langle E/p \rangle_{\text{COR}}$ differs by as much as 25% at low momentum.

Another interesting aspect of the simulation is the description of antiprotons at low momentum, where QGSP_BERT and FTFP_BERT have significant differences. This can be seen to have an effect in the inclusive response measurement when separated into positive and negative charge. The $\langle E/p \rangle_{\text{COR}}$ distributions for positive and negative particles are shown in Figure 9, where a small difference between QGSP_BERT and FTFP_BERT can be seen in the distribution for negative tracks. This is demonstrated more clearly in Figure 10, which shows

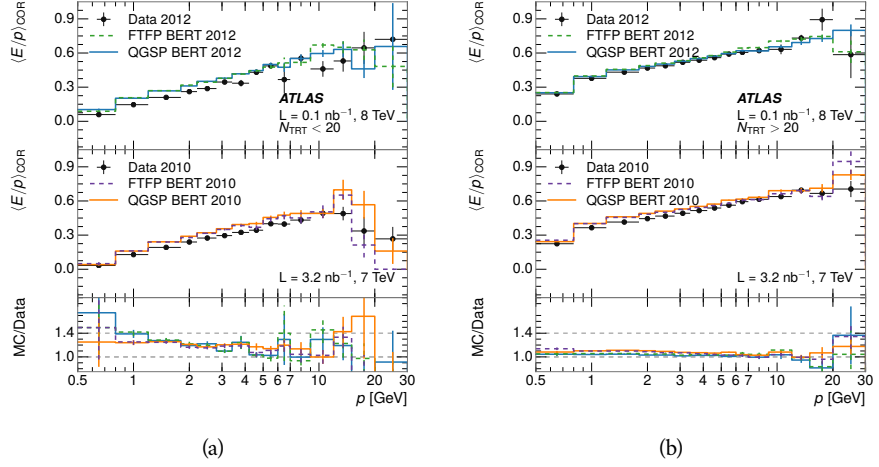


Figure 8: Comparison of the $\langle E/p \rangle_{\text{COR}}$ for tracks with (a) less than and (b) greater than 20 hits in the TRT.

the E/p distribution in the two simulations separated by charge. There is a clear difference around $E/p > 1.0$, which can be explained by the additional energy deposited by the annihilation of the antiproton in the calorimeter that is modeled well only in FTFP_BERT. This is also explored with data using identified antiprotons in Section 8.3.

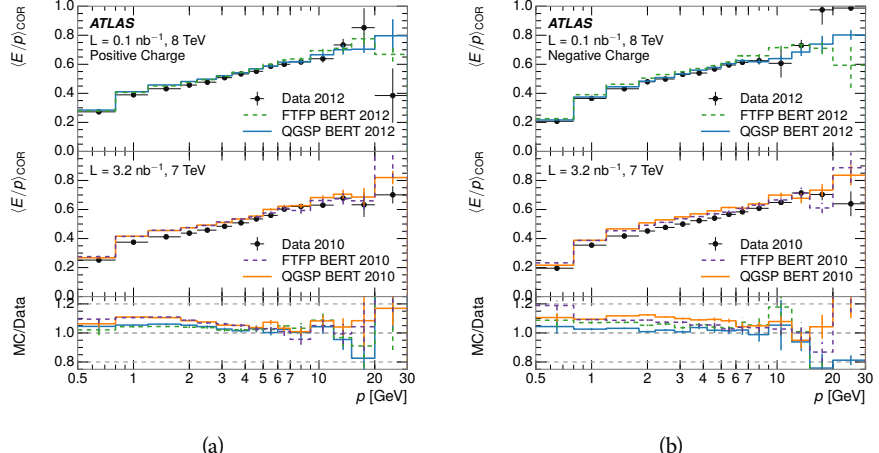


Figure 9: Comparison of the $\langle E/p \rangle_{\text{COR}}$ for (a) positive and (b) negative tracks as a function of track momentum for tracks with $|\eta| < 0.6$.

The $\langle E/p \rangle$ results in previous sections have considered the electromagnetic and hadronic calorimeters together as a single energy measurement, to emphasize the total energy deposited for a given particle. However, the deposits in each calorimeter are available separately and $\langle E/p \rangle$ can be constructed for each layer. As the layers are composed of different materials and are modeled separately in the detector geometry, confirmation that the simulation matches the data well

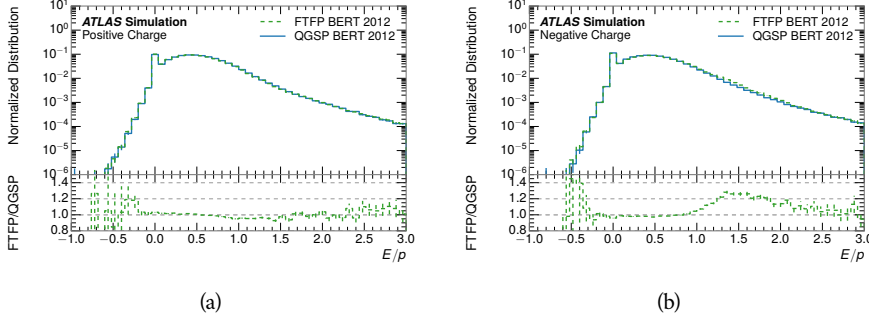


Figure 10: Comparison of the E/p distributions for (a) positive and (b) negative tracks with $0.8 < p/\text{GeV} < 1.2$ and $|\eta| < 0.6$, in simulation with the FTFP_BERT and QGSP_BERT physics lists.

in each layer adds confidence in both the description of hadronic interactions with the two different materials and also the geometric description of each.

The technique discussed in Section 8.2.3 for selecting minimally ionizing particle (MIP)s in the electromagnetic calorimeter is also useful in studying deposits in the hadronic calorimeter. Those MIPs deposit almost all of their energy exclusively in the hadronic calorimeter. Figure 11 shows $\langle E/p \rangle_{\text{RAW}}^{\text{Had}}$, where RAW indicates that no correction has been applied for neutral backgrounds and Had indicates that only clusters for the hadronic calorimeter are included. The RAW and COR versions of $\langle E/p \rangle$ in this case are the same, as the neutral background is negligible in that calorimeter layer. The distributions are shown both for the original EM scale calibration and after LCW calibration. The data and simulation agree very well in this comparison, except in the lowest momentum bin which has 5% discrepancy that has already been seen in similar measurements.

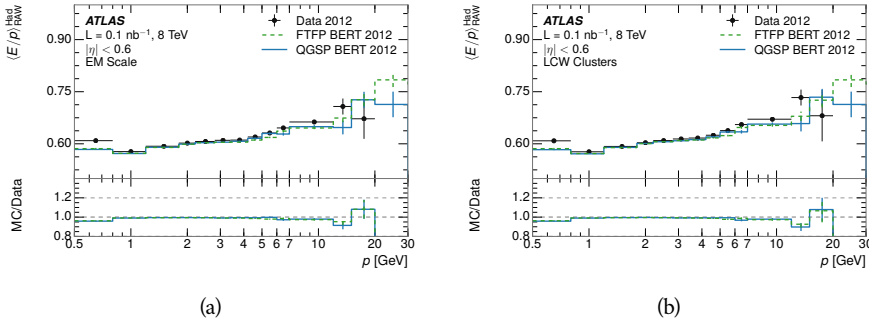


Figure 11: Comparison of the response of the hadronic calorimeter as a function of track momentum (a) at the EM-scale and (b) after the LCW calibration.

A similar comparison can be made in the electromagnetic calorimeter by selecting particles which have no associated energy in the hadronic calorimeter. These results are measured in terms of $\langle E/p \rangle_{\text{COR}}^{\text{EM}}$, where EM designates that only clusters in the electromagnetic calorimeter are included and COR designates that the neutral background is subtracted as the neutral background is present in this case. Figure 12 shows the analogous comparisons to Figure 11 in

812 the electromagnetic calorimeter. In this case the disagreement between data and
 813 simulation is more pronounced, with discrepancies as high as 5% over a larger
 814 range of momenta. This level of discrepancy indicates that the description of
 815 the electromagnetic calorimeter is actually the dominant source of discrepancy
 816 in the combined distributions in Section 8.2.4.

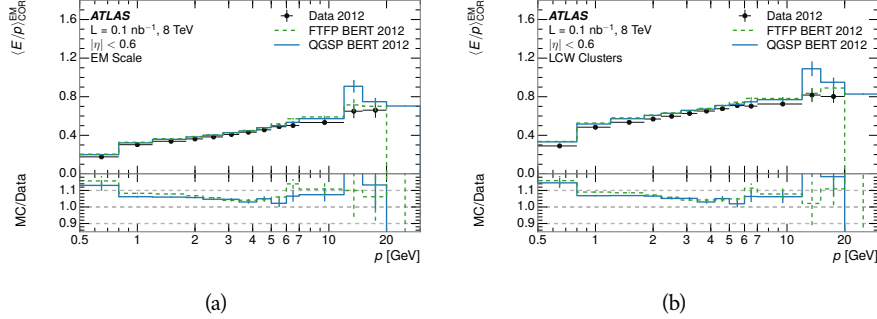


Figure 12: Comparison of the response of the EM calorimeter as a function of track momentum (a) at the EM-scale and (b) with the LCW calibration.

817 **NOTE: There are more studies that I skipped for brevity that could be in-**
 818 **cluded if interesting. E/p at different cluster threshold settings, E/p with**
 819 **pileup, E/p with cells. I also left out a lot of eta bins that appear in the**
 820 **paper so that this section didn't turn into 20 pages of plots.**

821 8.3 IDENTIFIED PARTICLE RESPONSE

822 The inclusive response measurement for hadrons can be augmented by measur-
 823 ing the response for specific particle species. The simulation models each parti-
 824 cle type separately, and understanding the properties of each is important in con-
 825 straining the uncertainty on jets. In order to select and measure specific hadrons,
 826 this section relies on the displaced decays of long-lived particles. Such decays
 827 can be identified by reconstructing secondary vertices with a requirement on
 828 mass. In particular, Λ , $\bar{\Lambda}$, and K_S^0 can be used to select a pure sample of protons,
 829 antiprotons, and pions, respectively.

830 8.3.1 DECAY RECONSTRUCTION

831 The measurement of response for identified particles uses the same selection as
 832 for inclusive particles (Section 8.1.3) with a few additions. Each event used is
 833 required to have at least one secondary vertex, and the tracks are required to
 834 match to that vertex rather than the primary vertex. Pions are selected from
 835 decays of $K_S^0 \rightarrow \pi^+ \pi^-$, which is the dominant decay for K_S^0 to charged particles.
 836 Protons are selected from decays of $\Lambda \rightarrow \pi^- p$ and antiprotons from $\bar{\Lambda} \rightarrow \pi^+ \bar{p}$,
 837 which are similarly the dominant decays of Λ and $\bar{\Lambda}$ to charged particles. The
 838 species of parent hadron in these decays is determined by reconstructing the
 839 mass of the tracks associated to the secondary vertex. The sign of the higher

momentum decay particle can distinguish between Λ and $\bar{\Lambda}$, which of course have the same mass, as the proton or antiproton is kinematically favored to have higher momentum. Examples of the reconstructed masses used to select these decays are shown in Figure 13.

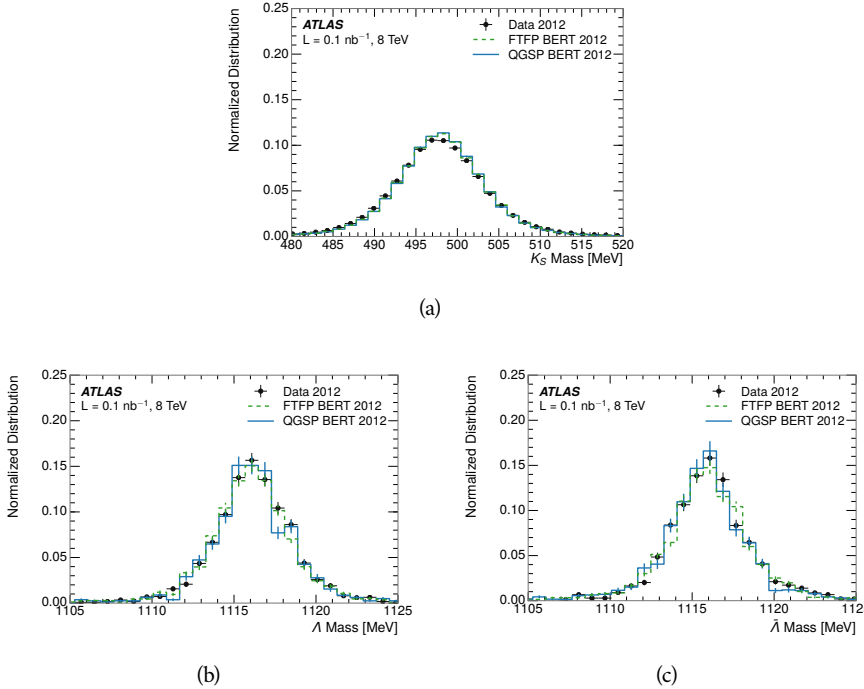


Figure 13: The reconstructed mass peaks of (a) K_S^0 , (b) Λ , and (c) $\bar{\Lambda}$ candidates.

The dominant backgrounds for the identified particle decays are nuclear interactions and combinatoric sources. These are suppressed by the kinematic requirements on the tracks as well as an additional veto which removes candidates that are consistent with both a Λ or $\bar{\Lambda}$ and a K_S^0 hypothesis, which is possible because of the different assumptions on particle mass in each case [5]. After these requirements, the backgrounds are found to be negligible compared to the statistical errors on these measurements.

8.3.2 IDENTIFIED RESPONSE

With these techniques the E/p distributions are extracted in data and simulation for each particle species and shown in Figure 14. These distributions are shown for a particular bin of E_a ($2.2 < E_a/\text{GeV} < 2.8$), rather than p . E_a is the energy available to be deposited in the calorimeter: for pions $E_a = \sqrt{p^2 + m^2}$, for protons $E_a = \sqrt{p^2 + m^2} - m$, and for antiprotons $E_a = \sqrt{p^2 + m^2} + m$. The features of the E/p distributions are similar to the inclusive case. There is a small negative tail from noise and a large fraction of tracks with zero energy from particles which do not reach the calorimeter. The long positive tail is noticeably more pronounced for antiprotons because of the additional energy generated by the annihilation in addition to the neutral background.

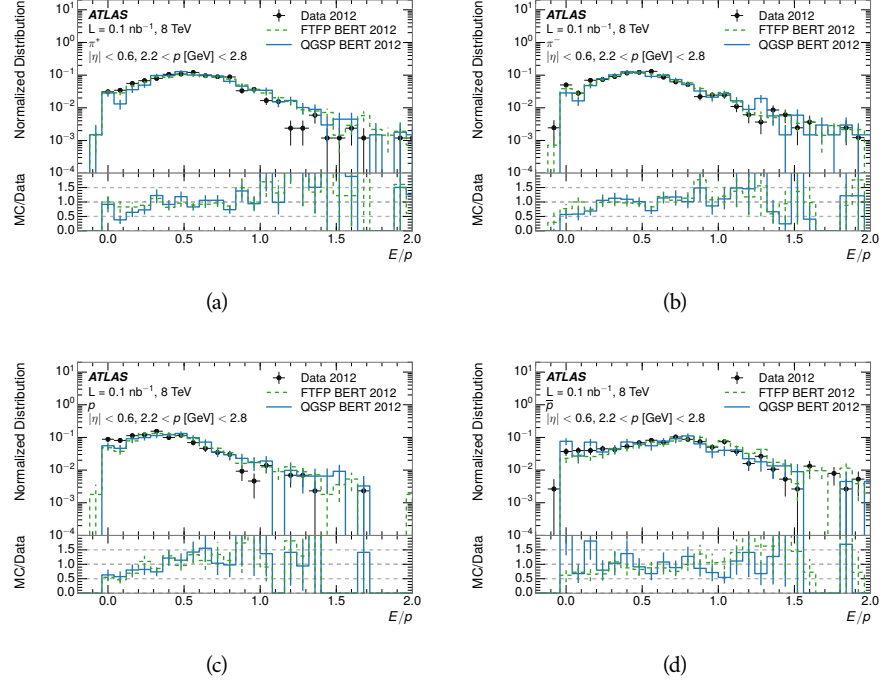


Figure 14: The E/p distribution for isolated (a) π^+ , (b) π^- , (c) proton, and (d) anti-proton tracks.

862 The zero fraction is further explored in Figure 15 for pions and protons in data
 863 and simulation. The simulation consistently underestimates the zero fraction
 864 independent of particle species, which implies that this discrepancy is not caused
 865 by the model of a particular species but rather a feature common to all.

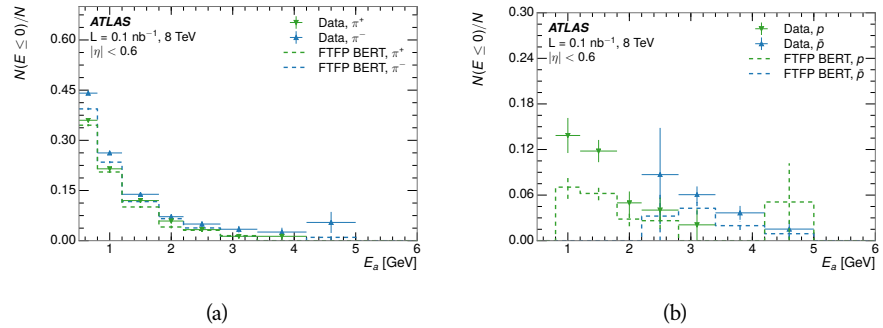


Figure 15: The fraction of tracks with $E \leq 0$ for identified (a) π^+ and π^- , and (b) proton and anti-proton tracks

866 It is also interesting to compare the response between the different particle
 867 species. One approach to do this is to measure the difference in $\langle E/p \rangle$ between
 868 two types, which has the advantage of removing the neutral background. These
 869 differences are shown in various combinations in Figure 16. The response for
 870 π^+ is greater on average than the response to π^- because of a charge-exchange
 871 effect which causes the production of additional neutral pions in the showers of

872 π^+ [27]. The response for π^+ is also greater on average than the response to p ,
 873 because a large fraction of the energy of π^+ hadrons is converted to an electro-
 874 magnetic shower [28, 29]. However, the \bar{p} response is significantly higher than
 875 the response to π^- because of the annihilation of the antiproton. FTFP_BERT
 876 does a better job of modeling this effect than QGSP_BERT because of their differ-
 877 ent descriptions of \bar{p} interactions with material.

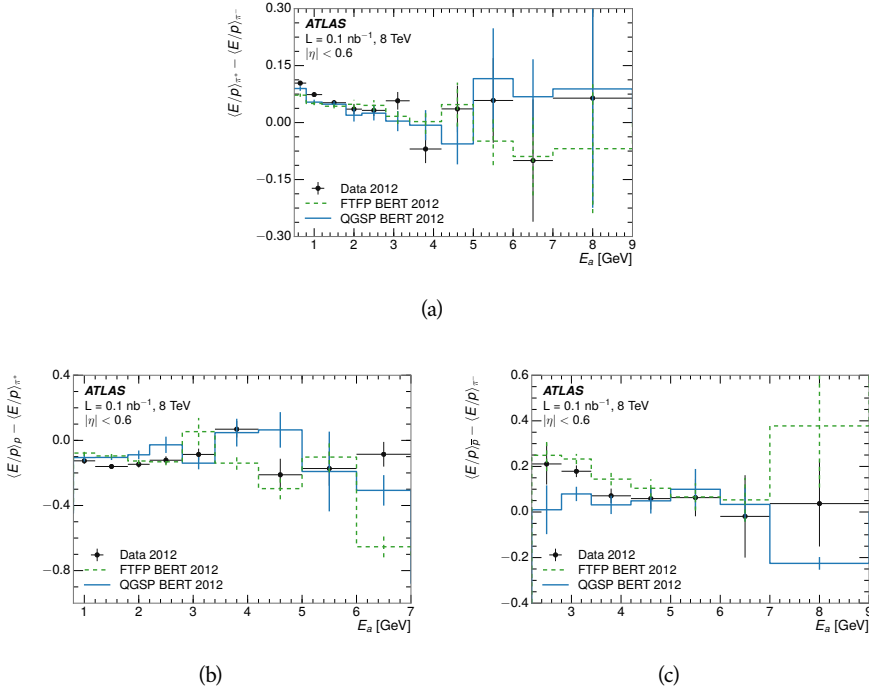


Figure 16: The difference in $\langle E/p \rangle$ between (a) π^+ and π^- (b) p and π^+ , and (c) \bar{p} and π^- .

878 It is also possible to remove the neutral background from these response dis-
 879 tributions using the same technique as in Section 8.2.3. The technique is largely
 880 independent of the particle species and so can be directly applied to $\langle E/p \rangle$ for
 881 pions. The $\langle E/p \rangle_{\text{COR}}$ distributions for pions are shown in Figure 17, which are
 882 very similar to the inclusive results. The inclusive hadrons are comprised mostly
 883 of pions, so this similarity is not surprising. It is also possible to see the small
 884 differences between π^+ and π^- response here, where $\langle E/p \rangle_{\text{COR}}$ is higher on av-
 885 erage for π^+ . The agreement between data and simulation is significantly worse
 886 for the π^- distributions than for the π^+ , with a discrepancy greater than 10%
 887 below 2-3 GeV.

888 8.3.3 ADDITIONAL SPECIES IN SIMULATION

889 The techniques above provide a method to measure the response separately for
 890 only pions and protons. However the hadrons which forms jets include a num-
 891 ber of additional species such as kaons and neutrons. The charged kaons are
 892 an important component of the inclusive charged hadron distribution, which is
 893 comprised of roughly 60-70% pions, 15-20% kaons, and 5-15% protons. These

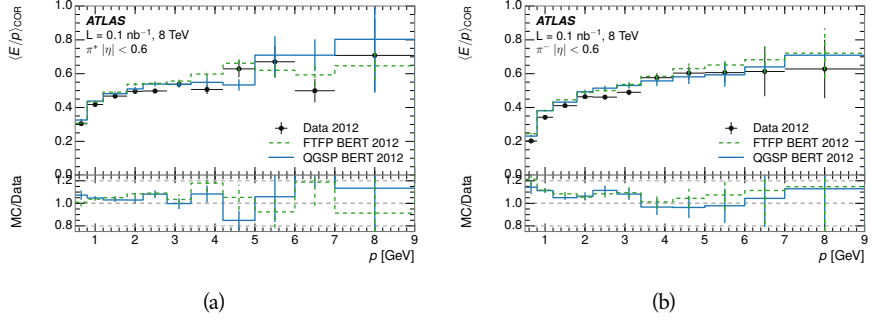


Figure 17: $\langle E/p \rangle_{\text{COR}}$ as a function of track momentum for (a) π^+ tracks and (b) π^- tracks.

are difficult to measure in data at the ATLAS detector, although a template subtraction technique has been proposed which may be effective with larger sample sizes [4]. The simulation of these particles includes noticeable differences in response at low energies, which are shown in Figure 18 for FTFP_BERT. The significant differences in response between low energy protons and antiprotons are accounted for above in the definitions of E_a .

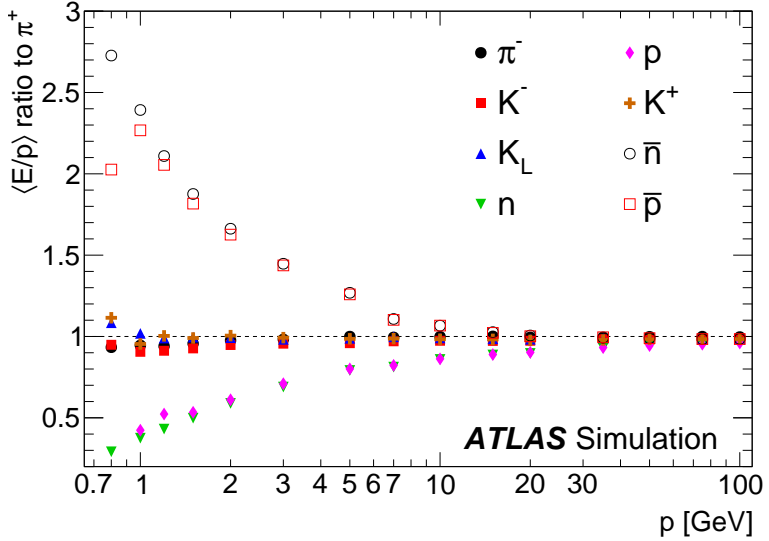


Figure 18: The ratio of the calorimeter response to single particles of various species to the calorimeter response to π^+ with the physics list FTFP_BERT.

900 8.4 SUMMARY

These various measurements of calorimeter response shown above for data and simulation illuminate the accuracy of the simulation of hadronic interactions at the ATLAS detector. The results were done using 2010 and 2012 data at 7 and 8 TeV, but reflect the most current understanding of the detector alignment and geometry. A number of measurements focusing on a comparison between pro-

906 tons and antiprotons suggest that FTFP_BERT models those interaction more
907 accurately than QGSP_BERT. These measurements, among others, were the moti-
908 vation to switch the default Geant4 simulation from FTFP_BERT to QGSP_BERT
909 for all ATLAS samples.

910 Even with these updates, there are a number of small, approximately 5%, dis-
911 crepancies in response between the data and simulation at low energies. At
912 higher energies the simulation of hadronic interactions is very consistent with
913 data. Chapter 9 discusses how to use these observed differences to constrain the
914 jet energy scale and its associated uncertainties.

915

916 JET ENERGY RESPONSE AND UNCERTAINTY

917 9.1 MOTIVATION

918 As jets form a major component of many physics analyses at ATLAS, it is cru-
 919 cial to carefully calibrate the measurement of jet energies and to derive an un-
 920 certainty on that measurement. These uncertainties have often been the dom-
 921 inant systematic uncertainty in high-energy analyses at the Large Hadron Col-
 922 linder ([LHC](#)). Dijet and multijet balance techniques provide a method to constrain
 923 the [JES](#) and its uncertainty in data, and provide the default values used for ATLAS
 924 jet measurements at most energies [30]. These techniques are limited by their re-
 925 liance on measuring jets in data, so they are statistically limited in estimating
 926 the jet energy scale at the highest jet energies. This chapter presents another
 927 method for estimating the jet energy scale and its uncertainty which builds up a
 928 jet from its components and thus can be naturally extended to high jet momen-
 929 tum. Throughout this chapter the jets studied are simulated using [Pythia8](#) with
 930 the CT10 parton distribution set [31] and the AU2 tune [8], and corrections are
 931 taken from the studies including data and simulation in Chapter 8.

932 As described in Section 7.2, jets are formed from topological clusters of energy
 933 in the calorimeters using the anti- k_t algorithm. These clusters originate from a
 934 diverse spectrum of particles, in terms of both species and momentum, leading to
 935 significantly varied jet properties and response between jets of similar produced
 936 momentum. Figure 19 shows the simulated distribution of particles within jets
 937 at a few examples energies. The E/p measurements provide a thorough under-
 938 standing of the dominant particle content of jets, the charged hadrons.

939 9.2 UNCERTAINTY ESTIMATE

940 Simulated jets are not necessarily expected to correctly model the energy de-
 941 posits in the calorimeters, because of the various discrepancies discussed in Chap-
 942 ter 8. To evaluate a jet energy response, the simulated jet energies are compared
 943 to a corrected jet built up at the particle level. Each cluster in a jet is associated
 944 to the truth particle which deposited it, and the energy in that cluster is then
 945 corrected for a number of effects based on measurements in data. The primary
 946 corrections come from the single hadron response measurements in addition
 947 to response measured using the combined test beam which covers higher mo-
 948 mentum particles [32]. These corrections include both a shift (Δ), in order to
 949 make the simulation match the average response in data, and an uncertainty (σ)
 950 associated with the ability to constrain the difference between data and simula-
 951 tion. Some of the dominant sources of uncertainty are itemized in Table 1 with
 952 typical values, and the full list considered is described in detail in the associated

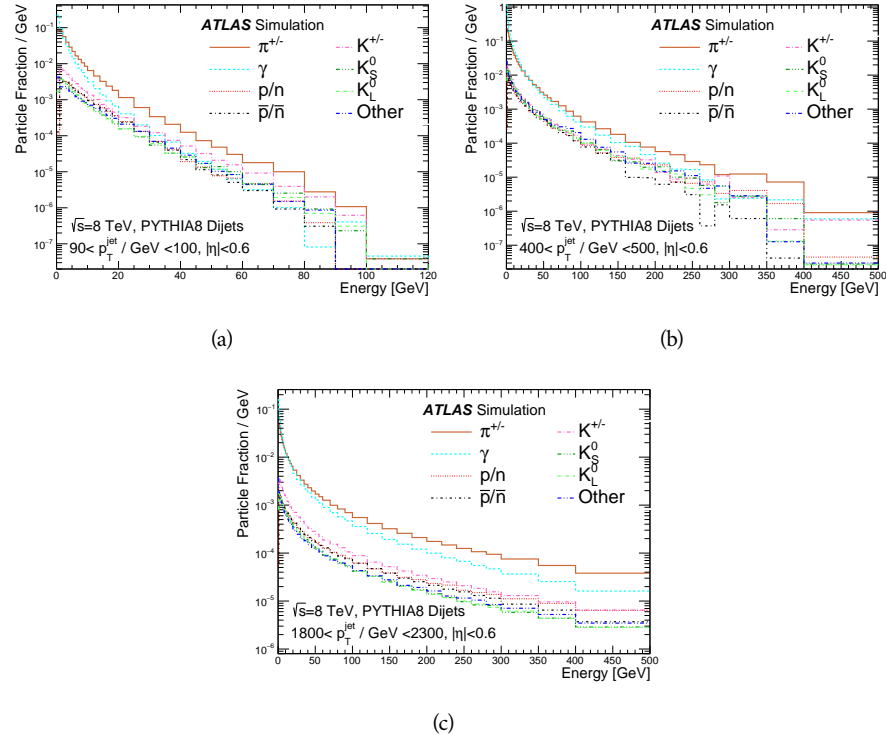


Figure 19: The spectra of true particles inside anti- k_t , $R = 0.4$ jets with (a) $90 < p_T/\text{GeV} < 100$, (b) $400 < p_T/\text{GeV} < 500$, and (c) $1800 < p_T/\text{GeV} < 2300$.

paper [4]. These uncertainties cover differences between the data and simulation in the modeling of calorimeter response to a given particle. No uncertainties are added for the difference between particle composition of jets in data and simulation.

From these terms, the jet energy scale and uncertainty is built up from individual energy deposits in simulation. Each uncertainty term is treated independently, and are taken to be gaussian distributed. The resulting scale and uncertainty is shown in Figure 20, where the mean response is measured relative to the calibrated energy reported by simulation. The dominant uncertainties come from the statistical uncertainties on the E/p measurements at lower energies and the additional uncertainty for out of range measurements at higher energies. The total uncertainty from this method at intermediate jet energies is comparable to other simulation-based methods [33] and is about twice as large as in-situ methods using data [30]. This method is the only one which provides an estimation above 1.8 TeV, however, and so is still a crucial technique in analyses that search for very energetic jets.

These techniques can also be used to measure the correlation between bins of average reconstructed jet momentum across a range of p_T and $|\eta|$, where correlations are expected because of a similarity in particle composition at similar energies. Figure 21 shows these correlations, where the uncertainties on jets in neighboring bins are typically between 30% and 60% correlated. The uncertainty on all jets becomes significantly correlated at high energies and larger pseudora-

Abbrev.	Description	Δ (%)	σ (%)
In situ E/p	The comparison of $\langle E/p \rangle_{\text{COR}}$ as described in Chapter 8 with statistical uncertainties from 500 MeV to 20 GeV.	0-3	1-5
CTB	The main $\langle E/p \rangle$ comparison uncertainties, binned in p and $ \eta $, as derived from the combined test beam results, from 20 to 350 GeV [32].	0-3	1-5
E/p Zero Fraction	The difference in the zero-fraction between data and MC simulation from 500 MeV to 20 GeV.	5-25	1-5
E/p Threshold	The uncertainty in the EM calorimeter response from the potential mismodeling of threshold effects in topological clustering.	0	0-10
Neutral	The uncertainty in the calorimeter response to neutral hadrons based on studies of physics model variations.	0	5-10
K_L	An additional uncertainty in the response to neutral K_L in the calorimeter based on studies of physics model variations.	0	20
E/p Misalignment	The uncertainty in the p measurement from misalignment of the ID.	0	1
Hadrons, $p > 350$ GeV	A flat uncertainty for all particles above the energy range or outside the longitudinal range probed with the combined test beam.	0	10

Table 1: The dominant sources of corrections and systematic uncertainties in the [JES](#) estimation technique, including typical values for the correcting shift (Δ) and the associated uncertainty (σ).

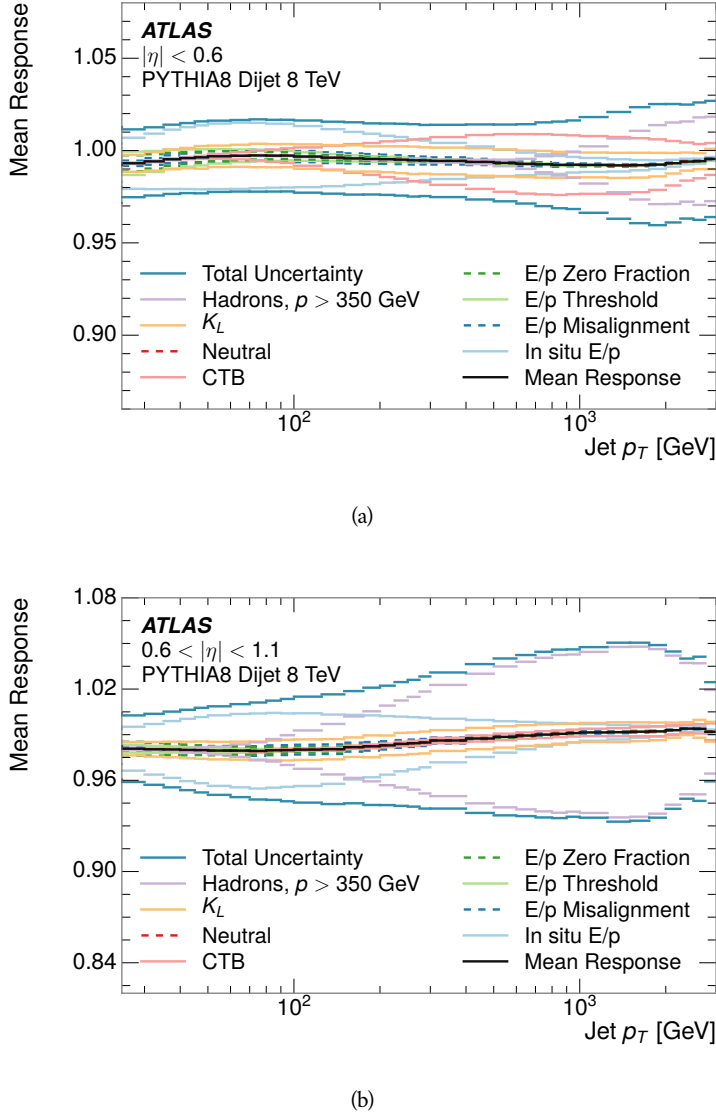


Figure 20: The [JES](#) uncertainty contributions, as well as the total [JES](#) uncertainty, as a function of jet p_T for (a) $|\eta| < 0.6$ and (b) $0.6 < |\eta| < 1.1$.

975 pidities, when the uncertainty becomes dominated by the single term reflecting
 976 out of range particles.

977 9.3 SUMMARY

978 The technique described above provides a jet energy scale and uncertainty by
 979 building up jet corrections from the energy deposits of constituent particles. The
 980 E/p measurements are crucial in providing corrections for the majority of parti-
 981 cles in the jets. The uncertainty derived this way is between 2 and 5% and is about
 982 twice as large at corresponding momentum than jet balance methods. However
 983 this is the only uncertainty available for very energetic jets using 2012 data and
 984 simulation, and repeating this method with Run 2 data and simulation will be

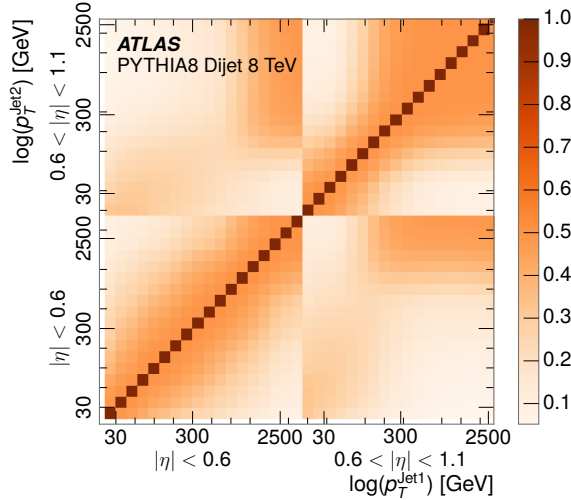


Figure 21: The JES correlations as a function of jet p_T and $|\eta|$ for jets in the central region of the detector.

985 important in providing an uncertainty for the most energetic jets in 13 TeV col-
 986 lisions.

987

PART V

988

SEARCH FOR LONG-LIVED PARTICLES

989

You can put some informational part preamble text here.

990

991 LONG-LIVED PARTICLES IN ATLAS

992 As discussed in Section 2.3, various limitations in the SM suggest a need for new
 993 particles at the TeV scale. A wide range of extensions to the Standard Model
 994 predict that these new particles can have lifetimes greater than approximately
 995 one-hundredth of a nanosecond. These include theories with universal extra-
 996 dimensions [34, 35], with new fermions [36], and with leptoquarks [37]. Many
 997 Supersymmetry (SUSY) theories also produce these Long-Lived Particles (LLPs),
 998 in both R-Parity violating [38–40] and R-Parity conserving [41–44] formula-
 999 tions. Split supersymmetry [45, 46], for example, predicts long-lived gluinos
 1000 with $O(\text{TeV})$ masses. This search focuses specifically on the SUSY case, but many
 1001 of the results are generic to any model with LLPs.

1002 Long-lived gluinos or squarks carry color-charge and will thus hadronize into
 1003 color neutral bound states called R-Hadrons. These are composit particles like
 1004 the usual hadrons but with one supersymmetric constituent, for example $\tilde{g}q\bar{q}$
 1005 and $\tilde{q}\bar{q}$. Through this hadronization process, the neutral gluino can acquire a
 1006 charge. Gluino pair production, $pp \rightarrow \tilde{g}\tilde{g}$ has the largest cross sectional increase
 1007 with the increase in energy to 13 TeV, and so this search focuses on gluino R-
 1008 Hadrons. Planned future updates will extend the case to explicitly include squark
 1009 and chargino models, but the method covers any long-lived, charged, massive
 1010 particle.

1011 10.1 EVENT TOPOLOGY

1012 The majority of SUSY models predict that gluinos will be produced in pairs at
 1013 the LHC, through processes like $pp \rightarrow q\bar{q} \rightarrow \tilde{g}\tilde{g}$ and $pp \rightarrow gg \rightarrow \tilde{g}\tilde{g}$, where the
 1014 gluon mode dominates for the collision energy and gluino masses considered
 1015 for this search. During their production, the long-lived gluinos hadronize into
 1016 color singlet bound states including $\tilde{g}q\bar{q}$, $\tilde{g}qqq$, and even $\tilde{g}g$ [47]. The probability
 1017 to form the gluon-only bound states is a free parameter usually taken to be 0.1,
 1018 while the meson states are favored among the R-Hadrons [48]. The charged and
 1019 neutral states are approximately equally likely for mesons, so the R-Hadrons will
 1020 be charged roughly 50% of the time.

1021 These channels produce R-Hadrons with large p_T , comparable to their mass,
 1022 so that they typically propagate with $0.2 < \beta < 0.9$ [48]. The fragmentation that
 1023 produces that hadrons is very hard, so the jet structure around the R-Hadron
 1024 is minimal, with less than 5 GeV of summed particle momentum expected in a
 1025 cone of $\Delta R < 0.25$ around the R-Hadron [48]. After hadronization, depending
 1026 on the gluino lifetime, the R-Hadrons then decay into hadrons and a LSP [47].

1027 In summary, the expected event for pair-produced long-lived gluinos is very
 1028 simple: two isolated, high-momentum R-Hadrons that propagate through the
 1029 detector before decaying into jets. The observable features of such events depend

1030 strongly on the interaction of the R-Hadron with the material of the detector and
 1031 also its lifetime. Section 10.1.1 describes the interactions of R-Hadrons which
 1032 reach the various detector elements in A Toroidal LHC ApparatuS ([ATLAS](#)) and
 1033 Section 10.1.2 provides a summary of the observable event descriptions for R-
 1034 Hadrons of various lifetimes.

1035 10.1.1 DETECTOR INTERACTIONS

1036 After approximately 0.2 ns, the R-Hadron reaches the pixel detector. If charged,
 1037 it deposits energy into the material through repeated single collisions that result
 1038 in ionization of the silicon substrate [49]. Because of its comparatively low β ,
 1039 the ionization energy can be significantly greater than expected for [SM](#) particles
 1040 because the most-probable energy loss grows significantly as β decreases [49].
 1041 This large ionization can be measured through the time over threshold ([ToT](#)) read
 1042 out from the pixel detector as described in Section 7.1.1.2. Large ionization in
 1043 the inner detector is one of the major characteristic features of [LLPs](#).

1044 Throughout the next few nanoseconds, the R-Hadron propagates through the
 1045 remainder of the inner detector. A charged R-Hadron will provide hits in each
 1046 of these systems as would any other charged particle, and can be reconstructed
 1047 as a track. The track reconstruction provides a measurement of its trajectory
 1048 and thus its momentum as described in Section 7.1. The large momentum is
 1049 another characteristic feature of massive particles produced at the [LHC](#). **Note: At**
 1050 **this point I am failing to mention that the TRT provides a possible dE/dx**
 1051 **measurement, because no one uses it as far as I know.**

1052 As of roughly 20 ns, the R-Hadron enters the calorimeter where it interacts
 1053 hadronically with the material. Because of its large mass and momentum, the
 1054 R-Hadron does not typically stop in the calorimeter, but rather deposits a small
 1055 fraction of its energy through repeated interactions with nucleons. The proba-
 1056 bility of interaction between the gluino itself and a nucleon is low because the
 1057 cross section drops off with the inverse square of its mass, so the interactions are
 1058 primarily governed by the light constituents [50]. Each of these interactions can
 1059 potentially change that quark content and thus change the sign of the R-Hadron,
 1060 so that the charge at exit is typically uncorrelated with the charge at entry [48].
 1061 The total energy deposited in the calorimeters during the propagation is small
 1062 compared to the kinetic energy of the R-Hadron, around 20-40 GeV, so that
 1063 E/p is typically less than 0.1 [48].

1064 Then, 30 ns after the collision, it reaches the muon system, where it again
 1065 ionizes in the material if charged and can be reconstructed as a muon track. Be-
 1066 cause of the charge-flipping interactions in the calorimeter, this track may have
 1067 the opposite sign of the track reconstructed in the inner detector, or there may
 1068 be a track present when there was none in the inner detector and vice-versa. The
 1069 propagation time at the typically lower β results in a significant delay compared
 1070 to muons, and that delay can be assessed in terms of a time-of-flight measure-
 1071 ment. Because of the probability of charge-flip and late arrival, there is a signif-
 1072 icant chance that an R-Hadron which was produced with a charge will not be

1073 identified as a muon. The long time-of-flight is another characteristic feature of
 1074 R-Hadrons which are reconstructed as muons.

1075 10.1.2 LIFETIME DEPENDENCE

1076 The above description assumed a lifetime long enough for the R-Hadron to exit
 1077 the detector, which through this search is referred to as “stable”, even though
 1078 the particle may decay after exiting the detector. There are several unique sig-
 1079 natures at shorter lifetimes where the R-Hadron decays in various parts of the
 1080 inner detector; these lifetimes are referred to as “metastable”.

1081 The shortest case where the R-Hadron is considered metastable is for life-
 1082 times around 0.01 ns, where the particle decays before reaching any of the de-
 1083 tector elements. Although the R-Hadrons are produced opposite each other in
 1084 the transverse plane, each R-Hadron decays to a jet and an [LSP](#). The [LSPs](#) are not
 1085 measured, so the produced jets can be significantly imbalanced in the transverse
 1086 plane which results in large missing energy. That missing energy can be used
 1087 to trigger candidate events, and provides the most efficient trigger option for
 1088 shorter lifetimes. Additionally, the precision of the tracking system allows the
 1089 displaced vertex of the R-Hadron decay to be reconstructed from the charged
 1090 particles in the jet. The distance of that vertex from the interaction point can
 1091 be used to distinguish R-Hadron decays from other processes. Figure 22 shows
 1092 a schematic diagram of an example R-Hadron event with such a lifetime. The
 1093 diagram is not to scale, but instead illustrates the detector interactions in the
 1094 pixel detector, calorimeters, and muon system. It includes a representation of
 1095 the charged R-Hadron and the neutral R-Hadron, as well as the [LSPs](#) and jets
 1096 (shown as charged hadrons) produced in the decay. Neutral hadrons may also
 1097 be produced in the decay but are not depicted. Previous searches on [ATLAS](#) have
 1098 used the displaced vertex to target [LLP](#) decays [51].

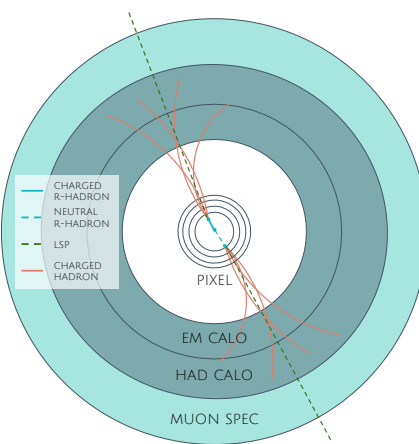


Figure 22: A schematic diagram of an R-Hadron event with a lifetime around 0.01 ns.
 The diagram includes one charged R-Hadron (solid blue), one neutral R-
 Hadron (dashed blue), [LSPs](#) (dashed green) and charged hadrons (solid orange).
 The pixel detector, calorimeters, and muon system are illustrated but not to
 scale.

1099 The next distinguishable case occurs at lifetimes greater than 0.1 ns, where
 1100 the R-Hadron forms a partial track in the inner detector. If the decay products
 1101 are sufficiently soft, they may not be reconstructed, and this forms a unique sig-
 1102 nature of a disappearing track. An example of such an event is illustrated in
 1103 Figure 23, which shows the short track in the inner detector and the undetected
 1104 soft charged hadron and LSP that are produced. A dedicated search on ATLAS used
 1105 the disappearing track signature to search for LLP in Run 1 [52]. **zNote: might**
 1106 **not be worth mentioning the disappearing track here since it is actually a**
 1107 **chargino search, the soft pion is pretty unique to charginos.**

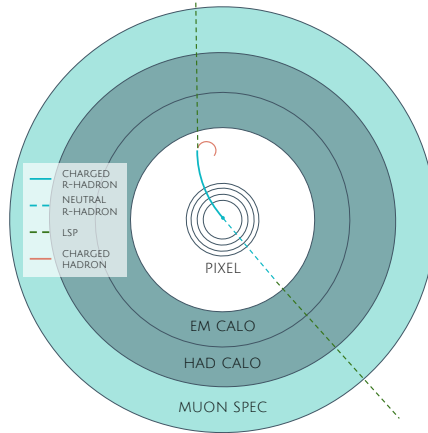


Figure 23: A schematic diagram of an R-Hadron event with a lifetime around 4 ns. The diagram includes one charged R-Hadron (solid blue), one neutral R-Hadron (dashed blue), LSPs (dashed green) and a charged hadron (solid orange). The pixel detector, calorimeters, and muon system are illustrated but not to scale.

1108 If the decay products are not soft, the R-Hadron daughters form jets, resulting
 1109 in an event-level signature of up to two high-momentum tracks, jets, and signif-
 1110 icant missing energy. The missing energy has the same origin as in the case of
 1111 0.01 ns lifetimes, from the decay to unmeasured particles, and again can be large.
 1112 The high-momentum tracks will also have the characteristically high-ionization
 1113 of massive, long-lived particles in the inner detector. Figure 24 illustrates an ex-
 1114 ample event with one charged R-Hadron which decays after approximately 10 ns,
 1115 and shows how the jets from the decay can still be reconstructed in the calorime-
 1116 ter. Several previous searches on ATLAS from Run 1 have used this signature to
 1117 search for R-Hadrons [53, 54], including a dedicated search for metastable parti-
 1118 cles [55].

1119 If the lifetime is longer than several nanoseconds, in the range of 15-30 ns,
 1120 the R-Hadron decay can occur in or after the calorimeters, but prior to reaching
 1121 the muon system. This case is similar to the above, although the jets may not be
 1122 reconstructed, and is covered by many of the same search strategies. The events
 1123 still often have large missing energy, although it is generated through different
 1124 mechanisms. The R-Hadrons do not deposit much energy in the calorimeters, so
 1125 a neutral R-Hadron will not enter into the missing energy calculation. A charged
 1126 R-Hadron opposite a neutral R-Hadron will thus generate significant missing en-
 1127 ergy, and close to 50% of pair-produced R-Hadron events fall into this category.

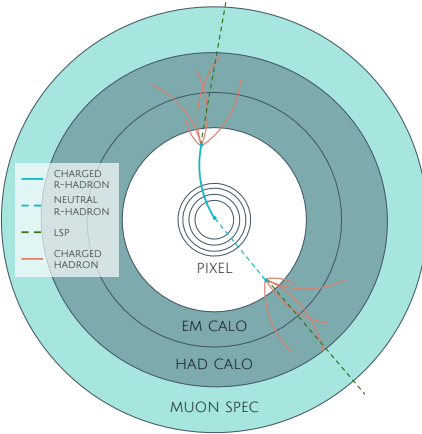


Figure 24: A schematic diagram of an R-Hadron event with a lifetime around 5 ns. The diagram includes one charged R-Hadron (solid blue), one neutral R-Hadron (dashed blue), LSPs (dashed green) and charged hadrons (solid orange). The pixel detector, calorimeters, and muon system are illustrated but not to scale.

1128 If both R-Hadrons are neutral then the missing energy will be low because nei-
 1129 ther is detected. Two charged R-Hadrons will also result in low missing energy
 1130 because both are reconstructed as tracks and will balance each other in the trans-
 1131 verse plane. A small fraction of the time, one of the charged R-Hadron tracks may
 1132 fail quality requirements and thus be excluded from the missing energy calcula-
 1133 tion and again result in significant missing energy. Figure 25 illustrates another
 1134 example event with one charged R-Hadron which decays after approximately 20
 1135 ns, and shows how the jets from the decay might not be reconstructed.

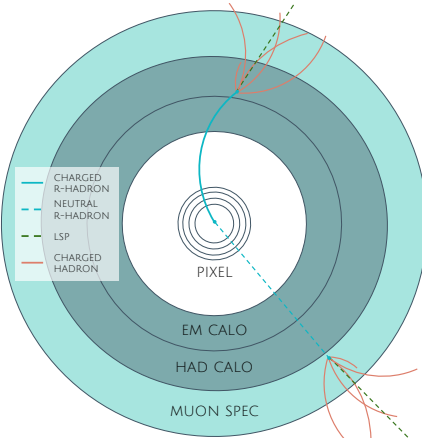


Figure 25: A schematic diagram of an R-Hadron event with a lifetime around 20 ns. The diagram includes one charged R-Hadron (solid blue), one neutral R-Hadron (dashed blue), LSPs (dashed green) and charged hadrons (solid orange). The pixel detector, calorimeters, and muon system are illustrated but not to scale.

1136 The longest lifetimes, the stable case, has all of the features of the 30-50 ns case
 1137 but with the addition of muon tracks for any R-Hadrons that exit the calorimeter
 1138 with a charge. That muon track can provide additional information from time-
 1139 of-flight measurements to help identify LLPs. An example of the event topology

1140 for one charged and one neutral stable R-Hadron is shown in Figure 26. Some
 1141 searches on [ATLAS](#) have included this information to improve the search reach
 1142 for stable particles [54, 56].

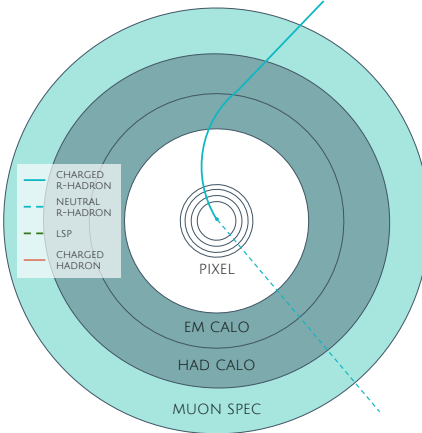


Figure 26: A schematic diagram of an R-Hadron event with a lifetime around 20 ns.
 The diagram includes one charged R-Hadron (solid blue) and one neutral R-Hadron (dashed blue). The pixel detector, calorimeters, and muon system are illustrated but not to scale.

1143 10.2 SIMULATION

1144 All of the event topologies discussed above are explored by simulations of R-
 1145 Hadron events in the [ATLAS](#) detector. A large number of such samples are gen-
 1146 erated to determine signal efficiencies, to measure expected yields, and to esti-
 1147 mate uncertainties. The primary interaction, pair production of gluinos with
 1148 masses between 400 and 3000 GeV, is simulated using [Pythia 6.4.27](#) [57]
 1149 with the AUET2B [58] set of tuned parameters for the underlying event and
 1150 the CTEQ6L1 [31] parton distribution function ([PDF](#)) set. The simulated inter-
 1151 actions include a modeling of pileup by adding secondary, minimum bias in-
 1152 teractions from both the same (in-time pileup) and nearby (out-of-time pileup)
 1153 bunch crossings. This event generation is then augmented with a dedicated
 1154 hadronization routine to hadronize the long-lived gluinos into final states with
 1155 R-Hadrons [59], with the probability to form a gluon-gluino bound set at 10% [60].

1156 The cross sections used for these processes are calculated at next-to-leading
 1157 order ([NLO](#)) in the strong coupling constant with a resummation of soft-gluon
 1158 emmission at next-to-leading logarithmic ([NLL](#)) [61–65]. The nominal predic-
 1159 tions and the uncertainties for each mass point are taken from an envelope of
 1160 cross-section predictions using different [PDF](#) sets and factorization and renor-
 1161 malization scales [66].

1162 The R-Hadrons then undergo a full detector simulation [], where the interac-
 1163 tions of the R-Hadrons with the material of the detector are described by dedi-
 1164 cated [Geant4](#) [1] routines. These routines model the interactions described in
 1165 Section 10.1.1, including the ionizing interactions in the silicon modules of the
 1166 inner detector and the R-Hadron-nucleon interactions in the calorimeters [67],

1167 [68]. The specific routine chosen to describe the interactions of the R-Hadrons
 1168 with nucleons, the “generic model”, uses a pragmatic approach where the scatter-
 1169 ing cross section is taken to be a constant 12 mb per light quark. In this model
 1170 the gluino itself does not interact at all except through its role as a reservoir of
 1171 kinetic energy.

1172 The lifetimes of these R-Hadrons are then simulated at several working points,
 1173 $\tau = 0.1, 1.0, 3.0, 10, 30, 50$ and detector stable, where the particle is required to
 1174 decay after propagating for a time compatible with its lifetime. Only one decay
 1175 mode is simulated for these samples, $\tilde{g} \rightarrow q\bar{q}\tilde{\chi}_1^0$ with the neutralino mass set to
 1176 100 GeV, which is chosen because it has the highest sensitivity among all of the
 1177 modes studied in previous searches [55]. Heavier neutralinos have similar results
 1178 but generate less missing energy which reduces the efficiency of triggering.

1179 All of the simulated events are then reconstructed using the same software
 1180 used for collision data. The fully reconstructed events are then reweighted to
 1181 match the distribution of initial state radiation in an alternative sample of events,
 1182 generated with MG5_aMC@NLO [69], which has a more accurate description of ra-
 1183 diate effects than Pythia6. This reweighting provides a more accurate descrip-
 1184 tion of the momentum of the gluino-gluino system and is important in modeling
 1185 the efficiency of triggering and offline event selection.

1186

1187 EVENT SELECTION

1188 The [LLPs](#) targeted by this search differ in their interactions with the detector from
 1189 [SM](#) particles primarily because of their large mass. When produced at the ener-
 1190 gies available at the [LHC](#), that large mass results in a low β (typically $0.2 < \beta <$
 1191 0.9). Such slow-moving particles heavily ionize in detector material. Each layer
 1192 of the pixel detector provides a measurement of that ionization, through [ToT](#), as
 1193 discussed in Section 6.3.1. The ionization in the pixel detector, quantified in
 1194 terms of dE/dx , provides the major focus for this search technique, along with
 1195 the momentum measured in the entire inner detector. It is effective both for its
 1196 discriminating power and its use in reconstructing a particle's mass, and it can
 1197 be used for a wide range of masses and lifetimes as discussed in Section 10.1.2.
 1198 However dE/dx needs to be augmented with a few additional selection require-
 1199 ments to provide a mechanism for triggering and to further reduce backgrounds.

1200 Ionization itself is not currently accessible for triggering, so this search in-
 1201 stead relies on E_T^{miss} to trigger signal events. Although triggering on E_T^{miss} can
 1202 be inefficient, E_T^{miss} is often large for many production mechanisms of [LLPs](#), as
 1203 discussed in Section 10.1.

1204 The use of ionization to reject [SM](#) backgrounds relies on well-measured, high-
 1205 momentum tracks, so some basic requirements on quality and kinematics are
 1206 placed on the tracks considered in this search. These quality requirements have
 1207 been significantly enhanced in Run 2 by a newly introduced tracking variable
 1208 that is very effective in removing highly-ionizing backgrounds caused by over-
 1209 lapping tracks. A few additional requirements are placed on the tracks consid-
 1210 ered for [LLP](#) candidates that increase background rejection by targeting specific
 1211 types of [SM](#) particles. These techniques provide a significant analysis improve-
 1212 ment over previous iterations of ionization-based searches on ATLAS by provid-
 1213 ing additional background rejection with minimal loss in signal efficiency.

1214 The ionization measurement with the Pixel detector can be calibrated to pro-
 1215 vide an estimator of $\beta\gamma$. That estimate, together with the momentum measure-
 1216 ment provided by tracking, can be used to reconstruct a mass for each track
 1217 which traverses the pixel detector. That mass variable will be peaked at the [LLP](#)
 1218 mass for any signal, and provides an additional tool to search for an excess. In
 1219 addition to an explicit requirement on ionization, this search constructs a mass-
 1220 window for each targeted signal mass in order to evaluate any excess of events
 1221 and to set limits.

1222 The strategy discussed here is optimized for lifetimes of $O(1) - O(10)$ ns.
 1223 Pixel ionization is especially useful in this regime as particles only need to prop-
 1224 agate through the first seven layers of the inner detector, about 37 cm from the
 1225 beam axis. The search is still competitive with other searches for [LLPs](#) at longer
 1226 lifetimes, because the primary discriminating variables are still applicable even
 1227 for particles that do not decay within the detector [56]. Although the majority of

1228 the requirements will be the same for all lifetimes, two signal regions are defined
 1229 to optimize separately for intermediate and long lifetime particles.

1230 11.1 TRIGGER

1231 Triggering remains a significant difficulty in defining an event selection with
 1232 high signal efficiency in a search for LLPs. There are no triggers available in
 1233 the current ATLAS system that can fire directly from a high momentum track
 1234 with large ionization (Section 6.6). Although in some configurations a charged
 1235 LLP can fire muon triggers, this requirement introduces significant model depen-
 1236 dence on both the allowed lifetimes and the interactions in the calorimeter [48],
 1237 as discussed in Section 10.1.1.

1238 For a search targeting particles which may decay prior to reaching the muon
 1239 system, the most efficient available trigger is based on missing energy [48]. As
 1240 discussed in Section 10.1, signal events can produce significant E_T^{miss} by a few
 1241 mechanisms. At the trigger level however, the missing energy is only calculated
 1242 using the calorimeters (Section 6.6) where the R-Hadrons deposit little energy.
 1243 So, at short lifetimes, E_T^{miss} measured in the calorimeter is generated by an im-
 1244 balance between the jets and undetected LSPs produced in R-Hadron decays. At
 1245 longer lifetimes, without the decay products, missing energy is only produced in
 1246 the calorimeters when the R-Hadrons recoil against an initial state radiation (ISR)
 1247 jet.

1248 These features are highlighted in Figure 27, which shows the E_T^{miss} distribu-
 1249 tions for simulated short lifetime (3 ns) and stable R-Hadron events. The figure
 1250 includes both the offline E_T^{miss} , the missing energy calculated with all available
 1251 information, and Calorimeter E_T^{miss} , the missing energy calculated using only
 1252 information available at the calorimeter which approximates the missing energy
 1253 available at the trigger. The short lifetime sample has significantly greater E_T^{miss}
 1254 and Calorimeter E_T^{miss} than the stable sample as expected. For the stable sam-
 1255 ple, a small fraction of events with very large E_T^{miss} (about 5%) migrate into the
 1256 bin with very small Calorimeter E_T^{miss} because the E_T^{miss} produced by a charged
 1257 R-Hadron track opposite a neutral R-Hadron track does not contribute any miss-
 1258 ing energy in the calorimeters.

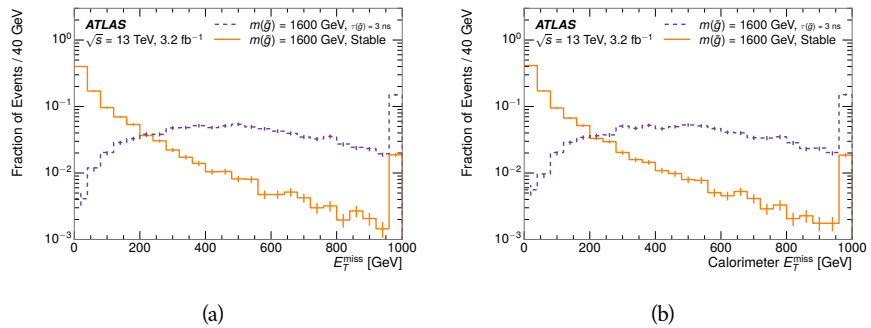


Figure 27: The distribution of (a) E_T^{miss} and (b) Calorimeter E_T^{miss} for simulated signal events before the trigger requirement.

1259 So, either case to some extent relies on kinematic degrees of freedom to pro-
 1260 duce missing energy, as the pair-produced LLPs tend to balance each other in
 1261 the transverse plain. That balance results in a relatively low efficiency for long-
 1262 lifetime particles, roughly 40%, and efficiencies between 65% and 95% for shorter
 1263 lifetimes depending on both the mass and the lifetime. For long lifetimes in par-
 1264 ticular, the presence of ISR is important in providing an imbalance in the trans-
 1265 verse plane, and is an important aspect of modeling the selection efficiency for
 1266 R-Hadron events.

1267 The missing energy trigger with the lowest threshold available is chosen for
 1268 this selection in order to maximize the trigger efficiency. During 2015 data col-
 1269 lection this was the HLT_xe70 trigger, which used a 50 GeV threshold on miss-
 1270 ing energy at LVL1 and a 70 GeV threshold on missing energy at the HLT. These
 1271 formation of the trigger decision for missing energy was discussed in more detail
 1272 in Section 6.6.

1273 11.2 KINEMATICS AND ISOLATION

1274 After the trigger requirement, each event is required to have a primary vertex
 1275 reconstructed from at least two well-measured tracks in the inner detector, each
 1276 with $p_T > 400$ MeV. If more than one such vertex exists, the primary vertex
 1277 is taken to be the one with the largest summed track momentum for all tracks
 1278 associated to that vertex. The offline reconstructed E_T^{miss} is required to be above
 1279 130 GeV to additionally reject SM backgrounds. The transverse missing energy
 1280 is calculated using fully reconstructed and calibrated offline objects, as described
 1281 in Section 7.5. In particular the E_T^{miss} definition in this selection uses jets recon-
 1282 structed with the anti- k_t algorithm with radius $R = 0.4$ from clusters of energy
 1283 in the calorimeter (Section 7.2) and with $p_T > 20$ GeV, as well as reconstructed
 1284 muons, electrons, and tracks not identified as another object type.

1285 The E_T^{miss} distributions are shown for data and a few simulated signals in Fig-
 1286 ure 28, after the trigger requirement. The cut placed at 130 GeV is 95% effi-
 1287 cient for metastable and 90% efficient for stable particles, after the trigger re-
 1288 quirement, because of the missing energy generating mechanisms discussed pre-
 1289 viously. The distribution of data in this figure and subsequent figures in this sec-
 1290 tion can be interpreted as the distribution of backgrounds, as any signal contam-
 1291 ination would be negligible if present at these early stages of the selection (prior
 1292 to the final requirement on ionization). The background falls rapidly with miss-
 1293 ing energy, motivating the direct requirement on E_T^{miss} for the signal region. Al-
 1294 though a tighter requirement than the specified value of 130 GeV would seem to
 1295 increase the search potential from these early distributions, other requirements
 1296 are more optimal when taken as a whole. The specific values for each require-
 1297 ment in signal region were optimized considering the increase in discovery reach
 1298 for tightening the requirement on each discriminating variable. **NOTE: If space**
 1299 **and time permit, I will add a whole section about signal region optimiza-**
 1300 **tion..**

1301 It is typically the practice for searches for new physics on ATLAS to place an
 1302 offline requirement on the triggering variable that is sufficiently tight to guar-

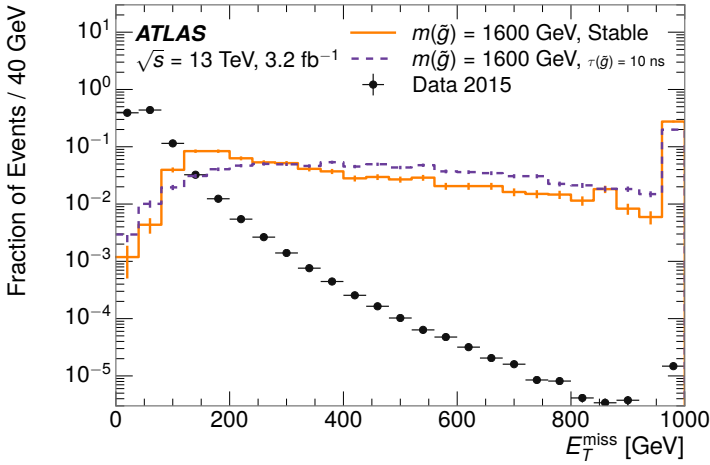


Figure 28: The distribution of E_T^{miss} for data and simulated signal events, after the trigger requirement.

1303 antee that the event would pass the trigger. Such a tight requirement makes the
 1304 uncertainty on the trigger efficiency of the simulation negligible, as modeling the
 1305 regime where the trigger is only partially efficient can be difficult. In this analy-
 1306 sis, however, because of the atypical interactions of R-Hadrons with the tracker
 1307 and the calorimeter, the offline requirement on E_T^{miss} is not sufficient to guar-
 1308 antee a 100% trigger efficiency even at large values, as can be seen in Figure 29.
 1309 This figure shows the efficiency for passing the HLT_xe70 trigger as a function
 1310 of the requirement on E_T^{miss} , which plateaus to roughly 85% even at large values.
 1311 This plateau does not reach 100% because events which have large offline miss-
 1312 ing energy from a neutral R-Hadron produced opposite of a charged R-Hadron
 1313 can have low missing energy in the calorimeters. The Calorimeter E_T^{miss} , on the
 1314 other hand, does not have this effect and reaches 100% efficiency at large values
 1315 because it is the quantity that directly corresponds to the trigger threshold. In
 1316 both cases the efficiency of triggering is greater for the short lifetime sample be-
 1317 cause the late decays to hadrons and LSPs produce an imbalance in the calorime-
 1318 ters even though they may not be reconstructed offline as tracks or jets. For this
 1319 reason, the requirement on E_T^{miss} is determined by optimizing the background
 1320 rejection even though it corresponds to a value of trigger efficiency significantly
 1321 below 1.0.

1322 Potential signal events are then required to have at least one candidate LLP
 1323 track. Although the LLPs are produced in pairs, many models do not consistently
 1324 yield two charged particles. For example, in the R-Hadron model highlighted
 1325 here, only 20% of events have two charged R-Hadrons while 47% of events have
 1326 just one. A signal region requiring two charged candidates could be a powerful
 1327 improvement in background rejection for a larger dataset, but it is not consid-
 1328 ered in this version of the analysis as it was found to be unnecessary to reject the
 1329 majority of backgrounds.

1330 For a track to be selected as a candidate, it must have $p_T > 50 \text{ GeV}$ and pass
 1331 basic quality requirements. The track must be associated to the primary vertex.

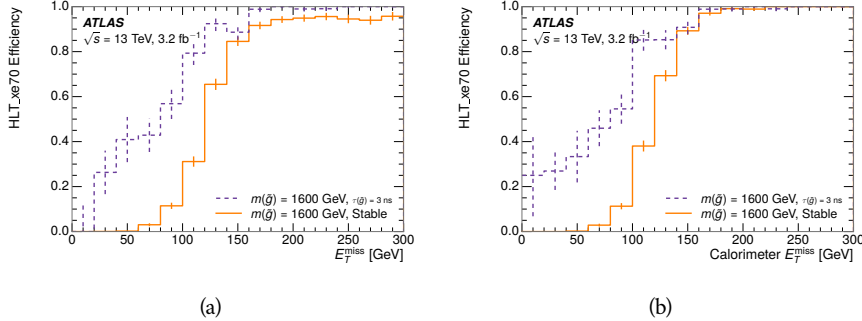


Figure 29: The trigger efficiency for the HLT_xe70 trigger requirement as a function of (a) E_T^{miss} and (b) Calorimeter E_T^{miss} for simulated signal events.

It must also have at least seven clusters in the silicon layers in the inner detector to ensure an accurate measurement of momentum. Those clusters must include one in the innermost layer if the extrapolated track is expected to pass through that layer. And to ensure a reliable measurement of ionization, the track is required to have at least two clusters in the pixel detector that provide a measurement of dE/dx .

At this point in the selection, there is a significant high-ionization background from multiple tracks that significantly overlap in the inner detector. Previous version of this analysis have rejected these overlaps by an explicit overlap rejection between pairs of fully reconstructed tracks, typically by requiring no additional tracks within a cone around the candidate. This technique, however, fails to remove the background from tracks that overlap so precisely that the tracks cannot be separately resolved, which can be produced in very collimated photon conversions or decays of pions.

A new method, added in Run 2, identifies cluster shapes that are likely formed by multiple particles based on a neural network classification algorithm. The number of clusters that are classified this way in the pixel detector for a given track is called N_{split} . As the shape of clusters requires significantly less spatial separation to identify overlaps than it does to reconstruct two fully resolved tracks, this variable is more effective at rejecting backgrounds from overlaps. Figure 30 shows the dependence of ionization on N_{split} ; as N_{split} increases the most probable value of dE/dx grows significantly up to twice the expected value when $N_{\text{split}} = 4$.

This requirement is very successful in reducing the long positive tail of the dE/dx distributions, as can be seen in Figure 31. Comparing the distribution for “baseline tracks”, tracks with only the above requirements on clusters applied and before the requirement on N_{split} , to the distribution with $N_{\text{split}} = 0$, it is clear that the fraction of tracks with large dE/dx is reduced by several orders of magnitude. The tracks without split hits are very close to the dE/dx distribution of identified muons, which are extremely well isolated on average. Figure 31 also includes the distribution of dE/dx in an example signal simulation to demonstrate how effective dE/dx is as a discriminating variable with this isolation applied. The background falls rapidly for $dE/dx > 1.8 \text{ MeVg}^{-1}\text{cm}^2$

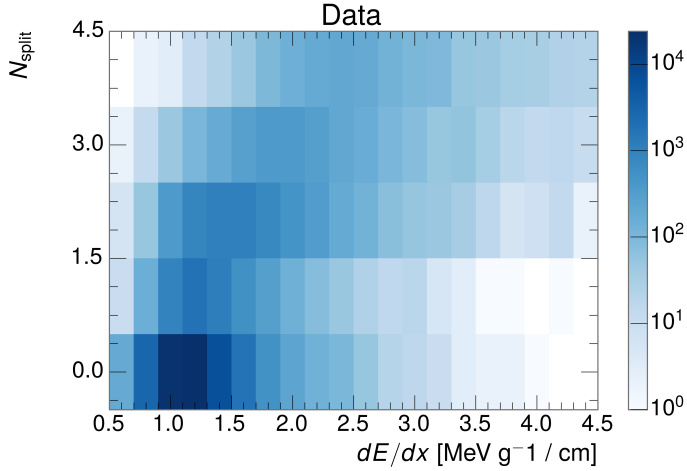


Figure 30: The dependence of dE/dx on N_{split} in data after basic track hit requirements have been applied.

1365 while the majority of the signal, approximately 90% depending on the mass, falls
 1366 above that threshold. Over 90% of LLP tracks in simulated signal events pass the
 1367 N_{split} -based isolation requirement.

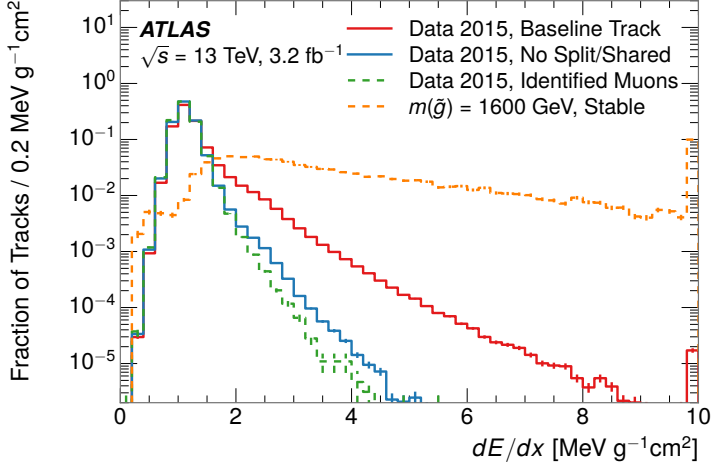


Figure 31: The distribution of dE/dx with various selections applied in data and simulated signal events.

1368 A few additional kinematic requirements are imposed to help reduce SM back-
 1369 grounds. The momentum of the candidate track must be at least 150 GeV, and
 1370 the uncertainty on that measurement must be less than 50%. The distribution of
 1371 momentum is shown in Figure 32 for tracks in data and simulated signal events
 1372 after the previously discussed requirements on clusters, transverse momentum,
 1373 and isolation have been imposed. The signal particles are much harder on aver-

age than their backgrounds because of the high energy interactions required to produce them. The transverse mass, M_T , defined as

$$M_T = \sqrt{2p_T E_T^{\text{miss}}(1 - \cos(\Delta\phi(E_T^{\text{miss}}, \text{track})))} \quad (1)$$

estimates the mass of a decay of to a single charged particle and an undetected particle and is required to be greater than 130 GeV to reject contributions from the decay of W bosons. Figure 33 shows the distribution of M_T for data and simulated signal events. The signal is distributed over a wide range of M_T , with about 90% above the threshold value of 130 GeV. The data shows a dual-peaked structure, where the first peak comes from W boson decays and the second peak is a kinematic shaping from the requirements on E_T^{miss} and the track p_T in dijet events.

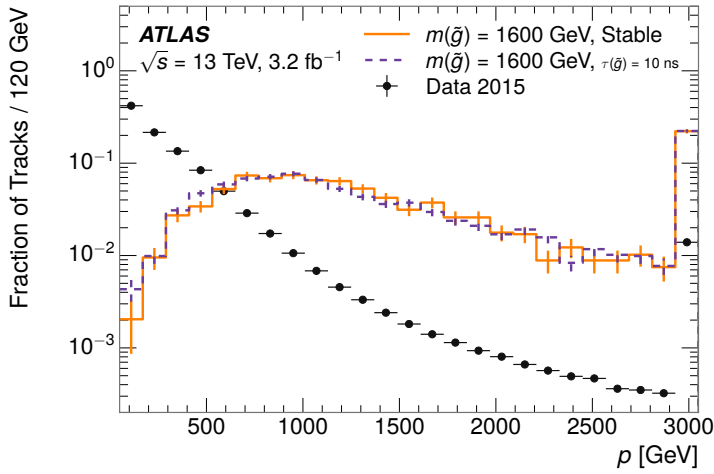


Figure 32: The distribution of track momentum for data and simulated signal events, after previous selection requirements have been applied.

11.3 PARTICLE SPECIES REJECTION

The amount of ionization deposited by particles with low mass and high momentum has a large positive tail [49], so backgrounds can be formed by a wide variety of SM processes when various charged particles have a few randomly large deposits of energy in the pixel detector. Those backgrounds can be additionally reduced by targeting other interactions with the detector where they are expected to have different behavior than R-Hadrons. The interactions with the detector depend on the types of particles produced rather than the processes which produce them, so this search forms a series of rejections to remove backgrounds from individual particle species. These rejections focus on using additional features of the event, other than the kinematics of the candidate track, as they can provide a powerful source of background rejection with very high signal efficiency. However, the lifetime of an R-Hadron can significantly change its

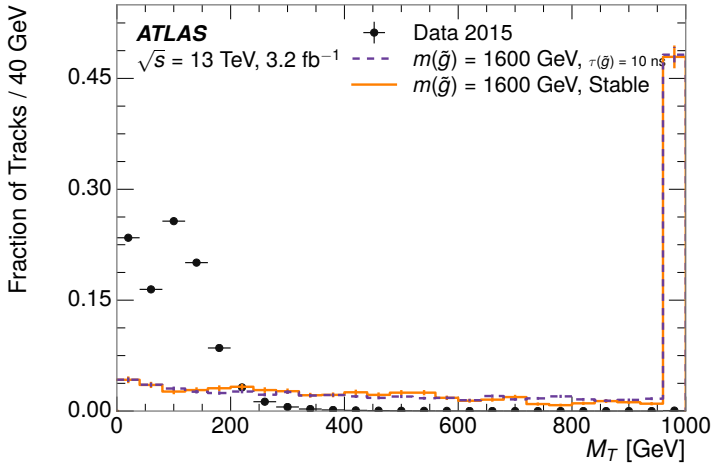


Figure 33: The distribution of M_T for data and simulated signal events, after previous selection requirements have been applied.

1397 detector characteristics, as discussed in Section 10.1.2. To accommodate these
 1398 differences, the SM rejections defined in this section are split to form two signal
 1399 regions, one for long-lifetimes particles, the stable region ($50 \leq \tau[\text{ns}] < \infty$),
 1400 and one for intermediate lifetime particles, the metastable region ($0.4 < \tau[\text{ns}] <$
 1401 50).

1402 Jets can be very effectively rejected by considering the larger-scale isolation of
 1403 the candidate track. In this case the isolation focuses on the production of nearby
 1404 particles as a jet-veto, rather than the isolation from overlapping tracks based on
 1405 N_{split} that was used to reduce high-ionization backgrounds. As explained in Sec-
 1406 tion 10.1, the fragmentation process which produces an R-Hadron is very hard
 1407 and thus is not expected to produce additional particles with a summed momen-
 1408 tum of more than 5 GeV. The jet-veto uses the summed momentum of tracks
 1409 with a cone of $\Delta R < 0.25$, referred to as p_T^{Cone} , which is shown in Figure 34 for
 1410 data and simulated signal events. In the data this value has a peak at zero from
 1411 isolated tracks such as leptons, and a long tail from jets which contains as much
 1412 as 80% of the background above 20 GeV at this stage of the selection. In signal
 1413 events p_T^{Cone} is strongly peaked at zero and significantly less than 1% of signal
 1414 events have p_T^{Cone} above 20 GeV. This makes a requirement of $p_T^{\text{Cone}} < 20$ GeV
 1415 a very effective method to reject background without losing signal efficiency.
 1416 For the stable signal region, this cut is further tightened to $p_T^{\text{Cone}} < 5$ GeV as
 1417 it is the most effective variable remaining to extend the search reach for long
 1418 lifetimes.

1419 Even for fully isolated particles, there are additional methods to reject each
 1420 type of particle using information in the muon system and calorimeters. Muons
 1421 can be identified very reliably using the tracks in the muon system, as described
 1422 in Section 7.4. For intermediate lifetimes the LLPs do not survive long enough
 1423 to reach the muon system, and so muons are vetoed by rejecting tracks that as-
 1424 sociate to a muon with medium muon identification requirements (Section 7.4).
 1425 For longer lifetimes, this rejection is not applied because LLPs which reach the

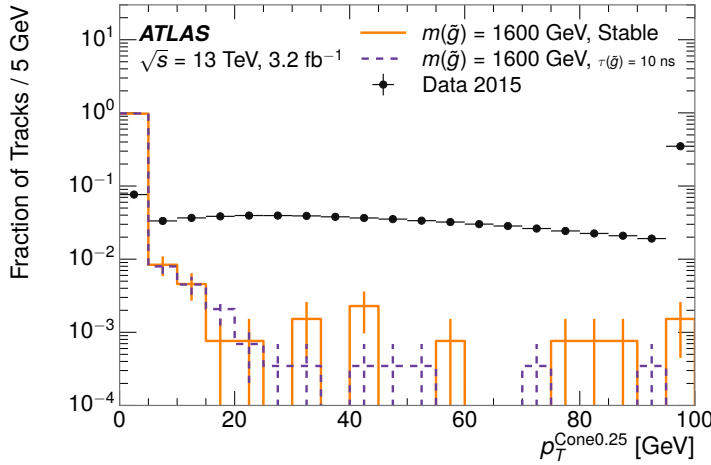


Figure 34: The distribution of summed tracked momentum within a cone of $\Delta R < 0.25$ around the candidate track for data and simulated signal events, after previous selection requirements have been applied.

muon system can be identified as muons as often as 30% of the time in simulated samples.

Calorimeter-based particle rejection relies on the expected small deposits of energy from LLPs. When the lifetime is long enough to reach the calorimeter, a LLP deposits little of its energy as it traverses the material, as discussed in Section 10.1. Even when the particle does decay before the calorimeter, the majority of its energy is carried away by the LSP and not deposited in the calorimeter. In both cases the energy is expected to be distributed across the layers of the calorimeters and not peaked in just one layer. This can be quantified in terms of E/p , the ratio of calorimeter energy of a nearby jet to the track momentum, and f_{EM} , the fraction of energy in that jet within the electromagnetic calorimeter. When no jets fall within a cone of 0.05 of the particle, E/p and f_{EM} are both defined as zero. E/p is expected to be above 1.0 for typical SM particles because of calibration and the contributions from other nearby particles, as discussed in Chapter ???. At these momenta there is no significant zero fraction due to interactions with the detector or insufficient energy deposits (see Section 8.2.2). f_{EM} is peaked close to 1.0 for electrons, and distributed between 10% and 90% for hadrons.

These trends can be seen in the two dimensional distribution for signal in Figure 35 for stable and metastable (10 ns) events. The majority of R-Hadrons in both samples fall into the bin for $E/p = 0$ and $f_{\text{EM}} = 0$ because the majority of the time there is no associated jet. In the stable sample, when there often is an associated jet, E/p is typically still below 0.1, and the f_{EM} is predominantly under 0.8. In the metastable sample, on the other hand, E/p is larger but still typically below 0.1 because of actual jets produced during the decay. The f_{EM} is much lower on average in this case, below 0.1, because the 10 ns lifetime particles rarely decay before passing through the electromagnetic calorimeter. Figure 35 also includes simulated Z decays to electrons or tau leptons. From the decays

1454 to electrons it is clear that the majority of electrons have f_{EM} above 0.9. The
 1455 tau decays include a variety of products. Muons can be seen in the bin where
 1456 $E/p = 0$ and $f_{\text{EM}} = 0$ because they do not have an associated jet. Electrons fall
 1457 into the range where $E/p > 1$ and $f_{\text{EM}} > 0.9$. Hadronic tau decays are the most
 1458 common, and fall in the range of $0.1 < f_{\text{EM}} < 0.9$ and $E/p > 1.0$.

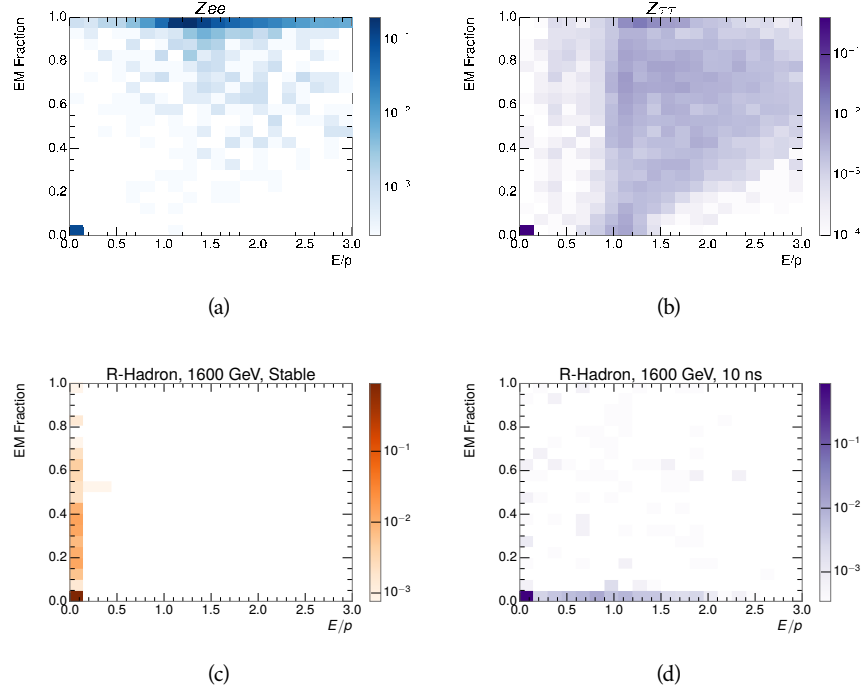


Figure 35: The normalized, two-dimensional distribution of E/p and f_{EM} for simulated
 (a) $Z \rightarrow ee$, (b) $Z \rightarrow \tau\tau$, (c) 1200 GeV Stable R-Hadron events, and (d) 1200
 GeV, 10 ns R-Hadron events.

1459 These differences motivate an electron rejection by requiring an f_{EM} below
 1460 0.9. Similarly, isolated hadrons are rejected by requiring $E/p < 1.0$. These re-
 1461 quirements combine to remove the majority of isolated electrons and hadrons
 1462 but retain over 95% of the simulated signal across a range of masses and lifetimes.

1463 11.4 IONIZATION

1464 The final requirement on the candidate track is the primary discriminating vari-
 1465 able, the ionization in the pixel detector. That ionization is measured in terms
 1466 of dE/dx , which was shown for data and simulated signal events in Figure 31.
 1467 dE/dx is dramatically greater for the high mass signal particles than the back-
 1468 grounds, which start to fall immediately after the minimally ionizing peak at 1.1
 1469 $\text{MeV g}^{-1} \text{cm}^2$. The dE/dx for candidate tracks must be greater than a pseudorapidity-
 1470 dependent threshold, specifically $1.80 - 0.11|\eta| + 0.17\eta^2 - 0.05\eta^3 \text{ MeV g}^{-1} \text{ cm}^{-2}$,
 1471 in order to correct for an approximately 5% dependence of the MIP peak on η .
 1472 The requirement was chosen as part of the signal region optimization, and man-

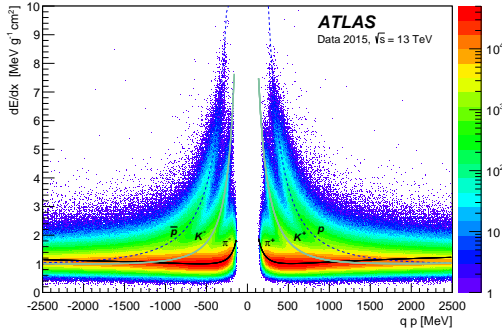


Figure 36: Two-dimensional distribution of dE/dx versus charge signed momentum (qp) for minimum-bias tracks. The fitted distributions of the most probable values for pions, kaons and protons are superimposed.

ages to reduce the backgrounds by a factor of 100 while remaining 70-90% efficient for simulated signal events depending on the mass.

11.4.1 MASS ESTIMATION

The mean value of ionization in silicon is governed by the Bethe equation and the most probable value follows a Landau-Vavilov distribution [49]. Those forms inspire a parametric description of dE/dx in terms of $\beta\gamma$,

$$(dE/dx)_{MPV}(\beta\gamma) = \frac{p_1}{\beta^{p_3}} \ln(1 + [p_2 \beta\gamma]^{p_5}) - p_4 \quad (2)$$

which performs well in the range $0.3 < \beta\gamma < 1.5$. This range includes the expected range of $\beta\gamma$ for the particles targeted for this search, with $\beta\gamma \approx 2.0$ for lower mass particles ($O(100 \text{ GeV})$) and up to $\beta\gamma \approx 0.5$ for higher mass particles ($O(1000 \text{ GeV})$). The parameters, p_i , are fit using a 2015 data sample of low-momentum pions, kaons, and protons as described in Ref. [70]. Figure 36 shows the two-dimensional distribution of dE/dx and momentum along with the above fitted values for $(dE/dx)_{MPV}$.

The above equation (2) is then numerically inverted to estimate $\beta\gamma$ and the mass for each candidate track. In simulated signal events, the mean of this mass value reproduces the generated mass up to around 1800 GeV to within 3%, and 3% shift is applied to correct for this difference. The mass distributions prior to this correction are shown for a few stable mass points in Figure 37. The large widths of these distributions come from the high variability in energy deposits in the pixel detector as well as the uncertainty on momentum measurements at high momentum, but the means converge to the expected values.

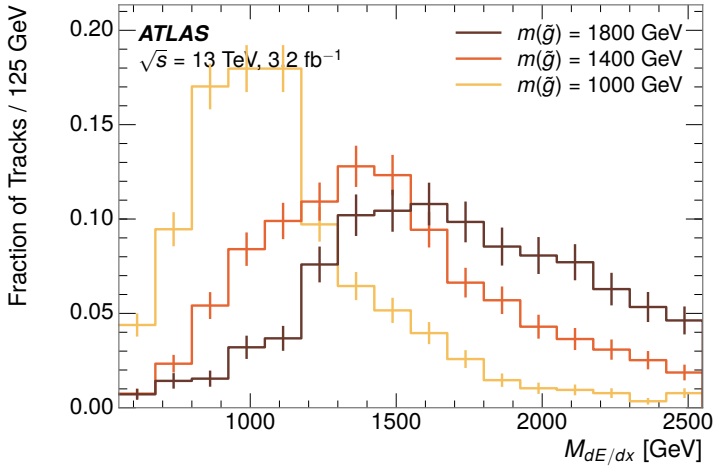


Figure 37: The distribution of mass estimated using dE/dx for simulated stable R-Hadrons with masses between 1000 and 1600 GeV.

1494 This analysis evaluates expected yields and the resulting cross sectional limits
 1495 using windows in this mass variable. The windows are formed by fitting mass
 1496 distributions in simulated signal events like those in Figure 37 to Gaussian distri-
 1497 butions and taking all events that fall within $\pm 1.4\sigma$ of the mean. As can be seen
 1498 in Figure 37, typical values for this width are $\sigma \approx 300 - 500$ GeV depending on
 1499 the generated mass.

1500 11.5 EFFICIENCY

1501 The numbers of events passing each requirement through ionization are shown
 1502 in Table 2 for the full 2015 dataset and a simulated 1600 GeV, 10 ns lifetime R-
 1503 Hadron sample. The table highlights the overall acceptance \times efficiency for sig-
 1504 nal events, which for this example is 19%. Between SM rejection and ionization,
 1505 this signal region reduces the background of tracks which pass the kinematic
 1506 requirements down by an additional factor of almost 2000.

1507 There is a strong dependence of this efficiency on lifetime and mass, with effi-
 1508 ciencies dropping to under 1% at low lifetimes. Figure 38 shows the dependence
 1509 on both mass and lifetime for all signal samples considered in this search. The
 1510 dependence on mass is relatively slight and comes predominantly from the in-
 1511 creasing fraction of R-Hadrons which pass the ionization cut with increasing
 1512 mass. The trigger and E_T^{miss} requirements are most efficient for particles that
 1513 decay before reaching the calorimeters. However, the chance of a particle to be
 1514 reconstructed as a high-quality track decreases significantly at low lifetimes as
 1515 the particle does not propagate sufficiently through the inner detector. These
 1516 effects lead to a maximum in the selection efficiency for lifetimes around 10-30
 1517 ns.

1518 The inefficiency of this signal region at short lifetimes comes almost exclu-
 1519 sively from an acceptance effect, in that the particles do not reach the necessary

Selection	Exp. Signal Events	Observed Events in 3.2 fb^{-1}
Generated	26.0 ± 0.3	
E_T^{miss} Trigger	24.8 ± 0.3 (95%)	
$E_T^{\text{miss}} > 130 \text{ GeV}$	23.9 ± 0.3 (92%)	
Track Quality and $p_T > 50$	10.7 ± 0.2 (41%)	368324
Isolation Requirement	9.0 ± 0.2 (35%)	108079
Track $p > 150 \text{ GeV}$	6.6 ± 0.2 (25%)	47463
$M_T > 130 \text{ GeV}$	5.8 ± 0.2 (22%)	18746
Electron and Hadron Veto	5.5 ± 0.2 (21%)	3612
Muon Veto	5.5 ± 0.2 (21%)	1668
Ionization Requirement	5.0 ± 0.1 (19%)	11

Table 2: The expected number of events at each level of the selection for metastable $1600 \text{ GeV}, 10 \text{ ns}$ R-Hadrons, along with the number of events observed in data, for 3.2 fb^{-1} . The simulated yields are shown with statistical uncertainties only. The total efficiency \times acceptance is also shown for the signal.

1520 layers of the SCT. This can be seen more clearly by defining a fiducial region
 1521 which includes events with at least one R-Hadron that is produced with non-
 1522 zero charge, $p_T > 50 \text{ GeV}$, $p > 150 \text{ GeV}$, $|\eta| < 2.5$, and a decay distance greater
 1523 than 37 cm in the transverse plane. At short (1 ns) lifetimes, the acceptance into
 1524 this region is as low as 4%. Once this acceptance is accounted for, the selection
 1525 efficiency ranges from 25% at lifetimes of 1 ns up to 45% at lifetimes of 10 ns.

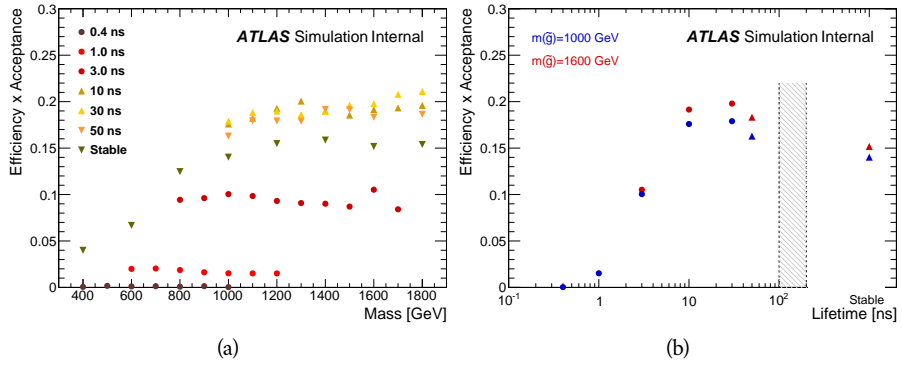


Figure 38: The acceptance \times efficiency as a function of R-Hadron (a) mass and (b) lifetime. (a) shows all of the combinations of mass and lifetime considered in this search, and (b) highlights the lifetime dependence for 1000 GeV and 1600 GeV R-Hadrons.

1526

1527 BACKGROUND ESTIMATION

1528 The event selection discussed in the previous section focuses on detector signa-
 1529 tures, emphasizing a single high-momentum, highly-ionizing track. That track
 1530 is then required to be in some way inconsistent with the expected properties
 1531 of SM particles, with various requirements designed to reject jets, hadrons,
 1532 electrons, and muons (Section 11.3). Therefore the background for this search comes
 1533 entirely from reducible backgrounds that are outliers of various distributions in-
 1534 cluding dE/dx , f_{EM} , and p_T^{Cone} . The simulation can be tuned in various ways to
 1535 do an excellent job of modeling the average properties of each particle type [71],
 1536 but it is not necessarily expected to accurately reproduce outliers. For this rea-
 1537 sons, the background estimation used for this search is estimated entirely using
 1538 data.

1539 12.1 BACKGROUND SOURCES

1540 SM charged particles with lifetimes long enough to form tracks in the inner de-
 1541 tector can be grouped into three major categories based on their detector inter-
 1542 actions: hadrons, electrons, and muons. Every particle that enters into the back-
 1543 ground for this search belongs to one of these types. Relatively pure samples of
 1544 tracks from each of these types can be formed in data by inverting the various
 1545 rejection techniques in Section 11.3. Specifically, muons are selected requiring
 1546 medium muon identification, electrons requiring $E/p > 1.0$ and $f_{EM} > 0.95$,
 1547 and hadrons requiring $E/p > 1.0$ and $f_{EM} < 0.95$.

1548 Figure 39 shows the distributions of momentum and dE/dx for these cate-
 1549 gories in data, after requiring the event level selection as well as the track re-
 1550 quirements on p_T , hits, and N_{split} , as discussed in Section 11.2. Simulated signal
 1551 events are included for reference. These distribution are only illustrative of the
 1552 differences between types, as the rejection requirements could alter their shape.
 1553 This is especially significant for momentum which enters directly into E/p and
 1554 can indirectly affect muon identification. However the various types show clear
 1555 differences in both distributions. The distributions of momentum are not nec-
 1556 cessarily expected to match between the various types because the production
 1557 mechanisms for each type result in different kinematic distributions. dE/dx is
 1558 also different between types because of incomplete isolation; although the re-
 1559 quirement on N_{split} helps to reduce the contribution of nearby particles it does
 1560 not completely remove the effect of overlaps. Muons are better isolated because
 1561 they do not have the additional particle from hadronization present for hadrons
 1562 and they are significantly less likely do interact with the detector and produce
 1563 secondary particles compared to hadrons and electrons. Thus muons have the
 1564 smallest fraction of dE/dx above the threshold of $1.8 \text{ MeVg}^{-1}\text{cm}^2$; hadrons and
 1565 electrons have a larger fraction above this threshold.

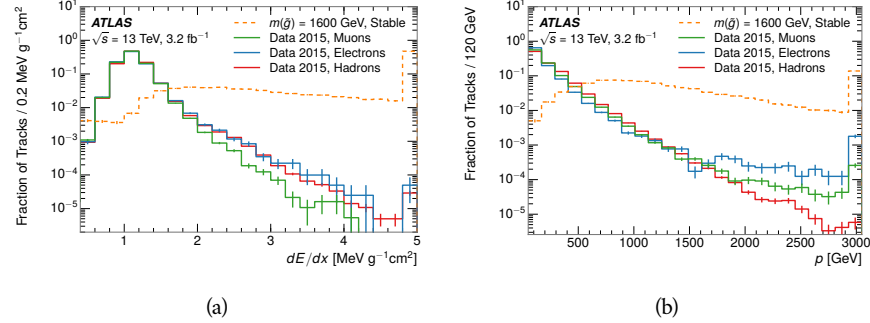


Figure 39: The distribution of (a) dE/dx and (b) momentum for tracks in data and simulated signal after requiring the event level selection and the track selection on p_T , hits, and N_{split} . Each sub-figure shows the normalized distributions for tracks classified as hadrons, electrons, and muons in data and R-Hadrons in the simulated signal.

1566 It is difficult to determine what fraction of each particle type enters into the fi-
 1567 nal signal region. The background method will not have significant dependence
 1568 on the relative contributions of each species, but it is useful to understand the
 1569 differences between each when considering the various tests of the method.

1570 12.2 PREDICTION METHOD

1571 The data-driven background estimation relies on the independence between ion-
 1572 ization and other kinematic variables in the event. For standard model particles
 1573 with momenta above 50 GeV, dE/dx is not correlated with momentum; though
 1574 there is a slight relativistic rise as momentum increases, the effect is small com-
 1575 pared to the width of the distribution of ionization energy deposits.. So, the
 1576 proposed method to estimate the mass distribution of the signal region is to use
 1577 momentum from a track with low dE/dx (below the threshold value) and to com-
 1578 bine it with a random dE/dx value from a dE/dx template. The resulting track is
 1579 just as likely as the original, so a number of such random generations provide the
 1580 expected distributions of momentum and ionization. These are then combined
 1581 using the parametrization described in Section 11.4.1 to form a distribution of
 1582 mass for the signal region.

1583 Algorithmically this method is implemented by forming two distinct Control
 1584 Regions (**CR**s). The first **CR**, CR1, is formed by applying the entire event selec-
 1585 tion from Chapter 11 up to the dE/dx and mass requirements. The dE/dx re-
 1586 quirement is instead inverted for this region. Because of the independence of
 1587 dE/dx , the tracks in this control region have the same kinematic distribution
 1588 as the tracks in the signal region, and are used to measure a two-dimensional
 1589 template of p and η . The second **CR**, CR2, is formed from the event selection
 1590 through the dE/dx requirement, but with an inverted E_T^{miss} requirement. The
 1591 tracks in this control region are expected to have similar dE/dx distributions to
 1592 the signal region before the ionization requirement, and so this region is used to
 1593 measure a two-dimensional template of dE/dx and η .

1594 The contribution of any signal to the control regions is minimized by the in-
 1595 verted selection requirements. Only less than 10% of simulated signal events
 1596 have either dE/dx or E_T^{miss} below the threshold values in the original signal re-
 1597 gion, while the backgrounds are significantly enhanced by inverting those re-
 1598 quirements. The signal contamination is less than 1% in both control regions
 1599 for all of the simulated masses and lifetimes considered in this analysis.

1600 With those measured templates, the shape of the mass estimation is generated
 1601 by first selecting a random (p , η) combination from CR1. This momentum
 1602 value is combined with a dE/dx value taken from the appropriate distribution
 1603 of dE/dx for the selected η from CR2. The use of η in both random samplings
 1604 controls for any correlation between p , dE/dx , and η . Those values are then
 1605 used to calculate a mass in the same way that is done for regular tracks in data,
 1606 see Section 11.4.1. As this procedure includes all dE/dx values, the cut at 1.8
 1607 MeVg $^{-1}$ cm 2 is then enforced to fully model the signal region. The generated
 1608 mass distribution is then normalized by scaling the background estimate to the
 1609 data in the region $M < 160$ GeV, where signals of this type have already been
 1610 excluded [55]. This normalization uses the distributions of mass generated with-
 1611 out the ionization requirement.

1612 The statistical uncertainties on these background distributions are calculated
 1613 by independently fluctuating each bin of the input templates according to their
 1614 Poisson uncertainties. These fluctuations are repeated a large number of times,
 1615 and the uncertainty on the resulting distribution is taken as the root mean square
 1616 (RMS) deviation of the fluctuations from the average. As the procedure uses one
 1617 million random combinations to generate the distributions, The statistical un-
 1618 certainty from the actual random generations is negligible compared to the un-
 1619 certainty from measuring the templates.

1620 12.3 VALIDATION

1621 The validity of the background estimation technique can be evaluated in both
 1622 data and simulation. The underlying assumption that random combinations of
 1623 dE/dx and momentum can predict a mass distribution in an orthogonal region
 1624 can be tested using simulated samples where concerns like multiple particle types
 1625 can be controlled. Using the same technique in another set of signal-depleted
 1626 regions in data then extends this confidence to the more complicated case where
 1627 several particle species are inherently included.

1628 12.3.1 CLOSURE IN SIMULATION

1629 The first test of the procedure is done using a simulated sample of $W \rightarrow \mu\nu$
 1630 decays. These types of events provide the ingredients required to test the back-
 1631 ground estimate, E_T^{miss} and isolated tracks, with high statistics. In this example
 1632 there is no signal, so simulated events in the orthogonal CRs are used to estimate
 1633 the shape of the mass distribution of the simulated events in the signal region. To
 1634 reflect the different topology for W boson decays, the CRs use slightly modified
 1635 definitions. In all CRs, the requirement of $p > 150$ GeV and the SM rejection

1636 requirements are removed. Additionally, for the signal region the requirement
 1637 on E_T^{miss} is relaxed to 30 GeV and the corresponding inverted requirement on
 1638 CR2 is also set at 30 GeV.

1639 With these modified selections, the simulated and randomly generated distri-
 1640 butions of $M_{dE/dx}$ are shown in Figure 40. This figure includes the mass distri-
 1641 butions before and after the requirement on dE/dx , which significantly shapes
 1642 the distributions. In both cases the background estimation technique repro-
 1643 duces the shape of $M_{dE/dx}$ in the signal region. There is a small difference in the pos-
 1644 itive tail of the mass distribution prior to the ionization cut, where the random
 1645 events underestimate the fraction of tracks with mass above 150 GeV by about
 1646 20%. After the ionization requirement, however, this discrepancy is not present
 1647 and the two distributions agree to within statistical uncertainties.

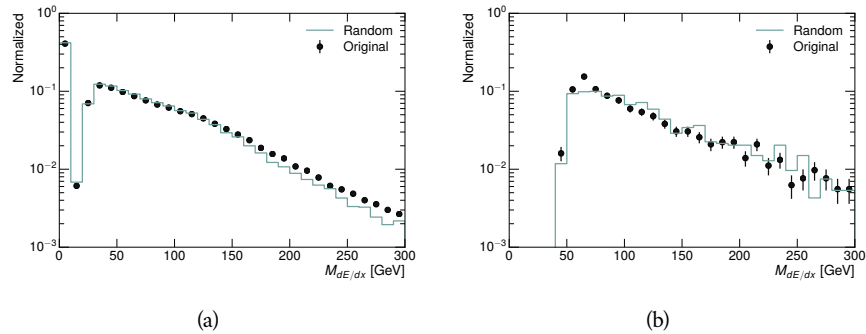


Figure 40: The distribution of $M_{dE/dx}$ (a) before and (b) after the ionization requirement for tracks in simulated W boson decays and for the randomly generated background estimate.

1648 This ability to reproduce the shape of the mass distribution in simulated events
 1649 shows that the technique works as expected. No significant biases are acquired
 1650 in using low dE/dx events to select kinematic templates or in using low E_T^{miss}
 1651 events to select ionization templates, as either would result in a mismodeling of
 1652 the shape of the mass distribution. The simulated events contain only one par-
 1653 ticle type, however, so this test only establishes that the technique works well
 1654 when the the CRs are populated by exactly the same species.

1655 12.3.2 VALIDATION REGION IN DATA

1656 The second test of the background estimate is performed using data in an or-
 1657 thogonal validation region. The validation region, and the corresponding CRs,
 1658 are formed using the same selection requirements as in the nominal method but
 1659 with a modified requirement on momentum, $50 < p[\text{GeV}] < 150$. This allows
 1660 the technique to be checked in a region with very similar properties but where
 1661 the signal is depleted, as the majority of the signal has momentum above 150
 1662 GeV while the backgrounds are enhanced below that threshold. Any biases on
 1663 the particle composition of the CRs for the signal region will be reflected in the
 1664 CRs used to estimate the mass distribution in the validation region.

1665 Figure 41 shows the measured and randomly generated mass distributions for
 1666 data before and after the ionization requirement. The background estimate does
 1667 an excellent job of modeling the actual background before the ionization require-
 1668 ment, with good agreement to within the statistical uncertainties out to the limit
 1669 of the mass distribution. There are very few events in the validation region after
 1670 the ionization requirement, but the few observed events are consistent with the
 1671 background prediction. The good agreement in this validation region provides
 1672 a confirmation that the technique works even in the full-complexity case with
 1673 multiple particle types entering the distributions. Any bias from changes in par-
 1674 ticle composition between regions is small compared to statistical uncertainties.

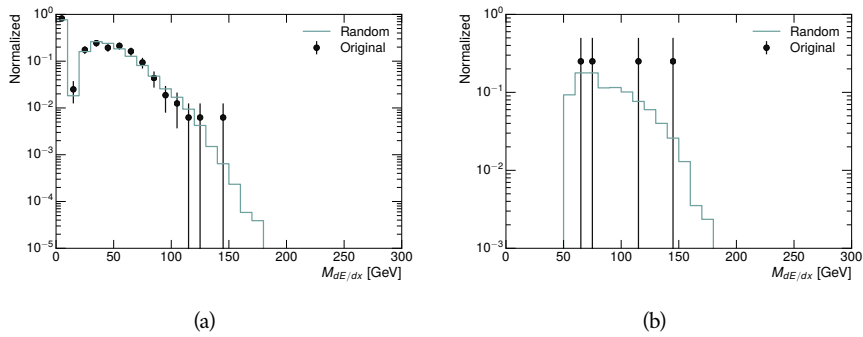


Figure 41: The distribution of $M_{dE/dx}$ (a) before and (b) after the ionization require-
 ment for tracks in the validation region and for the randomly generated back-
 ground estimate.

1675

1676 SYSTEMATIC UNCERTAINTIES AND RESULTS

1677 13.1 SYSTEMATIC UNCERTAINTIES

1678 A number of systematic uncertainties affect the interpretation of the results of
 1679 the search. These uncertainties can broken down into two major categories,
 1680 those which affect the estimate of the background using data and those which
 1681 affect the measurement of the signal yield estimated with simulated events. The
 1682 total measured systematic uncertainties are 7% for the background estimation
 1683 and approximately 32% for the signal yield depending on lifetime. These system-
 1684atic uncertainties are expected to be small compared to the statistical fluctuations
 1685 of the measured yields so that measured cross-sectional limits will be dominated
 1686 by statistical uncertainties. The following sections describe each source of sys-
 1687 tematic uncertainty for each of the two types.

1688 13.1.1 BACKGROUND ESTIMATE

1689 The systematic uncertainties on the background estimate come primarily from
 1690 considering alternative methods for generating the background distributions.
 1691 These uncertainties are small compared to the statistical uncertainties on the
 1692 background estimate which come from the limited statistics in measuring the
 1693 template distributions, as described in Section 12.2. They are summarized in
 1694 Table 3.

Source of Uncertainty:	Value [%]
Analytic Description of dE/dx	4.0
Muon Fraction (Stable Region only)	3.0
IBL Ionization Correction	3.8
Normalization	3.0
Total (Metastable Region):	6.3
Total (Stable Region):	7.0

Table 3: A summary of the sources of systematic uncertainty for the data-driven back-
 ground in the signal region. If the uncertainty depends on the mass, the maxi-
 mum values are reported.

1695 13.1.1.1 ANALYTIC DESCRIPTION OF DE/DX

1696 The background estimate uses a binned template distribution to estimate the
 1697 dE/dx of tracks in the signal region, as described in Section 12.2. It is also possi-

ble to fit that measured distribution to a functional form to help smooth the distribution in the tails of dE/dx where the template is driven by a small number of tracks. Both Landau convolved with a Gaussian and Crystal Ball functions are considered as the functional form and used to re-estimate the background distribution. The deviations compared to the nominal method are found to be 4%, and this is taken as a systematic uncertainty to cover the inability carefully predict the contribution from the long tail of dE/dx where there are few measurements available in data.

1706 13.11.2 MUON FRACTION

1707 The stable region of the analysis explicitly includes tracks identified as muons,
 1708 which have a known difference in their dE/dx distribution from non-muon
 1709 tracks (Section 12.1). To account for a difference in muon fraction between the
 1710 background region and the signal region for this selection, the dE/dx templates
 1711 for muons and non-muons are measured separately and then the relative frac-
 1712 tion of each is varied in the random generation. The muon fraction is varied by
 1713 its statistical uncertainty and the resulting difference of 3% in background yield
 1714 is taken as the systematic uncertainty.

1715 13.11.3 INSERTIBLE B-LAYER (IBL) CORRECTIONS

1716 The acIBL, described in Section 6.3.1, received a significant dose of radiation
 1717 during the data collection in 2015. The irradiation effect the electronics and can
 1718 alter the dE/dx measurement which includes the ToT from the IBL. These effects
 1719 are corrected for in the nominal analysis by scaling the dE/dx measurements
 1720 by a constant factor derived for each run to match the average dE/dx value to
 1721 a reference run where the IBL was known to be stable to this effect. However,
 1722 this corrective factor does not account for inter-run variations. To account for
 1723 this potential drift of dE/dx , the correction procedure is repeated by varying
 1724 the corrections up and down by the maximal run-to-run variation from the full
 1725 data-taking period, which results in an uncertainty of 3.8%.

1726 13.11.4 NORMALIZATION

1727 As described in Section 12.2, the generated distribution of masses is normalized
 1728 in a shoulder region ($M < 160$ GeV) where signals have been excluded by pre-
 1729 vious analyses. That normalization factor is varied by its statistical uncertainty
 1730 and the resulting fluctuation in the mass distribution of 3% is taken as a system-
 1731 atic uncertainty on the background estimate.

1732 13.1.2 SIGNAL YIELD

1733 The systematic uncertainties on the signal yield can be divided into three cate-
 1734 gories; those on the simulation process, those on the modeling of the detector
 1735 efficiency or calibration, and those affecting the overall signal yield. They are
 1736 summarized in Table 3. The largest uncertainty comes from the uncertainty on

1737 the production cross section for gluinos, which is the dominant systematic un-
 1738 certainty in this analysis.

Source of Uncertainty	-[%]	+[%]
ISR Modeling (Metastable Region)	1.5	1.5
ISR Modeling (Stable Region)	14	14
Pile-up Reweighting	1.1	1.1
Trigger Efficiency Reweighting	0.9	0.9
E_T^{miss} Scale	1.1	2.2
Ionization Parametrization	7.1	0
Momentum Parametrization	0.3	0.0
Electron Rejection	0.0	0.0
Hadron Rejection	0.0	0.0
μ Identification	4.3	4.3
Luminosity	5	5
Signal size uncertainty	28	28
Total (Metastable Region)	30	29
Total (Stable Region)	33	32

Table 4: A summary of the sources of systematic uncertainty for the simulated signal yield. The uncertainty depends on the mass and lifetime, and the maximum negative and positive values are reported in the table.

1739 13.1.2.1 ISR MODELING

1740 As discussed in Section 10.2, MadGraph is expected to reproduce the distribution
 1741 of ISR in signal events more accurately than the nominal Pythia samples. The
 1742 analysis reweights the distribution of ISR in the simulated signal events to match
 1743 the distribution found in generated MadGraph samples. This has an effect on the
 1744 selection efficiency in the signal samples, where ISR contributes to the generation
 1745 of E_T^{miss} . To account for the potential inaccuracy on the simulation of ISR at high
 1746 energies, half of the difference between the signal efficiency with the reweighted
 1747 distribution and the original distribution is taken as a systematic uncertainty.

1748 13.1.2.2 PILEUP REWEIGHTING

1749 The simulated events were generated prior to data collection with an estimate
 1750 of the average number of interactions per bunch crossing. This estimate does
 1751 not match the value of pileup during actual data collection, but a large fraction
 1752 of the simulated events would be discarded in order to match the distribution in
 1753 data. Therefore the simulated signal events are not reweighted for pileup by de-
 1754 fault in the analysis. The effect of the pileup on signal efficiency is not expected
 1755 to depend on the mass or lifetime of the generated signal events, which allows

1756 all of the generated signal events to be used together to assess the pileup depen-
 1757 dence. To account for the potential effect of the difference between the number
 1758 of interactions per bunch crossing between data and simulation, the difference
 1759 in yield between the nominal signal events and the reweighted events averaged
 1760 over all masses and lifetimes is taken as a systematic uncertainty on the yield for
 1761 each mass and lifetime (1.1%).

1762 13.1.2.3 TRIGGER EFFICIENCY REWEIGHTING

1763 As described in Section 11.2, the selection for this analysis does not require a suf-
 1764 ficiently large value of E_T^{miss} to be above the plateau of trigger efficiency. There-
 1765 fore, some signal events which would otherwise pass the event selection can be
 1766 excluded because of the trigger requirement. These effects can be difficult to es-
 1767 timate in simulation, and thus are constrained by comparing data and simulated
 1768 events in an alternative W boson region which uses decays to muons to find a rel-
 1769 atively pure sample of events with missing energy. The trigger efficiency for data
 1770 and simulated W events are shown in Figure 42. The comparison between data
 1771 and MC in this region constrains the simulation of the trigger efficiency. The
 1772 simulated signal events are reweighted by the ratio of data to simulation in the
 1773 W boson decays, while the difference between the data and simulation in those
 1774 decays is taken as a systematic uncertainty. This results in an uncertainty of only
 1775 0.9% as the majority of events are well above the plateau and the disagreement
 1776 between data and simulation is small even below that plateau.

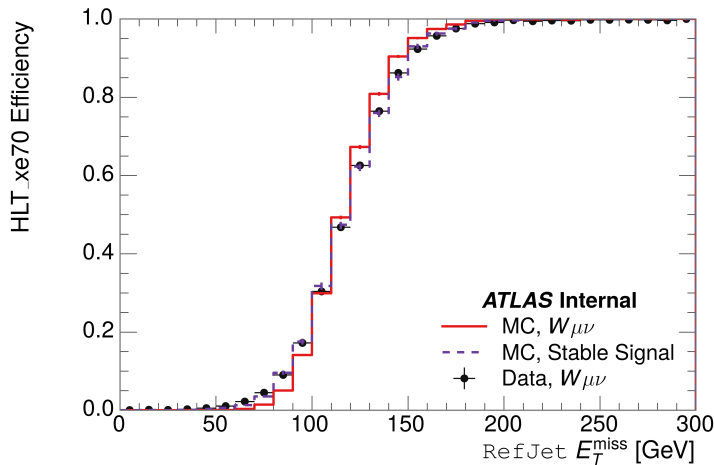


Figure 42: The trigger efficiency for the HLT_xe70 trigger requirement as a function of Calorimeter E_T^{miss} for simulated data events with a W boson selection. Simulated signal events and simulated W boson events are also included.

1777 13.1.2.4 MISSING TRANSVERSE MOMENTUM SCALE

1778 The ATLAS Combined Performance (CP) group provides a default recommenda-
 1779 tion for systematic variations of jets and missing energy (**note: I'm not quite**
 1780 **sure what to cite for this - I don't see any papers from the jet/met group**

Systematic Variation	-[%]	+[%]
JET_GroupedNP_1	-0.7	1.3
JET_GroupedNP_2	-0.7	1.2
JET_GroupedNP_3	-0.5	1.3

Table 5: Example of the contributing systematic variations to the total systematic for the E_T^{miss} Scale, as measured in a 1200 GeV, Stable R-Hadron signal sample.

1781 **after this was implemented).** These variations enter into this analysis only in
 1782 the requirement on E_T^{miss} . The effect of the measured scale of E_T^{miss} is evaluated
 1783 by varying the E_T^{miss} scale according to the one sigma variations provided by all
 1784 **CP** recommendations on objects affecting event kinematics in simulated signal
 1785 events. The E_T^{miss} is reconstructed from fully reconstructed objects so any sys-
 1786 tematic uncertainties affecting jets, muons, electrons, or the E_T^{miss} soft terms are
 1787 included. The only non-negligible contributions found using this method are
 1788 itemized in Table 5 for an example signal sample (1200 GeV, Stable R-Hadron),
 1789 where the systematic is measured as the relative difference in the final signal
 1790 efficiency after apply the associated variation through the CP tools. The only
 1791 variations that are significant are the grouped jet systematic variations, which
 1792 combine recommended jet systematic uncertainties into linearly independent
 1793 variations.

1794 As the peak of the reconstructed E_T^{miss} distribution in the signal is significantly
 1795 above the current threshold for events which pass the trigger requirement, the
 1796 effect of scale variation is expected to be small, which is consistent with the mea-
 1797 sured systematic of approximately 2%. Events which do not pass the trigger re-
 1798 quirement usually fail because there are no ISR jets in the event to balance the
 1799 R -hadrons' transverse momentum, so the reconstructed E_T^{miss} is low and there-
 1800 fore also expected to be not very sensitive to scale changes.

1801 13.1.2.5 MOMENTUM PARAMETRIZATION

1802 The uncertainty on the signal efficiency from track momentum is calculated us-
 1803 ing the **CP** group recommendations for tracks. In particular, only one recom-
 1804 mended systematic variation affects track momentum, the sagitta bias for q/P .
 1805 This uncertainty is propagated to the final selection efficiency by varying the
 1806 track momentum by the recommended one sigma variation, and the associated
 1807 uncertainty is found to be negligible (0.3%).

1808 13.1.2.6 IONIZATION REQUIREMENT

1809 The dE/dx distributions in data and simulated events have different most prob-
 1810 able values, which is due in part to radiation effects in the detector that are not
 1811 fully accounted for in the simulation. The difference does not affect the mass
 1812 measurement used in this analysis, as independent calibrations are done in sim-
 1813 ulation and in data. However, it does affect the efficiency of the high dE/dx
 1814 selection requirement. To calculate the size of the effect on the signal efficiency,

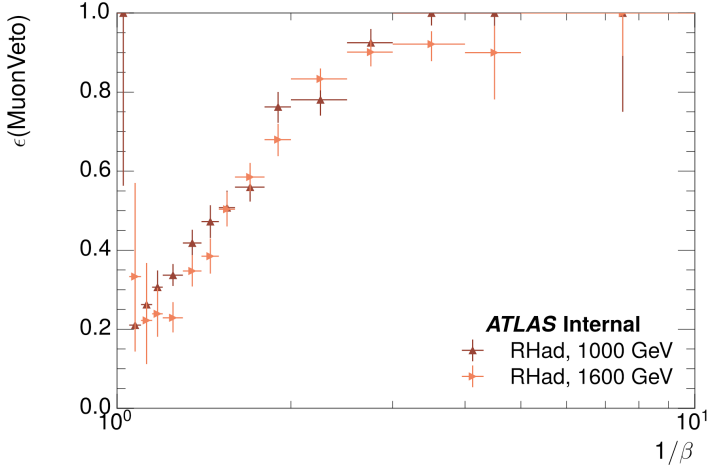


Figure 43: The efficiency of the muon veto for R -hadrons of two different masses, as a function of $\frac{1}{\beta}$ for simulated R-Hadron tracks.

the dE/dx distribution in signal simulation is scaled by a scale factor obtained from comparing the dE/dx distribution of inclusive tracks in data and in simulation. The difference in efficiency for this sample with a scaled dE/dx distribution, relative to the nominal case, is taken as a systematic uncertainty on signal efficiency. The uncertainty is as large as 7% for low masses and falls to a negligible effect for large masses.

13.1.2.7 ELECTRON AND JET REJECTION

The systematic uncertainty on the electron rejection is measured by varying the EM fraction requirement significantly, from 0.95 to 0.9. This is found to have a less than 0.04% effect on signal acceptance, on average, and so is completely negligible. Similarly, the uncertainty on jet rejection is measured by tightening the E/p requirement from 0.5 to 0.4. This is found to have no effect on signal acceptance, so again the systematic is again negligible.

13.1.2.8 MUON VETO

The metastable signal region requires that the candidate tracks are not identified as medium muons because for the majority of R-Hadrons in the lifetime range included in that region do not reach the muon spectrometers before they decay. However, the exponential tail of the R-Hadron lifetime distribution results in some R-Hadrons traversing the muon spectrometer. These can still fail the muon medium identification because they can fail on the requirement on the number of precision hits required to pass the loose selection because they arrive late to the muon spectrometer. This can be seen in Figure 43, which shows the efficiency of the muon veto as a function of $\frac{1}{\beta}$, for two simulated stable R-Hadron samples.

Thus, the efficiency of the muon veto depends on the timing resolution of the spectrometer, so an uncertainty is applied to the signal efficiency to cover

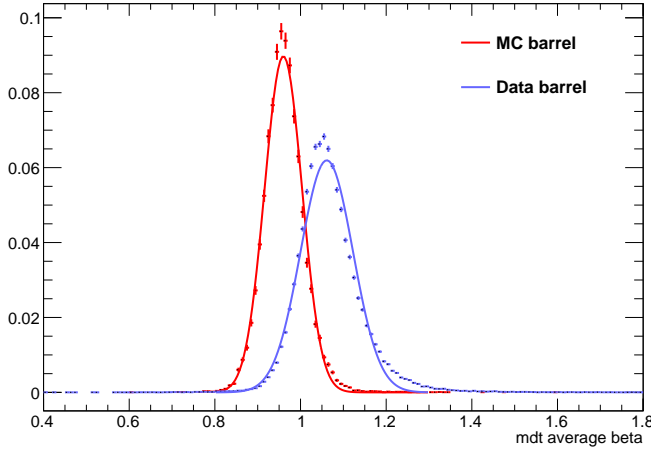


Figure 44: The average reconstructed MDT β distribution for $Z \rightarrow \mu\mu$ events in which one of the muons is reconstructed as a slow muon, for both data and simulation. A gaussian fit is superimposed.

1841 differences in timing resolution between data and simulation. First, a sample
 1842 of $Z \rightarrow \mu\mu$ events is selected in data in which one of the muons has a late ar-
 1843 rived time measured in Monitored Drift Tube ([MDT](#)). Then the reconstructed β
 1844 distribution is compared to the distribution in simulated $Z \rightarrow \mu\mu$ events; the
 1845 difference between these two distributions reflects the difference in timing res-
 1846 olution between data and simulation. To emulate this difference in simulated
 1847 signal events, the magnitude of the difference is used to scale and shift the true
 1848 β distribution of R-Hadrons in simulation. Signal events are then reweighted
 1849 based on this varied β distribution, and the difference in the efficiency of the
 1850 muon veto selection is compared with the nominal and reweighted true β distri-
 1851 butions. The difference in muon veto efficiency is taken as a systematic uncer-
 1852 tainty of the muon veto.

1853 The comparison of reconstructed β between data and simulation is performed
 1854 separately in the barrel, transition, and endcap regions of the spectrometer, and
 1855 the reweighting of the true β distribution in signal is done per region. The com-
 1856 parisons of average reconstructed [MDT](#) β between data and simulation for each
 1857 of the three detector regions in Figure 44 for $Z \rightarrow \mu\mu$ events. As expected, The
 1858 uncertainty is found to be negligible for R -hadrons with short lifetimes, and is
 1859 only significant for lifetimes above 30 ns.

1860 13.1.2.9 LUMINOSITY

1861 The luminosity uncertainty is provided by a luminosity measurement on [ATLAS](#)
 1862 and was measured to be 5% at the time of the publication of this analysis.

1863 13.1.2.10 SIGNAL SIZE

1864 As discussed in Section 10.2, the signal cross sections are calculated at [NLO](#) in the
 1865 strong coupling constant with a resummation of soft-gluon emission at [NLL](#). The

Selection Region	Expected Background	Data
Stable	$17.2 \pm 2.6 \pm 1.2$	16
Metastable	$11.1 \pm 1.7 \pm 0.7$	11

Table 6: The estimated number of background events and the number of observed events in data for the specified selection regions prior to the requirement on mass. The background estimates show statistical and systematic uncertainties.

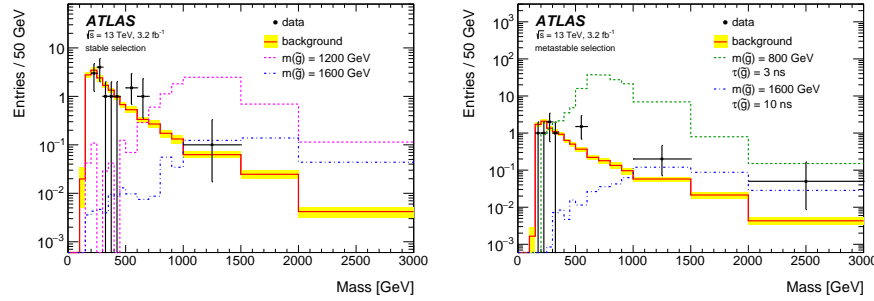


Figure 45: The observed mass distribution of events in data and the generated background distribution in (a) the stable and (b) the metastable signal region. A few example simulated signal distributions are superimposed.

uncertainties on those cross sections are between 14% to 28% for the R-Hadrons in the range of 400 to 1800 GeV [67, 68], where the uncertainty increases with the mass.

13.2 FINAL YIELDS

This full analysis was performed using the 3.2 fb^{-1} from the 2015 data-taking. Using the selections discussed in Chapter 11, sixteen events were observed in the stable signal region and eleven events were observed in the metastable signal region, prior to requirements on the candidate track mass. The background estimate discussed in Chapter 12 predicts $17 \pm 2.6(\text{stat}) \pm 1.2(\text{syst})$ events for the stable region and $11.1 \pm 1.7(\text{stat}) \pm 0.7(\text{syst})$ events for the metastable region. These counts are summarized in Table 6.

The mass estimated using dE/dx (Section 11.4.1) provides the final discriminating variable, where the signal would be expected as an excess in the falling exponential tail of the expected background. The observed distribution of masses is shown in Figure ?? along with the predicted distribution from the background estimate for each signal region. Both include a few example simulated signal distributions, which show the scale of an excess were the R-Hadron signals present. There is no statistically significant evidence of an excess in the data over the background estimation. From this distribution it is clearly possible to rule out signals with lower masses, around 1200 GeV, which have larger cross sections.

1886 13.3 CROSS SECTIONAL LIMITS

1887 Because there is no observed significant excess of events in the signal region, this
 1888 analysis sets upper limits on the allowed cross section for R-Hadron production.
 1889 These limits are set for each mass point by counting the observed events in data,
 1890 along with the expected background and simulated signal events, in windows of
 1891 mass. The mass windows are formed by fitting the distribution of signal events to
 1892 a Gaussian distribution, and the window is then $\pm 1.4\sigma$ around the center of that
 1893 Guassian. Two examples of the windows formed by this procedure are shown in
 1894 Tables 7-8, for the stable and 10 ns working points. The corresponding counts of
 1895 observed data, expected background, and simulated signal for those same work-
 1896 ing points are shown in Tables 9-10. Appendix B includes the mass windows and
 1897 counts for all of the considered signal points.

$m(\tilde{g})$ [GeV]	Left Extremum [GeV]	Right Extremum [GeV]
1000	655	1349
1100	734	1455
1200	712	1631
1300	792	1737
1400	717	1926
1500	815	2117
1600	824	2122
1700	900	2274
1800	919	2344

Table 7: The left and right extremum of the mass window for each generated mass point with a 10 ns lifetime.

$m(\tilde{g})$ [GeV]	Left Extremum [GeV]	Right Extremum [GeV]
800	627	1053
1000	726	1277
1200	857	1584
1400	924	1937
1600	993	2308
1800	1004	2554

Table 8: The left and right extremum of the mass window used for each generated stable mass point.

1898 The 95% confidence level upper limits on the cross sections for a large grid of
 1899 masses (between 800 and 1800 GeV) and lifetimes (between 0.4 and stable) are
 1900 extracted from these counts with the CL_S method using the profile likelihood

$m(\tilde{g})$ [GeV]	Expected Signal	Expected Background	Observed Data
800	462.83 ± 14.86	1.764 ± 0.080	2.0
1000	108.73 ± 3.38	1.458 ± 0.070	1.0
1200	31.74 ± 0.95	1.137 ± 0.060	1.0
1400	10.22 ± 0.29	1.058 ± 0.058	1.0
1600	3.07 ± 0.09	0.947 ± 0.054	1.0
1800	1.08 ± 0.05	0.940 ± 0.054	1.0

Table 9: The expected number of signal events, the expected number of background events, and the observed number of events in data with their respective statistical errors within the respective mass window for each generated stable mass point

$m(\tilde{g})$ [GeV]	Expected Signal	Expected Background	Observed Data
1000	144.48 ± 5.14	1.499 ± 0.069	2.0
1100	73.19 ± 2.61	1.260 ± 0.060	2.0
1200	41.54 ± 1.41	1.456 ± 0.067	2.0
1300	22.58 ± 0.77	1.201 ± 0.058	2.0
1400	12.70 ± 0.42	1.558 ± 0.071	2.0
1500	6.73 ± 0.24	1.237 ± 0.060	2.0
1600	3.90 ± 0.13	1.201 ± 0.058	2.0
1700	2.27 ± 0.07	1.027 ± 0.052	2.0
1800	1.34 ± 0.04	1.019 ± 0.052	2.0

Table 10: The expected number of signal events, the expected number of background events, and the observed number of events in data with their respective statistical errors within the respective mass window for each generated mass point with a lifetime of 10 ns.

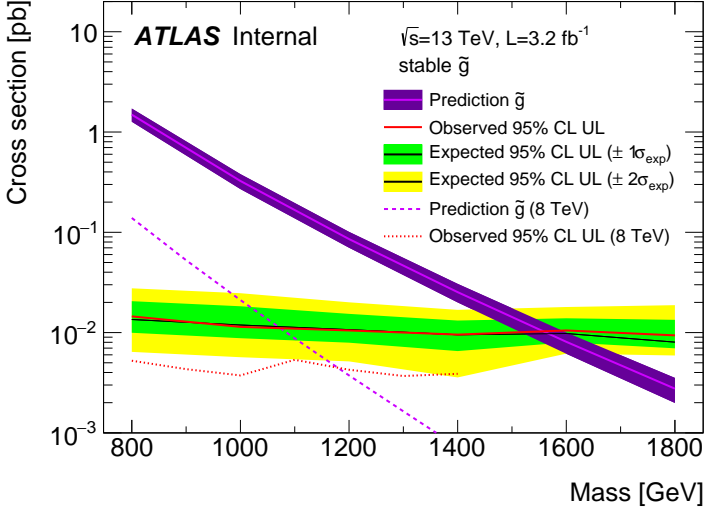


Figure 46: The observed and expected cross section limits as a function of mass for the stable simulated signal. The predicted cross section values for the corresponding signals are included.

ratio as a test statistic [72]. For this procedure, the systematic uncertainties estimated for the signal and background yields are treated as Gaussian-distributed nuisance parameters. The uncertainty on the normalization of the expected background distribution is included in the expected background events. At this point the expected cross section limit is calculated for both the metastable and stable signal region for each lifetime point, and the region with the best expected limit is selected for each lifetime. Using that procedure, the metastable region is used for lifetimes up to and including 30 ns, and the stable region for lifetimes above it.

The resulting cross-sectional upper limits are shown as a function of mass in Figure ?? and Figure ?? for each lifetime considered. The limits are interpolated linearly between each mass point, and the dependence of the limit on the mass is small as the efficiency is relatively constant for large R-Hadron masses. There is however a strong dependence on lifetime, as discussed in Section 11.5, where the probability to form a fully reconstructed track and the kinematic freedom to produce E_T^{miss} result in a local maximum in the limit at 10–30 ns. The figures also include the expected cross section for pair-produced gluino R-Hadrons for reference. For the 10 ns and stable cross section limits, both the observed limit and expected cross section for the Run 1, 8 TeV version of this analysis are included. There the cross sectional limits are lower because of the increased available luminosity, while the signal cross sections were also much lower because of the lower collision energy.

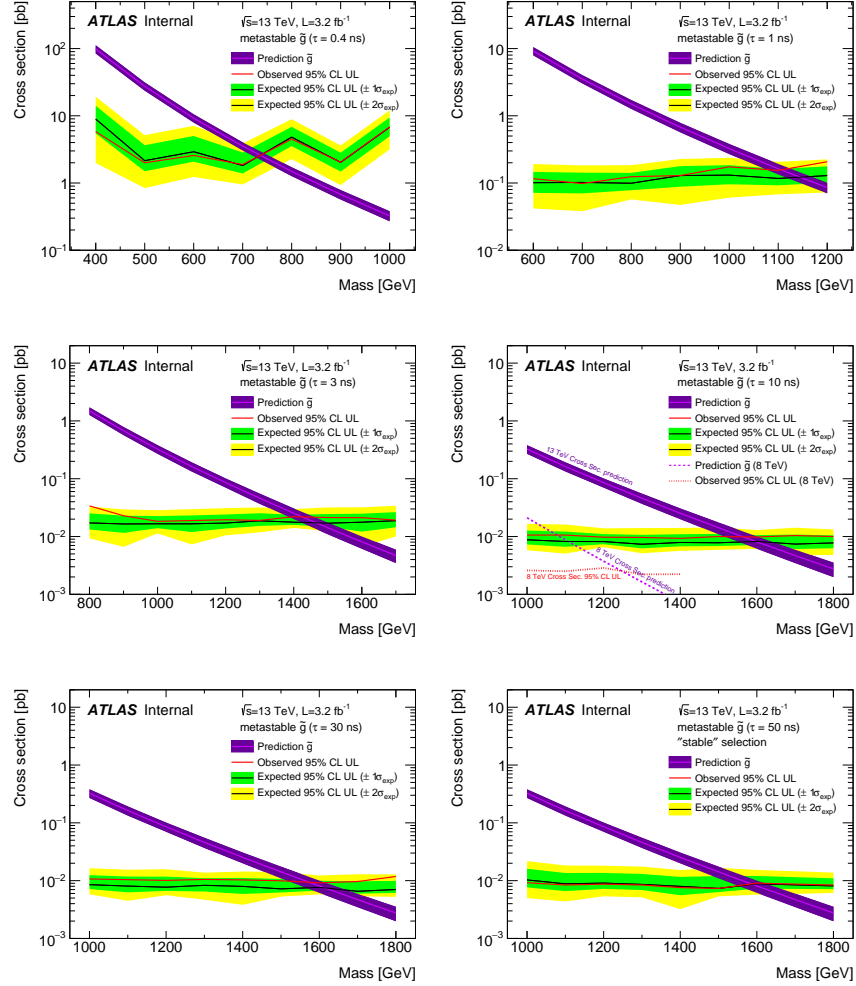


Figure 47: The observed and expected cross section limits as a function of mass for each generated lifetime. The predicted cross section values for the corresponding signals are included.

1923 13.4 MASS LIMITS

1924 The cross-sectional limits can then be used to derive a lower mass limit for gluino
 1925 R-Hadrons by comparing them to the theoretically predicted production cross
 1926 sections. These mass limits range from only 740 GeV at the lowest lifetimes con-
 1927 sidered, where the selection efficiency is very low, to up to 1580 GeV at 30 ns
 1928 where the selection efficiency is maximized. The observed and expected mass
 1929 limits for each lifetime point are detailed in Table 11, which also lists which se-
 1930 lection region was used for each lifetime. These excluded range of masses as a
 1931 function of lifetime is also shown in Figure 48. The Run 1 limits are included for
 1932 comparison; the limits have increased by about 200 GeV on average. The search
 1933 has also improved since the Run 1 version in optimizing the region between 30
 1934 GeV and detector-stable lifetimes by introducing the second signal region. The
 1935 definition of the stable region prevents the significant drop in mass limit that
 1936 occurred above 30 GeV in the Run 1 analysis.

Selection	τ [ns]	$M_{\text{obs}} > [\text{GeV}]$	$M_{\text{exp}} > [\text{GeV}]$
Metastable	0.4	740	730
"	1.0	1110	1150
"	3.0	1430	1470
"	10	1570	1600
"	30	1580	1620
Stable	50	1590	1590
"	stable	1570	1580

Table 11: The observed and expected 95% CL lower limit on mass for gluino R-Hadrons for each considered lifetime.

1937 13.5 CONTEXT FOR LONG-LIVED SEARCHES

1938 This search plays an important role in the current, combined [ATLAS](#) search for
 1939 long lived particles. The mass limits provided by various [ATLAS](#) searches for long-
 1940 lived gluino R-Hadrons can be seen in Figure 49. This search provides the most
 1941 competitive limit for lifetimes between 3 ns and all the way up through very long
 1942 lifetimes, where it is still competitive with dedicated searches for stable particles.
 1943 The limits placed on gluino production are very similar to the limits on promptly
 1944 decaying models.

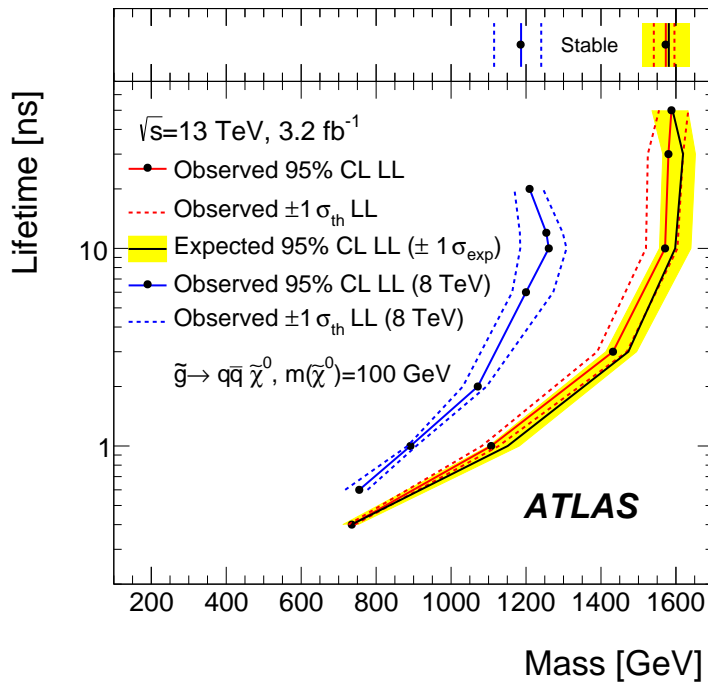


Figure 48: The excluded range of masses as a function of gluino lifetime. The expected lower limit (LL), with its experimental $\pm 1\sigma$ band, is given with respect to the nominal theoretical cross-section. The observed 95% LL obtained at $\sqrt{s} = 8 \text{ TeV}$ [55] is also shown for comparison.

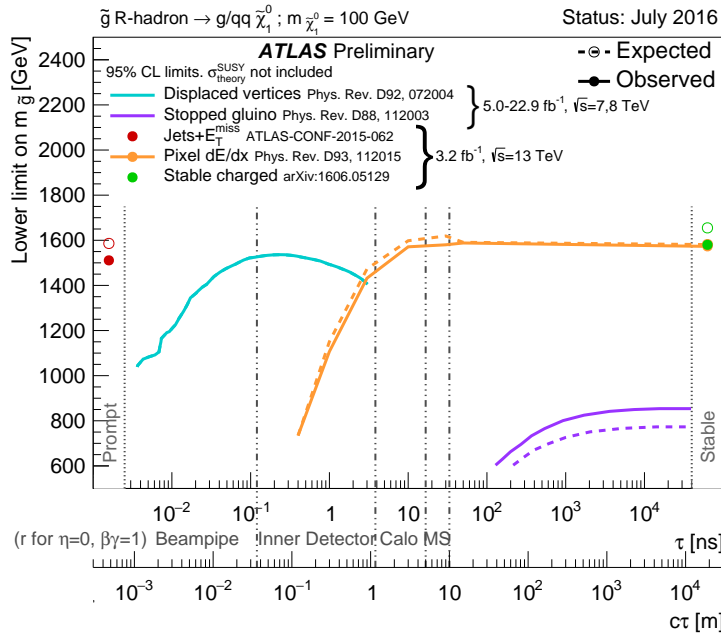


Figure 49: The constraints on the gluino mass as a function of lifetime for a split-supersymmetry model with the gluino R-Hadrons decaying into a gluon or light quarks and a neutralino with mass of 100 GeV. The solid lines indicate the observed limits, while the dashed lines indicate the expected limits. The area below the curves is excluded. The dots represent results for which the particle is assumed to be prompt or stable.

1945

PART VI

1946

CONCLUSIONS

1947

You can put some informational part preamble text here.

14

1948

1949 SUMMARY AND OUTLOOK

1950 14.1 SUMMARY

1951 14.2 OUTLOOK

1952

PART VII

1953

APPENDIX

1954

A

1955

1956 INELASTIC CROSS SECTION

B

$m(\tilde{g})$ [GeV]	Left Extremum [GeV]	Right Extremum [GeV]
1000	682	1387
1100	763	1478
1200	801	1606
1300	809	1841
1400	861	2011
1500	920	2032
1600	952	2173
1800	1017	2422

Table 12: The left and right extremum of the mass window for each generated mass point with a 50 ns lifetime.

$m(\tilde{g})$ [GeV]	Left Extremum [GeV]	Right Extremum [GeV]
1000	689	1321
1100	746	1513
1200	788	1670
1300	860	1734
1400	833	1925
1500	852	2048
1600	833	2283
1700	946	2379
1800	869	2505

Table 13: The left and right extremum of the mass window for each generated mass point with a 30 ns lifetime.

$m(\tilde{g})$ [GeV]	Left Extremum [GeV]	Right Extremum [GeV]
1000	655	1349
1100	734	1455
1200	712	1631
1300	792	1737
1400	717	1926
1500	815	2117
1600	824	2122
1700	900	2274
1800	919	2344

Table 14: The left and right extremum of the mass window for each generated mass point with a 10 ns lifetime.

$m(\tilde{g})$ [GeV]	Left Extremum [GeV]	Right Extremum [GeV]
800	531	1065
900	576	1165
1000	610	1345
1100	635	1432
1200	663	1563
1300	620	1667
1400	742	1727
1500	761	1937
1600	573	2000
1700	621	2182

Table 15: The left and right extremum of the mass window used for each generated mass point with a lifetime of 3 ns.

$m(\tilde{g})$ [GeV]	Left Extremum [GeV]	Right Extremum [GeV]
600	411	758
700	385	876
800	486	970
900	406	987
1000	408	1136
1100	555	1196
1200	516	1378

Table 16: The left and right extremum of the mass window used for each mass point with a lifetime of 1 ns.

$m(\tilde{g})$ [GeV]	Left Extremum [GeV]	Right Extremum [GeV]
400	204	510
500	295	639
600	288	702
700	323	701
800	190	771
900	277	677
1000	249	688

Table 17: The left and right extremum of the mass window for each generated mass point with a lifetime of 0.4 ns.

$m(\tilde{g})$ [GeV]	Left Extremum [GeV]	Right Extremum [GeV]
800	627	1053
1000	726	1277
1200	857	1584
1400	924	1937
1600	993	2308
1800	1004	2554

Table 18: The left and right extremum of the mass window used for each generated stable mass point.

$m(\tilde{g})$ [GeV]	Expected Signal	Expected Background	Observed Data
1000	131.18 ± 6.35	1.803 ± 0.081	1.0 ± 1.0
1100	71.11 ± 3.35	1.409 ± 0.069	1.0 ± 1.0
1200	37.18 ± 1.75	1.310 ± 0.066	1.0 ± 1.0
1300	20.76 ± 0.95	1.431 ± 0.069	1.0 ± 1.0
1400	12.63 ± 0.57	1.273 ± 0.065	1.0 ± 1.0
1500	6.57 ± 0.29	1.115 ± 0.059	1.0 ± 1.0
1600	3.56 ± 0.16	1.041 ± 0.057	1.0 ± 1.0
1800	1.27 ± 0.05	0.918 ± 0.053	1.0 ± 1.0

Table 19: The expected number of signal events, the expected number of background events, and the observed number of events in data with their respective statistical errors within the respective mass window for each generated mass point with a lifetime of 50 ns.

$m(\tilde{g})$ [GeV]	Expected Signal	Expected Background	Observed Data
1000	144.65 ± 6.34	1.328 ± 0.063	2.0 ± 1.4
1100	75.28 ± 3.27	1.255 ± 0.060	2.0 ± 1.4
1200	40.51 ± 1.75	1.193 ± 0.058	2.0 ± 1.4
1300	20.91 ± 0.93	0.997 ± 0.051	2.0 ± 1.4
1400	11.97 ± 0.51	1.131 ± 0.056	2.0 ± 1.4
1500	6.81 ± 0.28	1.111 ± 0.055	2.0 ± 1.4
1600	4.19 ± 0.16	1.193 ± 0.058	2.0 ± 1.4
1700	2.42 ± 0.09	0.963 ± 0.050	2.0 ± 1.4
1800	1.46 ± 0.05	1.138 ± 0.056	3.0 ± 1.7

Table 20: The expected number of signal events, the expected number of background events, and the observed number of events in data with their respective statistical errors within the respective mass window for each generated mass point with a lifetime of 30 ns.

$m(\tilde{g})$ [GeV]	Expected Signal	Expected Background	Observed Data
1000	144.48 ± 5.14	1.499 ± 0.069	2.0 ± 1.4
1100	73.19 ± 2.61	1.260 ± 0.060	2.0 ± 1.4
1200	41.54 ± 1.41	1.456 ± 0.067	2.0 ± 1.4
1300	22.58 ± 0.77	1.201 ± 0.058	2.0 ± 1.4
1400	12.70 ± 0.42	1.558 ± 0.071	2.0 ± 1.4
1500	6.73 ± 0.24	1.237 ± 0.060	2.0 ± 1.4
1600	3.90 ± 0.13	1.201 ± 0.058	2.0 ± 1.4
1700	2.27 ± 0.07	1.027 ± 0.052	2.0 ± 1.4
1800	1.34 ± 0.04	1.019 ± 0.052	2.0 ± 1.4

Table 21: The expected number of signal events, the expected number of background events, and the observed number of events in data with their respective statistical errors within the respective mass window for each generated mass point with a lifetime of 10 ns.

$m(\tilde{g})$ [GeV]	Expected Signal	Expected Background	Observed Data
800	362.97 ± 14.68	1.841 ± 0.080	5.0 ± 2.2
900	169.20 ± 6.69	1.710 ± 0.076	3.0 ± 1.7
1000	84.78 ± 3.23	1.727 ± 0.076	2.0 ± 1.4
1100	40.06 ± 1.60	1.679 ± 0.075	2.0 ± 1.4
1200	20.06 ± 0.81	1.598 ± 0.072	2.0 ± 1.4
1300	10.76 ± 0.43	1.851 ± 0.080	2.0 ± 1.4
1400	5.52 ± 0.22	1.374 ± 0.064	2.0 ± 1.4
1500	3.16 ± 0.13	1.355 ± 0.064	2.0 ± 1.4
1600	2.13 ± 0.11	2.235 ± 0.093	3.0 ± 1.7
1700	1.10 ± 0.06	1.995 ± 0.085	2.0 ± 1.4

Table 22: The expected number of signal events, the expected number of background events, and the observed number of events in data with their respective statistical errors within the respective mass window for each generated mass point with a lifetime of 3 ns.

$m(\tilde{g})$ [GeV]	Expected Signal	Expected Background	Observed Data
600	431.80 ± 36.60	2.418 ± 0.099	3.0 ± 1.7
700	192.77 ± 15.28	3.267 ± 0.126	3.0 ± 1.7
800	69.63 ± 5.90	2.125 ± 0.089	3.0 ± 1.7
900	28.91 ± 2.59	3.114 ± 0.121	3.0 ± 1.7
1000	13.64 ± 1.22	3.359 ± 0.129	5.0 ± 2.2
1100	6.13 ± 0.57	1.879 ± 0.081	3.0 ± 1.7
1200	3.24 ± 0.30	2.387 ± 0.098	5.0 ± 2.2

Table 23: The expected number of signal events, the expected number of background events, and the observed number of events in data with their respective statistical errors within the respective mass window for each generated mass point with a lifetime of 1 ns.

$m(\tilde{g})$ [GeV]	Expected Signal	Expected Background	Observed Data
400	181.71 ± 75.59	6.780 ± 0.238	4.0 ± 2.0
500	103.88 ± 30.05	4.310 ± 0.160	4.0 ± 2.0
600	28.34 ± 9.34	4.868 ± 0.177	4.0 ± 2.0
700	13.62 ± 4.00	3.908 ± 0.147	4.0 ± 2.0
800	2.75 ± 1.15	9.001 ± 0.308	8.0 ± 2.8
900	2.25 ± 0.71	5.045 ± 0.183	5.0 ± 2.2
1000	0.34 ± 0.19	6.026 ± 0.214	6.0 ± 2.4

Table 24: The expected number of signal events, the expected number of background events, and the observed number of events in data with their respective statistical errors within the respective mass window for each generated mass point with a lifetime of p4 ns.

$m(\tilde{g})$ [GeV]	Expected Signal	Expected Background	Observed Data
800	462.83 ± 14.86	1.764 ± 0.080	2.0 ± 1.4
1000	108.73 ± 3.38	1.458 ± 0.070	1.0 ± 1.0
1200	31.74 ± 0.95	1.137 ± 0.060	1.0 ± 1.0
1400	10.22 ± 0.29	1.058 ± 0.058	1.0 ± 1.0
1600	3.07 ± 0.09	0.947 ± 0.054	1.0 ± 1.0
1800	1.08 ± 0.05	0.940 ± 0.054	1.0 ± 1.0

Table 25: The expected number of signal events, the expected number of background events, and the observed number of events in data with their respective statistical errors within the respective mass window for each generated stable mass point

- 1960 [1] S. Agostinelli et al. “GEANT4: A simulation toolkit”. In: *Nucl. Instrum. Meth.*
1961 A 506 (2003), pp. 250–303. doi: [10.1016/S0168-9002\(03\)01368-8](https://doi.org/10.1016/S0168-9002(03)01368-8).
- 1962 [2] ATLAS Collaboration. “A study of the material in the ATLAS inner detector
1963 using secondary hadronic interactions”. In: *JINST* 7 (2012), P01013.
1964 doi: [10.1088/1748-0221/7/01/P01013](https://doi.org/10.1088/1748-0221/7/01/P01013). arXiv: [1110.6191 \[hep-ex\]](https://arxiv.org/abs/1110.6191).
1965 [PERF-2011-08](#).
- 1966 [3] ATLAS Collaboration. “Electron and photon energy calibration with the
1967 ATLAS detector using LHC Run 1 data”. In: *Eur. Phys. J. C* 74 (2014), p. 3071.
1968 doi: [10.1140/epjc/s10052-014-3071-4](https://doi.org/10.1140/epjc/s10052-014-3071-4). arXiv: [1407.5063](https://arxiv.org/abs/1407.5063)
1969 [hep-ex]. [PERF-2013-05](#).
- 1970 [4] ATLAS Collaboration. “A measurement of the calorimeter response to sin-
1971 gle hadrons and determination of the jet energy scale uncertainty using
1972 LHC Run-1 pp -collision data with the ATLAS detector”. In: (2016). arXiv:
1973 [1607.08842 \[hep-ex\]](https://arxiv.org/abs/1607.08842). [PERF-2015-05](#).
- 1974 [5] ATLAS Collaboration. “Single hadron response measurement and calorime-
1975 ter jet energy scale uncertainty with the ATLAS detector at the LHC”. In:
1976 *Eur. Phys. J. C* 73 (2013), p. 2305. doi: [10.1140/epjc/s10052-013-2305-1](https://doi.org/10.1140/epjc/s10052-013-2305-1). arXiv: [1203.1302 \[hep-ex\]](https://arxiv.org/abs/1203.1302). [PERF-2011-05](#).
- 1978 [6] ATLAS Collaboration. “The ATLAS Simulation Infrastructure”. In: *Eur.*
1979 *Phys. J. C* 70 (2010), p. 823. doi: [10.1140/epjc/s10052-010-1429-9](https://doi.org/10.1140/epjc/s10052-010-1429-9).
1980 arXiv: [1005.4568 \[hep-ex\]](https://arxiv.org/abs/1005.4568). [SOFT-2010-01](#).
- 1981 [7] T. Sjöstrand, S. Mrenna, and P. Skands. “A Brief Introduction to PYTHIA
1982 8.1”. In: *Comput. Phys. Commun.* 178 (2008), pp. 852–867. doi: [10.1016/j.cpc.2008.01.036](https://doi.org/10.1016/j.cpc.2008.01.036). arXiv: [0710.3820](https://arxiv.org/abs/0710.3820).
- 1984 [8] ATLAS Collaboration. *Summary of ATLAS Pythia 8 tunes*. ATL-PHYS-PUB-
1985 2012-003. 2012. URL: <http://cds.cern.ch/record/1474107>.
- 1986 [9] A.D. Martin, W.J. Stirling, R.S. Thorne, and G. Watt. “Parton distributions
1987 for the LHC”. In: *Eur. Phys. J. C* 63 (2009). Figures from the [MSTW Website](#),
1988 pp. 189–285. doi: [10.1140/epjc/s10052-009-1072-5](https://doi.org/10.1140/epjc/s10052-009-1072-5). arXiv: [0901.0002](https://arxiv.org/abs/0901.0002).
- 1990 [10] A. Sherstnev and R.S. Thorne. “Parton Distributions for LO Generators”.
1991 In: *Eur. Phys. J. C* 55 (2008), pp. 553–575. doi: [10.1140/epjc/s10052-008-0610-x](https://doi.org/10.1140/epjc/s10052-008-0610-x). arXiv: [0711.2473](https://arxiv.org/abs/0711.2473).
- 1993 [11] A. Ribon et al. *Status of Geant4 hadronic physics for the simulation of LHC*
1994 *experiments at the start of LHC physics program*. CERN-LCGAPP-2010-02.
1995 2010. URL: <http://lcgapp.cern.ch/project/docs/noteStatusHadronic2010.pdf>.

- 1997 [12] M. P. Guthrie, R. G. Alsmiller, and H. W. Bertini. "Calculation of the cap-
1998 ture of negative pions in light elements and comparison with experiments
1999 pertaining to cancer radiotherapy". In: *Nucl. Instrum. Meth.* 66 (1968), pp. 29–
2000 36. doi: [10.1016/0029-554X\(68\)90054-2](https://doi.org/10.1016/0029-554X(68)90054-2).
- 2001 [13] H. W. Bertini and P. Guthrie. "News item results from medium-energy
2002 intranuclear-cascade calculation". In: *Nucl. Instr. and Meth. A* 169 (1971),
2003 p. 670. doi: [10.1016/0375-9474\(71\)90710-X](https://doi.org/10.1016/0375-9474(71)90710-X).
- 2004 [14] V.A. Karmanov. "Light Front Wave Function of Relativistic Composite
2005 System in Explicitly Solvable Model". In: *Nucl. Phys. B* 166 (1980), p. 378.
2006 doi: [10.1016/0550-3213\(80\)90204-7](https://doi.org/10.1016/0550-3213(80)90204-7).
- 2007 [15] H. S. Fesefeldt. *GHEISHA program*. Pitha-85-02, Aachen. 1985.
- 2008 [16] G. Folger and J.P. Wellisch. "String parton models in Geant4". In: (2003).
2009 arXiv: [nucl-th/0306007](https://arxiv.org/abs/nucl-th/0306007).
- 2010 [17] N. S. Amelin et al. "Transverse flow and collectivity in ultrarelativistic
2011 heavy-ion collisions". In: *Phys. Rev. Lett.* 67 (1991), p. 1523. doi: [10.1103/PhysRevLett.67.1523](https://doi.org/10.1103/PhysRevLett.67.1523).
- 2013 [18] N. S. Amelin et al. "Collectivity in ultrarelativistic heavy ion collisions". In:
2014 *Nucl. Phys. A* 544 (1992), p. 463. doi: [10.1016/0375-9474\(92\)90598-E](https://doi.org/10.1016/0375-9474(92)90598-E).
- 2016 [19] L. V. Bravina et al. "Fluid dynamics and Quark Gluon string model - What
2017 we can expect for Au+Au collisions at 11.6 AGeV/c". In: *Nucl. Phys. A* 566
2018 (1994), p. 461. doi: [10.1016/0375-9474\(94\)90669-6](https://doi.org/10.1016/0375-9474(94)90669-6).
- 2019 [20] L. V. Bravin et al. "Scaling violation of transverse flow in heavy ion colli-
2020 sions at AGS energies". In: *Phys. Lett. B* 344 (1995), p. 49. doi: [10.1016/0370-2693\(94\)01560-Y](https://doi.org/10.1016/0370-2693(94)01560-Y).
- 2022 [21] B. Andersson et al. "A model for low-pT hadronic reactions with general-
2023 izations to hadron-nucleus and nucleus-nucleus collisions". In: *Nucl. Phys.*
2024 *B* 281 (1987), p. 289. doi: [10.1016/0550-3213\(87\)90257-4](https://doi.org/10.1016/0550-3213(87)90257-4).
- 2025 [22] B. Andersson, A. Tai, and B.-H. Sa. "Final state interactions in the (nuclear)
2026 FRITIOF string interaction scenario". In: *Z. Phys. C* 70 (1996), pp. 499–
2027 506. doi: [10.1007/s002880050127](https://doi.org/10.1007/s002880050127).
- 2028 [23] B. Nilsson-Almqvist and E. Stenlund. "Interactions Between Hadrons and
2029 Nuclei: The Lund Monte Carlo, Fritiof Version 1.6". In: *Comput. Phys. Com-*
2030 *mun.* 43 (1987), p. 387. doi: [10.1016/0010-4655\(87\)90056-7](https://doi.org/10.1016/0010-4655(87)90056-7).
- 2031 [24] B. Ganhuyag and V. Uzhinsky. "Modified FRITIOF code: Negative charged
2032 particle production in high energy nucleus nucleus interactions". In: *Czech.*
2033 *J. Phys.* 47 (1997), pp. 913–918. doi: [10.1023/A:1021296114786](https://doi.org/10.1023/A:1021296114786).
- 2034 [25] ATLAS Collaboration. "Topological cell clustering in the ATLAS calorime-
2035 ters and its performance in LHC Run 1". In: (2016). arXiv: [1603.02934](https://arxiv.org/abs/1603.02934)
2036 [[hep-ex](#)].
- 2037 [26] Peter Speckmayer. "Energy Measurement of Hadrons with the CERN AT-
2038 LAS Calorimeter". Presented on 18 Jun 2008. PhD thesis. Vienna: Vienna,
2039 Tech. U., 2008. URL: <http://cds.cern.ch/record/1112036>.

- 2040 [27] CMS Collaboration. “The CMS barrel calorimeter response to particle
2041 beams from 2 to 350 GeV/c”. In: *Eur. Phys. J. C* 60.3 (2009). doi: [10.1140/epjc/s10052-009-0959-5](https://doi.org/10.1140/epjc/s10052-009-0959-5).
- 2043 [28] J. Beringer et al. (Particle Data Group). “Review of Particle Physics”. In:
2044 *Chin. Phys. C* 38 (2014), p. 090001. URL: <http://pdg.lbl.gov>.
- 2045 [29] P. Adragna et al. “Measurement of Pion and Proton Response and Lon-
2046 gitudinal Shower Profiles up to 20 Nuclear Interaction Lengths with the
2047 ATLAS Tile Calorimeter”. In: *Nucl. Instrum. Meth. A* 615 (2010), pp. 158–
2048 181. doi: [10.1016/j.nima.2010.01.037](https://doi.org/10.1016/j.nima.2010.01.037).
- 2049 [30] ATLAS Collaboration. “Jet energy measurement and its systematic uncer-
2050 tainty in proton–proton collisions at $\sqrt{s} = 7$ TeV with the ATLAS detec-
2051 tor”. In: *Eur. Phys. J. C* 75 (2015), p. 17. doi: [10.1140/epjc/s10052-014-3190-y](https://doi.org/10.1140/epjc/s10052-014-3190-y). arXiv: [1406.0076 \[hep-ex\]](https://arxiv.org/abs/1406.0076). PERF-2012-01.
- 2053 [31] Hung-Liang Lai, Marco Guzzi, Joey Huston, Zhao Li, Pavel M. Nadolsky,
2054 et al. “New parton distributions for collider physics”. In: *Phys. Rev. D* 82
2055 (2010), p. 074024. doi: [10.1103/PhysRevD.82.074024](https://doi.org/10.1103/PhysRevD.82.074024). arXiv: [1007.2241 \[hep-ph\]](https://arxiv.org/abs/1007.2241).
- 2057 [32] E. Abat et al. “Study of energy response and resolution of the ATLAS barrel
2058 calorimeter to hadrons of energies from 20 to 350 GeV”. In: *Nucl. Instrum.*
2059 *Meth. A* 621.1-3 (2010), pp. 134 – 150. doi: <http://dx.doi.org/10.1016/j.nima.2010.04.054>.
- 2061 [33] ATLAS Collaboration. “Jet energy measurement with the ATLAS detector
2062 in proton–proton collisions at $\sqrt{s} = 7$ TeV”. In: *Eur. Phys. J. C* 73 (2013),
2063 p. 2304. doi: [10.1140/epjc/s10052-013-2304-2](https://doi.org/10.1140/epjc/s10052-013-2304-2). arXiv: [1112.6426 \[hep-ex\]](https://arxiv.org/abs/1112.6426). PERF-2011-03.
- 2065 [34] Nausheen R. Shah and Carlos E. M. Wagner. “Gravitons and dark matter in
2066 universal extra dimensions”. In: *Phys. Rev. D* 74 (2006), p. 104008. doi: [10.1103/PhysRevD.74.104008](https://doi.org/10.1103/PhysRevD.74.104008). arXiv: [hep-ph/0608140 \[hep-ph\]](https://arxiv.org/abs/hep-ph/0608140).
- 2068 [35] Jonathan L. Feng, Arvind Rajaraman, and Fumihiro Takayama. “Graviton
2069 cosmology in universal extra dimensions”. In: *Phys. Rev. D* 68 (2003), p. 085018.
2070 doi: [10.1103/PhysRevD.68.085018](https://doi.org/10.1103/PhysRevD.68.085018). arXiv: [hep-ph/0307375 \[hep-ph\]](https://arxiv.org/abs/hep-ph/0307375).
- 2072 [36] Paul H. Frampton and Pham Quang Hung. “Long-lived quarks?” In: *Phys.*
2073 *Rev. D* 58 (5 1998), p. 057704. doi: [10.1103/PhysRevD.58.057704](https://doi.org/10.1103/PhysRevD.58.057704).
2074 URL: <http://link.aps.org/doi/10.1103/PhysRevD.58.057704>.
- 2076 [37] C. Friberg, E. Norrbin, and T. Sjostrand. “QCD aspects of leptoquark pro-
2077 duction at HERA”. In: *Phys. Lett. B* 403 (1997), pp. 329–334. doi: [10.1016/S0370-2693\(97\)00543-1](https://doi.org/10.1016/S0370-2693(97)00543-1). arXiv: [hep-ph/9704214 \[hep-ph\]](https://arxiv.org/abs/hep-ph/9704214).
- 2079 [38] Herbert K. Dreiner. “An introduction to explicit R-parity violation”. In:
2080 (1997). arXiv: [hep-ph/9707435](https://arxiv.org/abs/hep-ph/9707435).

- 2081 [39] Edmond L. Berger and Zack Sullivan. “Lower limits on R-parity-violating
 2082 couplings in supersymmetry”. In: *Phys. Rev. Lett.* 92 (2004), p. 201801. doi:
 2083 [10.1103/PhysRevLett.92.201801](https://doi.org/10.1103/PhysRevLett.92.201801). arXiv: [hep-ph/0310001](https://arxiv.org/abs/hep-ph/0310001).
- 2084 [40] R. Barbieri, C. Berat, M. Besancon, M. Chemtob, A. Deandrea, et al. “R-
 2085 parity violating supersymmetry”. In: *Phys. Rept.* 420 (2005), p. 1. doi: [10.1016/j.physrep.2005.08.006](https://doi.org/10.1016/j.physrep.2005.08.006). arXiv: [hep-ph/0406039](https://arxiv.org/abs/hep-ph/0406039).
- 2087 [41] M. Fairbairn et al. “Stable massive particles at colliders”. In: *Phys. Rept.* 438
 2088 (2007), p. 1. doi: [10.1016/j.physrep.2006.10.002](https://doi.org/10.1016/j.physrep.2006.10.002). arXiv: [hep-ph/0611040](https://arxiv.org/abs/hep-ph/0611040).
- 2090 [42] Christopher F. Kolda. “Gauge-mediated supersymmetry breaking: Intro-
 2091 duction, review and update”. In: *Nucl. Phys. Proc. Suppl.* 62 (1998), p. 266.
 2092 doi: [10.1016/S0920-5632\(97\)00667-1](https://doi.org/10.1016/S0920-5632(97)00667-1). arXiv: [hep-ph/9707450](https://arxiv.org/abs/hep-ph/9707450).
- 2093 [43] Howard Baer, Kingman Cheung, and John F. Gunion. “A Heavy gluino as
 2094 the lightest supersymmetric particle”. In: *Phys. Rev. D* 59 (1999), p. 075002.
 2095 doi: [10.1103/PhysRevD.59.075002](https://doi.org/10.1103/PhysRevD.59.075002). arXiv: [hep-ph/9806361](https://arxiv.org/abs/hep-ph/9806361).
- 2096 [44] S. James Gates Jr. and Oleg Lebedev. “Searching for supersymmetry in
 2097 hadrons”. In: *Phys. Lett. B* 477 (2000), p. 216. doi: [10.1016/S0370-2693\(00\)00172-6](https://doi.org/10.1016/S0370-2693(00)00172-6). arXiv: [hep-ph/9912362](https://arxiv.org/abs/hep-ph/9912362).
- 2099 [45] G. F. Giudice and A. Romanino. “Split supersymmetry”. In: *Nucl. Phys. B*
 2100 699 (2004), p. 65. doi: [10.1016/j.nuclphysb.2004.11.048](https://doi.org/10.1016/j.nuclphysb.2004.11.048). arXiv:
 2101 [hep-ph/0406088](https://arxiv.org/abs/hep-ph/0406088).
- 2102 [46] N. Arkani-Hamed, S. Dimopoulos, G. F. Giudice, and A. Romanino. “As-
 2103 pects of split supersymmetry”. In: *Nucl. Phys. B* 709 (2005), p. 3. doi: [10.1016/j.nuclphysb.2004.12.026](https://doi.org/10.1016/j.nuclphysb.2004.12.026). arXiv: [hep-ph/0409232](https://arxiv.org/abs/hep-ph/0409232).
- 2105 [47] Glennys R. Farrar and Pierre Fayet. “Phenomenology of the Production,
 2106 Decay, and Detection of New Hadronic States Associated with Supersym-
 2107 metry”. In: *Phys. Lett. B* 76 (1978), pp. 575–579. doi: [10.1016/0370-2693\(78\)90858-4](https://doi.org/10.1016/0370-2693(78)90858-4).
- 2109 [48] A. C. Kraan, J. B. Hansen, and P. Nevski. “Discovery potential of R-hadrons
 2110 with the ATLAS detector”. In: *Eur. Phys. J. C* 49 (2007), pp. 623–640. doi:
 2111 [10.1140/epjc/s10052-006-0162-x](https://doi.org/10.1140/epjc/s10052-006-0162-x). arXiv: [hep-ex/0511014](https://arxiv.org/abs/hep-ex/0511014)
 2112 [[hep-ex](https://arxiv.org/abs/hep-ex)].
- 2113 [49] K. A. Olive et al. “Review of Particle Physics”. In: *Chin. Phys. C* 38 (2014),
 2114 p. 090001. doi: [10.1088/1674-1137/38/9/090001](https://doi.org/10.1088/1674-1137/38/9/090001).
- 2115 [50] Rasmus Mackeprang and David Milstead. “An Updated Description of
 2116 Heavy-Hadron Interactions in GEANT-4”. In: *Eur. Phys. J. C* 66 (2010), pp. 493–
 2117 501. doi: [10.1140/epjc/s10052-010-1262-1](https://doi.org/10.1140/epjc/s10052-010-1262-1). arXiv: [0908.1868](https://arxiv.org/abs/0908.1868)
 2118 [[hep-ph](https://arxiv.org/abs/hep-ph)].
- 2119 [51] ATLAS Collaboration. “Search for massive, long-lived particles using mul-
 2120 titrack displaced vertices or displaced lepton pairs in pp collisions at $\sqrt{s} =$
 2121 8 TeV with the ATLAS detector”. In: *Phys. Rev. D* 92 (2015), p. 072004.
 2122 doi: [10.1103/PhysRevD.92.072004](https://doi.org/10.1103/PhysRevD.92.072004). arXiv: [1504.05162](https://arxiv.org/abs/1504.05162) [[hep-ex](https://arxiv.org/abs/hep-ex)].
 2123 SUSY-2014-02.

- 2124 [52] ATLAS Collaboration. “Search for charginos nearly mass degenerate with
 2125 the lightest neutralino based on a disappearing-track signature in pp col-
 2126 lisions at $\sqrt{s} = 8$ TeV with the ATLAS detector”. In: *Phys. Rev. D* 88 (2013),
 2127 p. 112006. doi: [10.1103/PhysRevD.88.112006](https://doi.org/10.1103/PhysRevD.88.112006). arXiv: [1310.3675](https://arxiv.org/abs/1310.3675)
 2128 [[hep-ex](#)]. SUSY-2013-01.
- 2129 [53] ATLAS Collaboration. “Searches for heavy long-lived sleptons and R-Hadrons
 2130 with the ATLAS detector in pp collisions at $\sqrt{s} = 7$ TeV”. In: *Phys. Lett. B*
 2131 720 (2013), p. 277. doi: [10.1016/j.physletb.2013.02.015](https://doi.org/10.1016/j.physletb.2013.02.015). arXiv:
 2132 [1211.1597](https://arxiv.org/abs/1211.1597) [[hep-ex](#)]. SUSY-2012-01.
- 2133 [54] ATLAS Collaboration. “Searches for heavy long-lived charged particles
 2134 with the ATLAS detector in proton–proton collisions at $\sqrt{s} = 8$ TeV”. In: *JHEP* 01 (2015), p. 068. doi: [10.1007/JHEP01\(2015\)068](https://doi.org/10.1007/JHEP01(2015)068). arXiv:
 2135 [1411.6795](https://arxiv.org/abs/1411.6795) [[hep-ex](#)]. SUSY-2013-22.
- 2136 [55] ATLAS Collaboration. “Search for metastable heavy charged particles with
 2137 large ionisation energy loss in pp collisions at $\sqrt{s} = 8$ TeV using the AT-
 2138 LAS experiment”. In: *Eur. Phys. J. C* 75 (2015), p. 407. doi: [10.1140/epjc/s10052-015-3609-0](https://doi.org/10.1140/epjc/s10052-015-3609-0). arXiv: [1506.05332](https://arxiv.org/abs/1506.05332) [[hep-ex](#)]. SUSY-
 2139 2014-09.
- 2140 [56] ATLAS Collaboration. “Search for heavy long-lived charged R -hadrons
 2141 with the ATLAS detector in 3.2 fb^{-1} of proton–proton collision data at
 2142 $\sqrt{s} = 13$ TeV”. In: *Phys. Lett. B* 760 (2016), pp. 647–665. doi: [10.1016/j.physletb.2016.07.042](https://doi.org/10.1016/j.physletb.2016.07.042). arXiv: [1606.05129](https://arxiv.org/abs/1606.05129) [[hep-ex](#)].
- 2143 [57] Torbjorn Sjöstrand, Stephen Mrenna, and Peter Skands. “PYTHIA 6.4 Physics
 2144 and Manual”. In: *JHEP* 0605 (2006), p. 026. doi: [10.1088/1126-6708/2006/05/026](https://doi.org/10.1088/1126-6708/2006/05/026). arXiv: [hep-ph/0603175](https://arxiv.org/abs/hep-ph/0603175).
- 2145 [58] *Further ATLAS tunes of PYTHIA6 and Pythia 8*. Tech. rep. ATL-PHYS-PUB-
 2146 2011-014. Geneva: CERN, 2011. URL: <https://cds.cern.ch/record/1400677>.
- 2147 [59] Aafke Christine Kraan. “Interactions of heavy stable hadronizing parti-
 2148 cles”. In: *Eur. Phys. J. C* 37 (2004), pp. 91–104. doi: [10.1140/epjc/s2004-01946-6](https://doi.org/10.1140/epjc/s2004-01946-6). arXiv: [hep-ex/0404001](https://arxiv.org/abs/hep-ex/0404001) [[hep-ex](#)].
- 2149 [60] M. Fairbairn et al. “Stable massive particles at colliders”. In: *Phys. Rept.* 438
 2150 (2007), p. 1. doi: [10.1016/j.physrep.2006.10.002](https://doi.org/10.1016/j.physrep.2006.10.002). arXiv: [hep-ph/0611040](https://arxiv.org/abs/hep-ph/0611040).
- 2151 [61] W. Beenakker, R. Hopker, M. Spira, and P. M. Zerwas. “Squark and gluino
 2152 production at hadron colliders”. In: *Nucl. Phys. B* 492 (1997), p. 51. doi:
 2153 [10.1016/S0550-3213\(97\)00084-9](https://doi.org/10.1016/S0550-3213(97)00084-9). arXiv: [hep-ph/9610490](https://arxiv.org/abs/hep-ph/9610490).
- 2154 [62] A. Kulesza and L. Motyka. “Threshold resummation for squark-antisquark
 2155 and gluino-pair production at the LHC”. In: *Phys. Rev. Lett.* 102 (2009),
 2156 p. 111802. doi: [10.1103/PhysRevLett.102.111802](https://doi.org/10.1103/PhysRevLett.102.111802). arXiv: [0807.2405](https://arxiv.org/abs/0807.2405) [[hep-ph](#)].

- 2165 [63] A. Kulesza and L. Motyka. “Soft gluon resummation for the production
 2166 of gluino-gluino and squark-antisquark pairs at the LHC”. In: *Phys. Rev.*
 2167 *D* 80 (2009), p. 095004. doi: [10.1103/PhysRevD.80.095004](https://doi.org/10.1103/PhysRevD.80.095004). arXiv:
 2168 [0905.4749 \[hep-ph\]](https://arxiv.org/abs/0905.4749).
- 2169 [64] Wim Beenakker, Silja Brensing, Michael Kramer, Anna Kulesza, Eric Lae-
 2170 nen, et al. “Soft-gluon resummation for squark and gluino hadroproduc-
 2171 tion”. In: *JHEP* 0912 (2009), p. 041. doi: [10.1088/1126-6708/2009/12/041](https://doi.org/10.1088/1126-6708/2009/12/041). arXiv: [0909.4418 \[hep-ph\]](https://arxiv.org/abs/0909.4418).
- 2173 [65] W. Beenakker, S. Brensing, M.n Kramer, A. Kulesza, E. Laenen, et al. “Squark
 2174 and Gluino Hadroproduction”. In: *Int. J. Mod. Phys. A* 26 (2011), p. 2637.
 2175 doi: [10.1142/S0217751X11053560](https://doi.org/10.1142/S0217751X11053560). arXiv: [1105.1110 \[hep-ph\]](https://arxiv.org/abs/1105.1110).
- 2176 [66] Michael Krämer et al. *Supersymmetry production cross sections in pp collisions*
 2177 at $\sqrt{s} = 7 \text{ TeV}$. 2012. arXiv: [1206.2892 \[hep-ph\]](https://arxiv.org/abs/1206.2892).
- 2178 [67] Rasmus Mackeprang and Andrea Rizzi. “Interactions of Coloured Heavy
 2179 Stable Particles in Matter”. In: *Eur. Phys. J. C*50 (2007), pp. 353–362. doi:
 2180 [10.1140/epjc/s10052-007-0252-4](https://doi.org/10.1140/epjc/s10052-007-0252-4). arXiv: [hep-ph/0612161](https://arxiv.org/abs/hep-ph/0612161)
 2181 [hep-ph].
- 2182 [68] Rasmus Mackeprang and David Milstead. “An Updated Description of
 2183 Heavy-Hadron Interactions in GEANT-4”. In: *Eur. Phys. J. C*66 (2010), pp. 493–
 2184 501. doi: [10.1140/epjc/s10052-010-1262-1](https://doi.org/10.1140/epjc/s10052-010-1262-1). arXiv: [0908.1868](https://arxiv.org/abs/0908.1868)
 2185 [hep-ph].
- 2186 [69] J. Alwall, R. Frederix, S. Frixione, V. Hirschi, F. Maltoni, O. Mattelaer, H. S.
 2187 Shao, T. Stelzer, P. Torrielli, and M. Zaro. “The automated computation of
 2188 tree-level and next-to-leading order differential cross sections, and their
 2189 matching to parton shower simulations”. In: *JHEP* 07 (2014), p. 079. doi:
 2190 [10.1007/JHEP07\(2014\)079](https://doi.org/10.1007/JHEP07(2014)079). arXiv: [1405.0301 \[hep-ph\]](https://arxiv.org/abs/1405.0301).
- 2191 [70] “dE/dx measurement in the ATLAS Pixel Detector and its use for particle
 2192 identification”. In: (2011).
- 2193 [71] ATLAS Collaboration. “The ATLAS Simulation Infrastructure”. In: *Eur.*
 2194 *Phys. J. C*70 (2010), pp. 823–874. doi: [10.1140/epjc/s10052-010-1429-9](https://doi.org/10.1140/epjc/s10052-010-1429-9). arXiv: [1005.4568 \[physics.ins-det\]](https://arxiv.org/abs/1005.4568).
- 2196 [72] Alexander L. Read. “Presentation of search results: The CL(s) technique”.
 2197 In: *J. Phys. G*28 (2002). [,11(2002)], pp. 2693–2704. doi: [10.1088/0954-3899/28/10/313](https://doi.org/10.1088/0954-3899/28/10/313).

2199 DECLARATION

2200 Put your declaration here.

2201 *Berkeley, CA, September 2016*

2202

Bradley Axen

2203

2204 COLOPHON

2205

Not sure that this is necessary.